Metasurface Enhanced Ultra-wideband Multifunctional Antenna Arrays and Fabry-Perot Antennas

Alpha Osman Bah

Thesis submitted to the School of Electrical and Data Engineering
Faculty of Engineering and Information Technology
University of Technology Sydney

In fulfilment of the requirements for the degree of

Doctor of Philosophy

October 2019

Certificate of Original Authorship

I, Alpha Osman Bah declare that this thesis, is submitted in fulfilment of the requirements for the award of Doctor of Philosophy, in the Faculty of Engineering and Information Technology at the University of Technology Sydney. This thesis is wholly my own work unless otherwise referenced or acknowledged. In addition, I certify that all information sources and literature used are indicated in the thesis. This document has not been submitted for qualifications at any other academic institution. This research is supported by the Australian Government Research Training Program, the Commonwealth Scientific and Industrial Research Organization (CSIRO), and the Cooperative Research Centre for Space Environment Management (SERC Limited) through the Australian Government's Cooperative Research Centre Programme.

Signature: Production Note: Signature removed prior to publication.

Date: 4/10/2019

Acknowledgements

First and foremost, I would like to give thanks and praise to Almighty Allah for giving me the courage and perseverance to undertake this research study at this time of my life.

I am indebted to my advisors Prof. Jay Guo and Dr. Peiyuan Qin for their continued support and guidance along this journey. Our very fruitful fortnightly group meetings were a valuable opportunity to learn from other Distinguished Professors at the Global Big Data Technologies Centre (GBDTC) and from fellow colleagues. Special thanks go to Prof. Trevor Bird, Prof. Richard Ziolkowski and Prof. Bevan Jones for their support and useful advice during my candidature.

I would like to acknowledge the help and support of the management and staff at the GBDTC for their professionalism and friendship, and for organizing meetings, scholarships, conference travels, and the list goes on. I would also like to thank my colleagues for some fruitful discussions, especially Shulin Chen for having such a kind heart.

I would like to express my sincere appreciation to the Commonwealth Scientific and Industrial Research Organisation (CSIRO), the Space Environment Research Centre (SERC), and Jenkins Engineering Defense Systems (JEDS) for their timely financial and technical support. I would also like to thank the staff at the Faculty of Engineering and Information Technology (FEIT) workshop of the University of Technology Sydney, for their help with the fabrication of the antenna prototypes.

This work is dedicated to my wife, Maimouna Bah, and our three beautiful children, Hassanatu Bah, Isatu Bah, and Mohamed Gandor Bah. I would like to thank them for their love, patience, and support during this challenging period, without which this work would not have been possible.

Thesis Format

The format of this Thesis is by compilation. The major contents of Chapter 2 are derived from a paper we published in *Scientific Reports* entitled, "Realization of an Ultra-thin Metasurface to Facilitate Wide Bandwidth, Wide Angle Beam Scanning." The major contents in Chapter 3 are derived from a paper we published in the *IEEE Transactions on Antennas and Propagation*, entitled "A Wideband Low-Profile Tightly Coupled Antenna Array with a Very High Figure of Merit." Chapter 3 is based on a paper we submitted to the *IEEE Transactions on Antennas and Propagation*, entitled “A Wideband Low-Profile Fabry-Perot Antenna Employing a Multi-Resonant Metasurface Based Superstrate.” The publication details of these Journal papers, and other Conference Proceeding Papers, Presentations, Posters, and Book Chapter that I have contributed towards are given in the next section.

Publications

Refereed Journal Articles

[1] A. O. Bah, P. Y. Qin, R. W. Ziolkowski, Y. J. Guo and T. S. Bird, "A Wideband Low-Profile Tightly Coupled Antenna Array with a Very High Figure of Merit," *IEEE Trans. Antennas Propag.,* vol. 67, no. 4, pp. 2332-2343, Apr. 2019. doi: 10.1109/TAP.2019.2891460

[2] A. O. Bah, P. Y. Qin, R. W. Ziolkowski, Q. Cheng and Y. J. Guo, "Realization of an Ultra-thin Metasurface to Facilitate Wide Bandwidth, Wide Angle Beam Scanning," *Scientific reports*, vol. 8, no. 1, 2018, pp. 4761. doi:10.1038/s41598-018-23288-4

[3] A. O. Bah, Y. J. Guo, P. Y. Qin and T. S. Bird, "A Wideband Low-Profile Fabry-Perot Antenna Employing a Multi-Resonant Metasurface Based Superstrate," *IEEE Trans. Antennas Propag*, Feb. 2019. (Submitted).

Book Chapters

[1] T. S. Bird, A. O. Bah, and K. Smart, "Measurement of Mutual Coupling Effects," in *Mutual Coupling Between Antennas*, John Wiley & Sons, West Sussex, UK. (In preparation).

Presentations, Posters, and Conference Proceeding Papers

[2] A. O. Bah, P. Y. Qin, and T. S. Bird, "A Low Profile Antenna Array with a 5.6:1 Bandwidth for Multifunctional Applications," *16th Australian Symposium on Antennas (ASA2019),* Sydney, Australia, 2019. (Poster presentation)

[3] A. O. Bah, R. W. Ziolkowski, P. Qin, and Y. J. Guo, "Design and analysis of a wide angle impedance matching metasurface for wideband antenna arrays," *12th European Conference on Antennas and Propagation (EuCAP 2018)*, London, pp. 1-4, 2018.

[4] A. O. Bah, P. Y. Qin and Y. J. Guo, "A Wideband (5.6:1) Antenna Array with a Simple Low Profile Feed Structure," *International Symposium on Antennas and Propagation (ISAP 2018)*, Busan, South Korea, 2018. http://isap2018.org/download/program/ThB1.PDF

[5] A. O. Bah, Pei-Yuan Qin and Y. J. Guo, "An extremely wideband tapered balun for application in tightly coupled arrays," *2016 IEEE-APS Topical Conference on Antennas and Propagation in Wireless Communications (APWC)*, Cairns, QLD, pp. 162-165, 2016.

[6] X. Yang, G. Zhao, W. Hu, Y. J. Guo, Y. Z. Yin and A. O. Bah, "Characteristics of wideband phased array with two-layer metasurface," *2016 International Conference on Electromagnetics in Advanced Applications (ICEAA)*, Cairns, QLD, pp. 852-855, 2016.

[7] A. O. Bah, "Reconfigurable ultrawideband tightly coupled antenna arrays," *2016 Space Environment Research Centre (SERC) Colloquium*, Mount Stromlo, Canberra, 2016.

Abbreviations

AA	Aperture Arrays
A_{eff}	Effective Area
AMC	Artificial Magnetic Conductor
AMS	Aperture Type Metasurface
Apertif	Aperture Tile in Focus
ASKAP	Australian Square Kilometre Array Pathfinder
B	Balun
CA	Connected Array
CM	Common Mode
COTS	Commercial Off The Shelf
CPS	Coplanar Strip
CPW	Coplanar Waveguide
CSIRO	Commonwealth Scientific Industrial and Research Organisation
DBW	Directivity Bandwidth
DBWP	Directivity Bandwidth Product
DS	Double Sided
EBG	Electromagnetic Bandgap
EM	Electromagnetic
EMBRACE	Electronic Multibeam Radio Astronomy Concept
EW	Electronic Warfare
FOV	Field of View
FPA	Fabry-Perot Antenna
FSS	Frequency Selective Surface
GBW	Gain Bandwidth
GBWP	Gain Bandwidth Product
HFSS	High Frequency Structure Simulator
LFAA	Low Frequency Aperture Array
LOFAR	Low Frequency Array

MFAA	Mid Frequency Aperture Array
MS	Metasurface
MT	Meandered Transformer
MTM	Metamaterial
MVG	Microwave Vision Group
MWA	Murchison Widefield Array
NZI	Near Zero Index
P_A	Array Figure of Merit
PAF	Phased Array Feed
PCB	Printed Circuit Board
PCS	Phase Correcting Structure
PEC	Perfect Electric Conductor
PMC	Perfect Magnetic Conductor
PMS	Patch Type Metasurface
PRS	Partially Reflective Surface
PUMA	Planar Ultrawideband Modular Array
SB	Shorter Balun
SIW	Substrate Integrated Waveguide
SKA	Square Kilometre Array
SKA1-Low	Square Kilometre Array Phase-1 Low Frequency
SKA1-Mid	Square Kilometre Array Phase-1 Mid Frequency
SRR	Split Ring Resonator
SS	Single Sided
ST	Straight Transformer
TCAA	Tightly Coupled Antenna Array
TCDA-IB	Tightly Coupled Dipole Array with an Integrated Balun
TC-UAJC	Tightly Coupled Unequal Arm Jerusalem Cross
TE	Transverse Electric
TM	Transverse Magnetic
UCS	Uniform Current Sheet

UWB	Ultrawideband
VSWR	Voltage Standing Wave Ratio
WAIM	Wide Angle Impedance Matching

Table of Contents

List of Tables

List of Figures

Abstract

In recent years, the demand for ultra-wideband (UWB) antennas and arrays has escalated due to their flexibility and high data rate capabilities. This demand is driven by bandwidth intensive applications such as radio telescopes, satellite communications, and advanced radar systems. Wideband antennas enable the incorporation of multiple steerable beams, polarizations, and frequency bands onto a single multifunctional aperture.

Two of the main obstacles to truly multifunctional tightly coupled antenna arrays (TCAAs) is the problem of impedance mismatch at the aperture–air boundary and the need for a wideband and fully integrated feed network. The high cost and losses in the feed networks of TCAAs renders them impractical for some applications. In these cases, the low-cost and highly efficient Fabry-Perot antenna (FPA) provides a possible solution.

In the first part of this thesis, we present the design, analysis, and practical implementation of a 10x10 wideband TCAA with a very high figure of merit. The array figure of merit is a single number which takes into account the bandwidth, profile, polarization, scan range, and overall complexity of the array. An improved design of the fabricated array has a performance that approaches the fundamental limits of low profile arrays with a bandwidth of 5.5:1, a maximum scan range of 80° along the E-plane, and a profile of $\sim\lambda_L/12$. This excellent performance is enabled by a newly introduced feed network that is simple, inexpensive, and extremely wideband; in conjunction with a novel ultra-thin metasurface superstrate for wideband wide angle impedance matching.

The usual method of enhancing the gain bandwidth of FPAs involve the use of multi-layered superstrate structures which increase their profile and complexity. In the second part of this thesis, we develop a new approach to FPA gain bandwidth enhancement. Using this new approach, a small foot print, wideband, and low-profile FPA empowered by a single multi-resonant metasurface superstrate is designed, fabricated and tested. Due to the small foot print of this FPA, it can be easily employed as an element in an active array setting without the introduction of grating lobes. At the same time, the number

of active elements will be significantly reduced compared to the dense TCAAs leading to substantial cost reductions.

Chapter 1 - Introduction

1.1 Problem Statement

The demand for ultra-wideband (UWB) antennas and arrays has escalated exponentially due in part to the increasing number of bandwidth intensive applications, the shrinking size of antenna platforms and the need for multifunctional antenna systems. This work introduces a new class of low-profile, UWB antennas, as critical components in future multifunctional systems [1], radio telescopes [2], advanced radar systems [3], and software defined radios [4].

The traditional methods of UWB array design substantially limits the achievable bandwidth as the isolated behavior of the antenna elements differ significantly from those in the array setting [5]. In addition, traditional phased arrays are usually narrowband, bulky, non-conformal, difficult to scale to higher frequencies, and too expensive for commercial applications, which makes them impractical for many applications [6]. More recently, new approaches to UWB array designs have been developed commonly referred to as "tightly coupled antenna arrays" (TCAA) [7-10]. These arrays are compact, conformal and grating lobes free. A TCAA may refer to directly connected elements (connected array) [7, 8] or capacitively coupled elements [9, 10]. TCAAs have many desirable characteristics, however, several key challenges have not been fully addressed. For instance, to overcome the impedance mismatch at the aperture–air boundary when scanning, bulky and heavy dielectric superstrates have been used as wide angle impedance matching (WAIM) layers [11, 12]. Various attempts have been made to replace this dielectric layer with a more light-weight, thin, and low cost metasurface. However, the WAIM functionality achieved so far using metasurfaces has been restricted to a limited range of frequencies. In addition, to practically realize very large bandwidth in low profile implementations, a simple, compact, equally wideband, and fully integrated feed network is required, that can perform unbalanced-to-balanced as well as impedance transformations.

The high cost and losses in the feed networks of TCAAs renders them impractical for some applications. In these cases, the highly directive Fabry-Perot antenna (FPA) [13] with a simpler structure, less lossy feed network, and of cheaper cost compared to antenna arrays provides a possible

solution. Due to their numerous advantages, FPAs find many applications in areas such as satellite communications, electronic warfare, sensor networks, and point-point links. One major disadvantage of FPAs lies in their inherently narrow gain bandwidth, which poses a major challenge. Existing gain bandwidth improvement attempts, including the use of metasurface superstrates, has shown marginal success. The low profile TCAA and FPA antennas introduced in this work fully address the above mentioned challenges.

1.2 Research Significance and Objectives

As the platforms on which antennas operate continue to shrink, wideband multifunctional apertures employing multiple beams, polarizations, and frequency bands are needed. These apertures can consolidate various communication and sensing systems onto a single wideband device ensuring substantial reduction in size, weight, cost and power consumption [14]. A typical multifunctional antenna installed on a navy ship for example, can simultaneously receive GPS signals, electronic warfare (EW) signals, Radar signals, and land communications as shown in the generic multifunctional aperture in Fig. 1.1 Without multifunctional antennas, each application would require a separate antenna with substantial increases in cost and complexity.

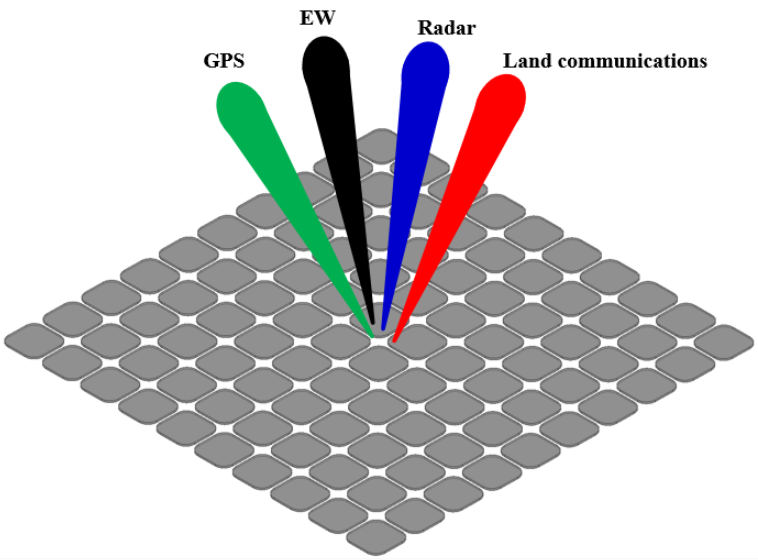

Fig. 1. 1. A generic multifunctional aperture showing simultaneous individual beams for GPS, EW, Radar, and Land communications.

Another emerging area of UWB array application is in the next generation of radio telescopes such as the square kilometre array (SKA) [2]. The SKA has two types of arrays that can be arranged either densely or sparsely into phased array fed (PAF) dish arrays or aperture arrays (AA). PAFs are created by placing a receiver array at the focal plane of a parabolic dish whereas AAs are standalone, electrically dense arrays of low-gain elements, with a direct view to the sky [15]. The Commonwealth Scientific and Industrial Organisation (CSIRO) designed chequerboard PAF receiver [16, 17] is shown in Fig. 1.2 (a). PAFs generate multiple beams with a wide scan range to achieve a wide field-of-view (FoV) for the rapid detection of faint radio waves from space and the imaging of different areas of the sky simultaneously. The Australian SKA Pathfinder's (ASKAP) FoV [18] is depicted in Fig. 1.2 (b) with 36 beams. Traditional Telescopes with single pixel feeds have only one beam. ASKAP and the Aperture tile in focus (Apertif) [19], are two of the leading PAF precursors and technology demonstrators of the SKA. Their operating frequencies are (0.7 – 1.8) GHz and (1 – 1.7) GHz respectively.

The SKA is to be constructed in two phases. During phase-1, a sparse irregular low frequency AA (LFAA) [20] covering 50 MHz – 350 MHz will be built at the Murchison Radio Astronomy

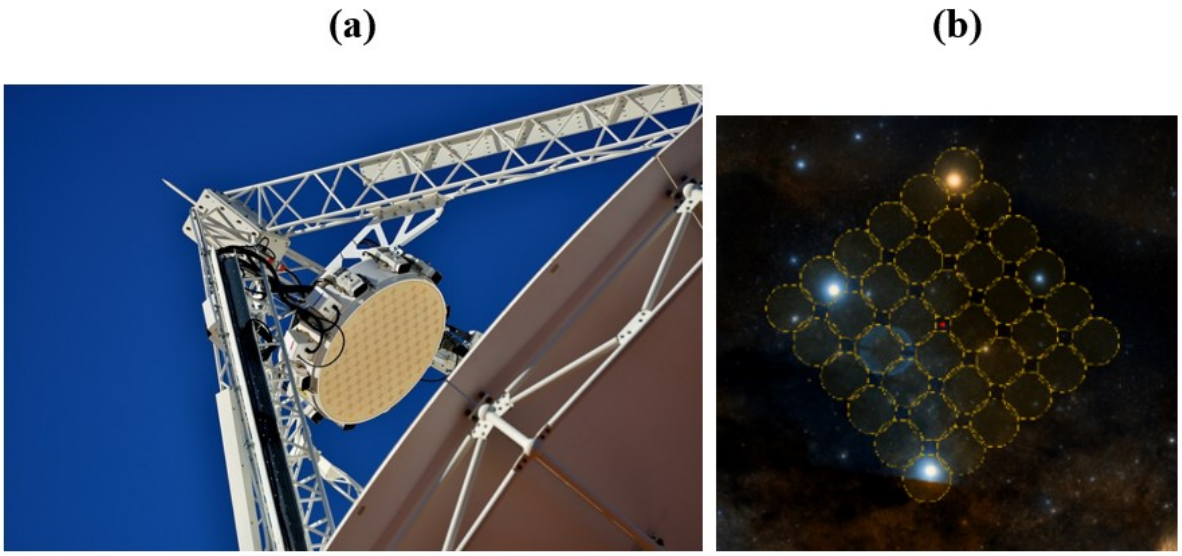

Fig. 1. 2. The Australian SKA Pathfinder Radio Telescope. (a) The CSIRO designed PAF receiver placed at the focal plane of a parabolic dish [16]. (b) The 'fields of view' seen with the PAF receiver showing 36 individual beams [18]. Images courtesy of CSIRO.

Observatory site in Western Australia (SKA1-low) using 2^{17} log-periodic antenna elements in 512 stations. Also during phase-1, the mid to high frequency (0.35 GHz – 15.3 GHz) component of the SKA (SKA1-mid) [21] will be built in South Africa and Australia using dense AAs, dense PAF focal plane arrays, and horn cluster fed focal plane arrays. During phase-2, the more technically challenging mid frequency aperture array (MFAA) [22], will be built in South Africa and the SKA capabilities expanded further into other African countries and within Australia. An artist's impression of the MFAA telescope on the African site is shown in Fig. 1.3. It is composed of planar arrays and dish arrays. The LOw Frequency Array (LOFAR) [23], the Murchison Widefield Array (MWA) [24], and the Electronic Multibeam Radio Astronomy ConcEpt (EMBRACE) [25] are currently being trialed as effective pathfinders for the SKA1-low and SKA1-mid aperture arrays.

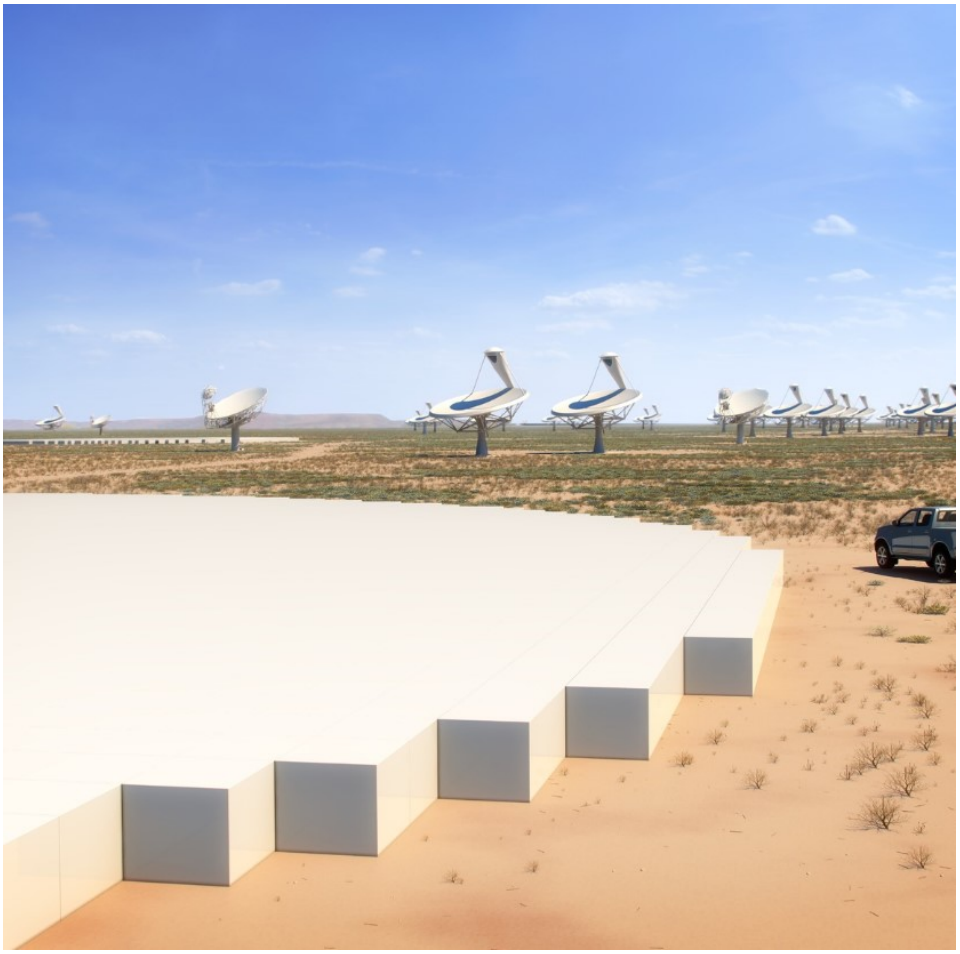

Fig. 1. 3. An Artist's impression of the Mid Frequency Aperture Array (MFAA) telescope. Foreground: Planar arrays (0.4 GHz -1.450 GHz). Background: Dish arrays with cluster feeds or PAFs (0.35 GHz – 15.3 GHz). Image courtesy of the SKA organisation.

To be able to cover the SKA1-mid frequency band from 0.35 GHz to 15.3 GHz, the operation range of current arrays needs to be expanded quite significantly using fewer antennas.

The objectives of this thesis are to fully address the three challenges listed previously inorder to facilitate multifunctional operation. The first objective is to enhance the performance of current TCAAs by reducing the complexity and profile of their feed networks. The second objective is to improve their wide angle impedance matching characteristics with the aid of a novel wideband ultra-thin metasurface superstrate. The third objective is to utilize our understanding of the wideband metasurface to design a multi-resonant metasurface superstrate with significant improvements to the gain bandwidth and profile of the traditionally narrowband Fabry-Perot antenna. The low-profile tightly coupled antenna array and the wideband Faby-Perot antenna introduced in this work provides tangible solutions to the three identified research objectives.

1.3 Literature Review

Some of the most critical issues for practical realization of wideband, low profile arrays, with good scan performance and low cross polarization are outlined below. We start by giving an overview of four types of arrays with a variety of operational principles. The first part describes the ubiquitous Vivaldi antenna array and its variants. The second part deals with another class of periodically fed wideband arrays using either capacitively or directly connected elements. The third part details the low profile planar ultra-wideband modular array (PUMA). Finally, the fourth part introduces the Fabry-Perot antenna as a possible alternative to the other three due to its simplicity, high efficiency, and lower cost.

1.3.1 Flared Notch (Vivaldi) Antenna

There have been numerous investigations into increasing antenna array bandwidth using a wide variety of techniques. One such technique uses the flared notch (Vivaldi) antenna [26] to achieve over a 10:1 impedance bandwidth [27]. However, this wide bandwidth is achieved at the expense of an increased array profile. The bandwidth of a Vivaldi antenna is given by the relationship, B = 2*H/W [28], where W is the width of the antenna and H is its height. As an example, the profile of the array shown in Fig. 1.4 is 3.9 wavelengths long at the highest frequency of operation. Furthermore, these antennas are

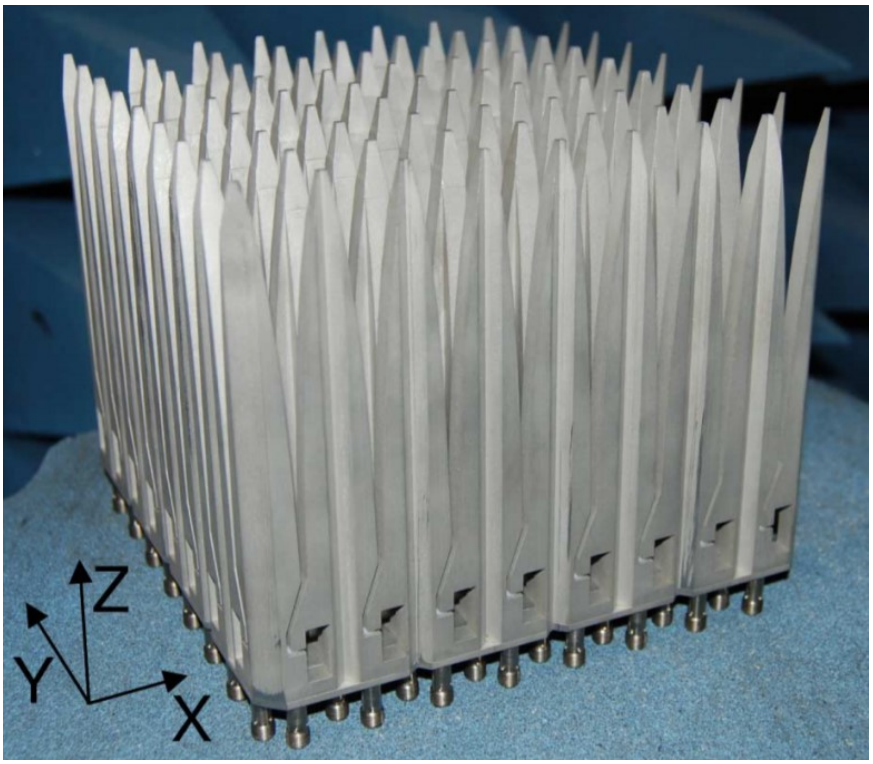

Fig. 1. 4. An 8x8 dual-polarized Vivaldi array of flared-notches [27]. The array profile is $3.9\lambda_H$ at 9 GHz.

Fig. 1. 5. An 8x9 dual-polarized prototype of the BAVA array [30]. Operating frequency: 1.8 GHz - 18 GHz.

usually heavy, are wide spread in the E-plane, and have high cross-polarization levels in the diagonal planes [29].

The modified Vivaldi (i.e. balanced antipodal Vivaldi antenna, BAVA) [30] can achieve a 10:1 bandwidth with a $\lambda_H/2$ thick profile and has a better than -17 dB cross-polarization level across all planes where λ_H is the wavelength at the highest frequency of operation. Nonetheless, the BAVA shows high scanning voltage standing wave ratios (VSWR) across the H-plane. An 8x9 dual-polarized prototype of the BAVA array is shown in Fig 1.5. The above-mentioned designs are usually quite costly and difficult to fabricate.

1.3.2 Tightly Coupled Antenna Arrays

Tightly coupled antenna arrays (TCAAs) are another class of periodically fed wideband arrays with either directly connected [7, 8] or capacitively coupled elements [9, 10]. Their operation is based on Wheeler's infinite uniform current sheet (UCS) concept [31, 32], which is an ideal case of a phased array with no reflecting boundary, radiating equally at all frequencies. This concept is equivalent to an infinite number of very small, tightly packed electric or magnetic dipoles, carrying continuous current over an open circuit or short circuit boundary. In this model, the current is roughly constant over the entire array for very short dipoles but the performance decreases sharply as the dipole length approach half a wavelength at the highest frequency. Figure 1.6 shows the evolution of the UCS concept for both electric and magnetic dipoles. The work presented in this Thesis is focused on capacitively-coupled arrays.

TCAAs have been implemented in various forms using dipoles [33 – 36, 10], patches [37, 38], spirals [39, 40], fractal geometries [41], bowties [42 - 44], long slots [45, 46], and optical techniques [47, 48] to achieve wideband arrays. One major challenge in TCAAs is the design of an equally wideband feed network. The earlier prototypes [9] made use of bulky feed organizers and commercially available external 180° hybrids for cable routing, common mode (CM) suppression, and balanced

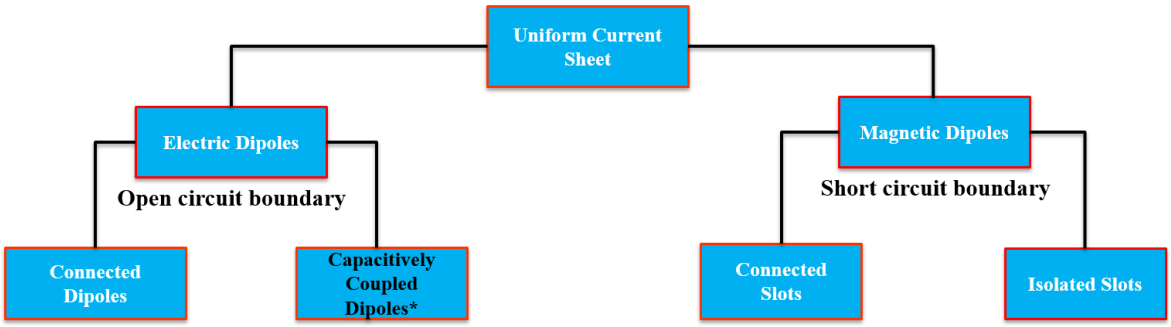

Fig. 1. 6. Evolution of the uniform current sheet concept

feeding. Subsequent TCAA designs have attempted to incorporate the feed network into the array design in order to remove the feed organiser.The feeding mechanism of TCAAs can be broadly into two categories, namely, the balun based feeds, and the planar ultra-wideband modular array (PUMA) [50 - 53] feeds. The PUMA array uses shorting posts instead of baluns to mitigate CM resonances.

1.3.2.1 Balun based feeds

TCAAs utilise variations of dipoles as array elements. These dipoles are balanced antennas and require a balanced feed structure to ensure that the current flowing on both arms of the dipoles are equal and opposite. A transformer called a balun is required to connect the balanced dipole terminals to the unbalanced coaxial feed. Various feeding arrangements have been proposed in the literature for TCAAs including differential feeds [42], printed baluns [6, 28, 30, 39], and tightly coupled dipole arrays with integrated baluns (TCDA-IB) [10]. The desired balun should also be at least as wideband as the array itself and able to provide a balanced feed together with impedance transformation.

a) Differential feed

To prevent the occurrence of common modes due to vertically polarized currents on the dipole feed lines, their currents should be equal in magnitude but opposite in phase over the whole frequency band of interest. In addition, the feed lines must also be shielded to prevent unbalanced currents when scanning along the E-plane due to mutual coupling. This can be accomplished by employing twin coaxial lines (with their jackets soldered together) between the array and an external wideband balun to force a 180° phase difference between the feed lines [42]. This relatively straightforward feeding arrangement

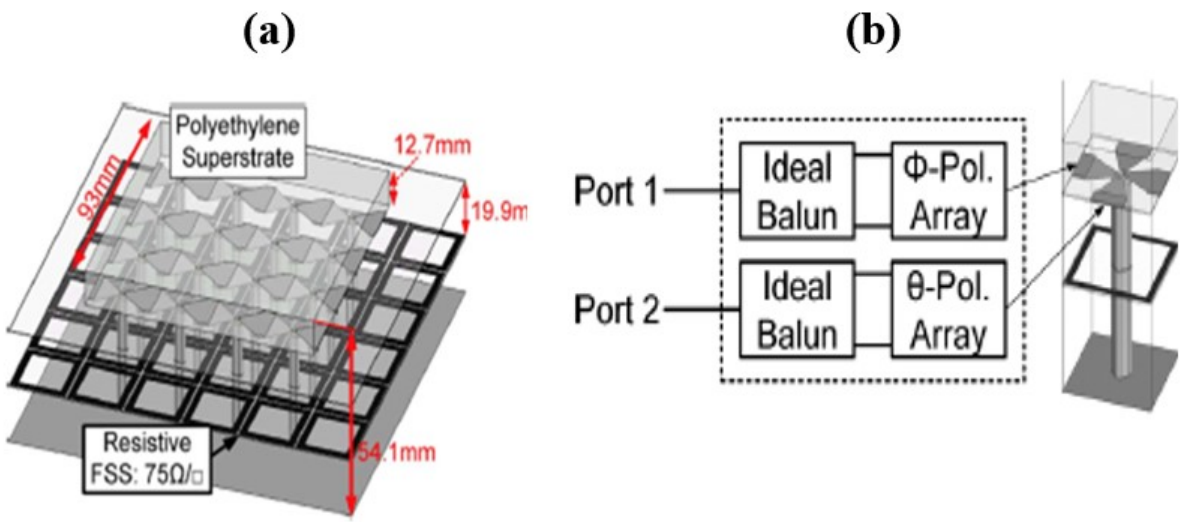

Fig. 1. 7. TCAA with a differential feed [42]. (a) A 4x4 prototype of the twin coaxially fed TCAA with a resistive frequency selective surface (FSS) for further bandwidth increase. (b) External wideband baluns connected to the θ-polarized and ϕ-polarized sections of the array.

is shown in Fig. 1.7. However, the use of bulky external 180° hybrid baluns in conjunction with power dividers, leads to significant increase in the total size, weight, and cost of the array as well as fabrication complexities when scaling to higher frequencies. This feeding technique together with a resistive frequency selective surface (FSS) realized a bandwidth of 21:1 albeit at a loss of between 2-7 dB. Alternative feeding methods that are more conformal and integrated with the array are needed to overcome these drawbacks.

Printed planar balun feeds are compact and low profile but despite this, they yield reduced bandwidth compared to other feeding methods. They include co-planar waveguides in conjunction with lumped baluns [34], ring hybrids in tandem with twin coaxial lines [6, 35], and planar microstrip baluns combined with ferrite beads [43]. The feed in [43] is compact but display a reduced bandwidth (2:1) and lower efficiency (~40%). The feeds in [6, 35] use non-symmetric dipoles (ball-and-cup) with integrated printed baluns and matching networks as shown in Fig. 1.8. The dipoles are modified to provide additional degrees of freedom to control their self-inductance, mutual capacitance with neighboring elements, and to cancel the ground plane inductance. These additional degrees of freedom in turn enable independent control of the input impedance and wave velocity. These feeds are compact, enable high efficiency (>93%) and wide scanning angles (>75° in E plane) but have lower bandwidth (1.6:1).

b) Printed planar baluns

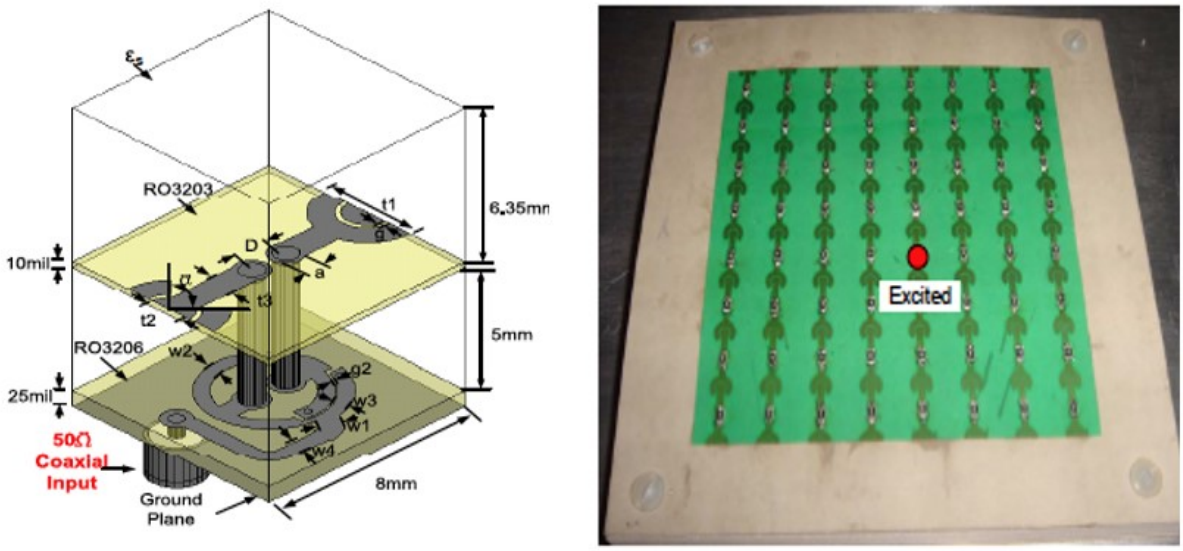

Fig. 1. 8. The unit cell of the printed ring hybrid fed TCAA (left) and the resulting 8x8 finite array (right) [6, 35].

In [34], a wideband commercial off the shelf (COTS) balun and printed transformer (4:1) was employed between the coplanar waveguide (CPW) feed and the coplanar strip (CPS) sections. However, this comes at a higher balun/transformer cost, limited scanning range (30° in the H-plane) and difficulty in integration.

c) TCDA with integrated balun

A new type of feed was introduced in [10] known as a Tightly Coupled Dipole Array with an Integrated Balun (TCDA-IB) as shown in Fig. 1.9. The TCDA-IB feed is based on the Marchand balun [49]. It consist of an open circuited microstrip line at right angles to a short circuited slotline. This arrangement forces a differential signal along the slot. The short circuit at the end of the slotline ensures that energy flows only in one direction. In the TCDA-IB feed arrangement, the reactance of the balun is tuned to cancel that of the array, thereby acting as part of the impedance matching network. This ensures that the balun and TCDA achieves wider bandwidth compared to a differentially fed array.

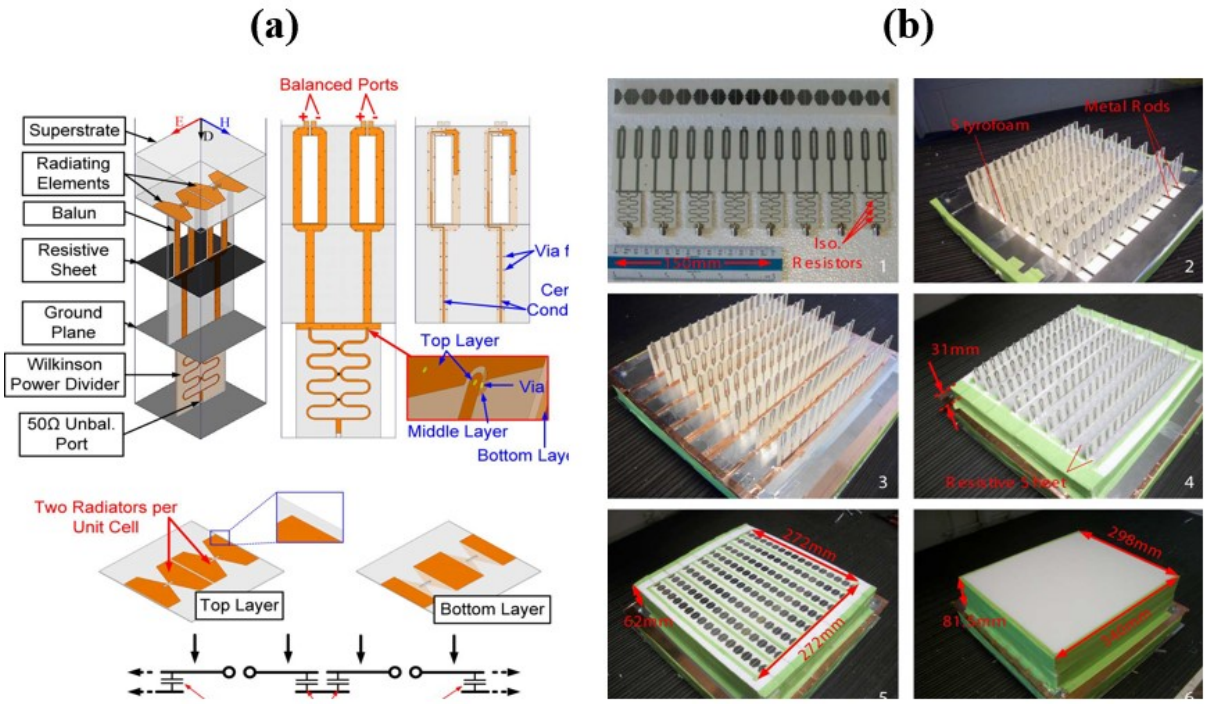

Fig. 1. 9. The TCDA-IB [10]. (a) Component parts of the TCDA-IB unit cell. (b) Component parts of the TCDA-IB prototype.

The TCDA-IB uses a dual-balun split unit cell with a dual-offset feed to enable dual polarization, reduce dipole input impedance, increase compactness, minimize inter feed coupling, and reduce cross-polarization by eliminating common mode resonance. The feed is comprised of a three stage Wilkinson power divider and an integrated folded Marchand balun to provide a balanced feed together with impedance transformation. This feeding arrangement does not require external balancing circuitry; however, it requires extremely compact baluns since two baluns are required for each radiating element. Additionally, the integrated feed is multilayered and quite complicated. The TCDA-IB feed helped overcome the size, weight, and bandwidth limitation of previous feeds. They facilitated bandwidths up to 7.35:1.

1.3.2.2 PUMA feeds

Other feeding techniques have been developed that avoids baluns altogether and uses unbalanced feed lines and shorting posts to mitigate common mode resonances. The arrangement of the shorting posts in a PUMA [50] fed array together with the fabricated prototype is shown in Fig. 1.10. Bandwidths up to

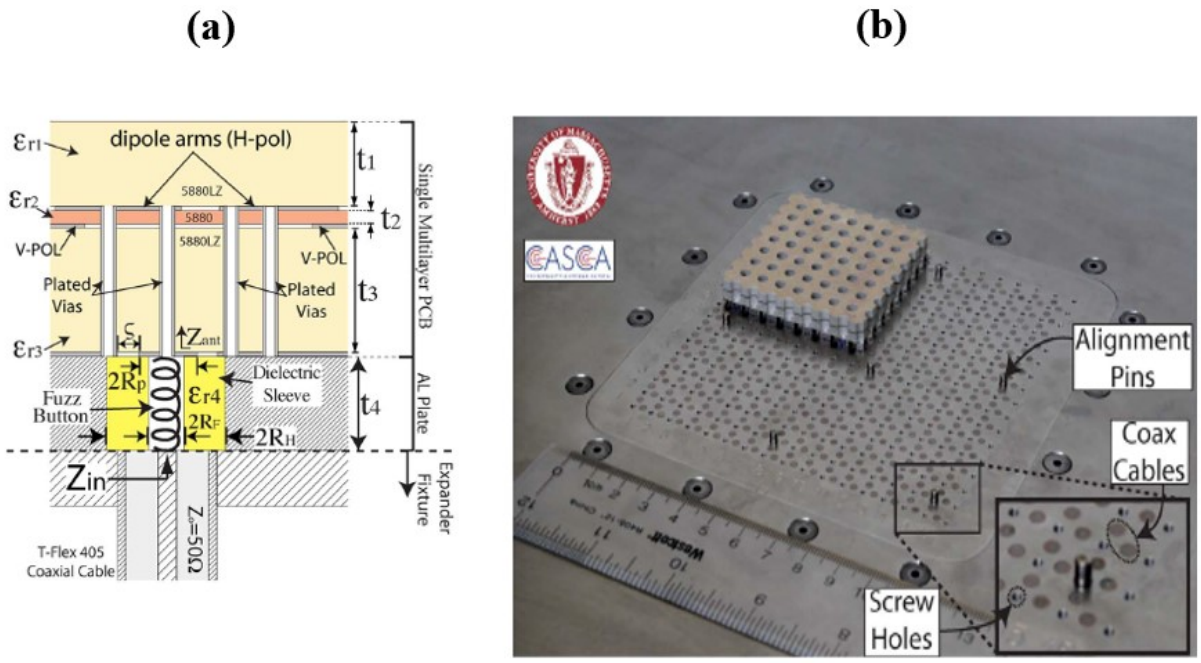

Fig. 1. 10. PUMA array [50]. (a) Detailed view of the unbalanced fed PUMA array unit cell showing H-polarized and V-polarized dipole arms embedded in a dielectric medium with two plated vias (shorting posts) per arm. (b) The fabricated PUMA tiles sitting on an Aluminium expander fixture.

6:1 have been obtained using this technique [51] while scanning to 45°. This feeding technique has been used to produce low-cost, wide scanning, and dual-offset dual polarized PUMA arrays [50 - 53]. The PUMA array was designed to overcome some of the limitations of the balun-based feeding methods while also retaining a simple, modular, tile-based assembly. The PUMA array does not require complex external baluns, cable organizers or other external support mechanisms to achieve wideband performance. However, common modes, current loops and surface waves needs to be carefully controlled for proper operation.

a) Common modes, current loops, and surface waves

One of the major issues in PUMA arrays relates to the possible common mode excitation by the feed structure. Common modes occur due to the net vertical current when balanced antennas are fed with unbalanced feeds or when unshielded balanced feeds become unbalanced during E-plane scan. The magnitude and direction of the currents on an unbalanced fed antenna is shown in Fig. 1.11 (a). Common modes can also occur when the antenna length and feed lines are approximately 1λ long [6].

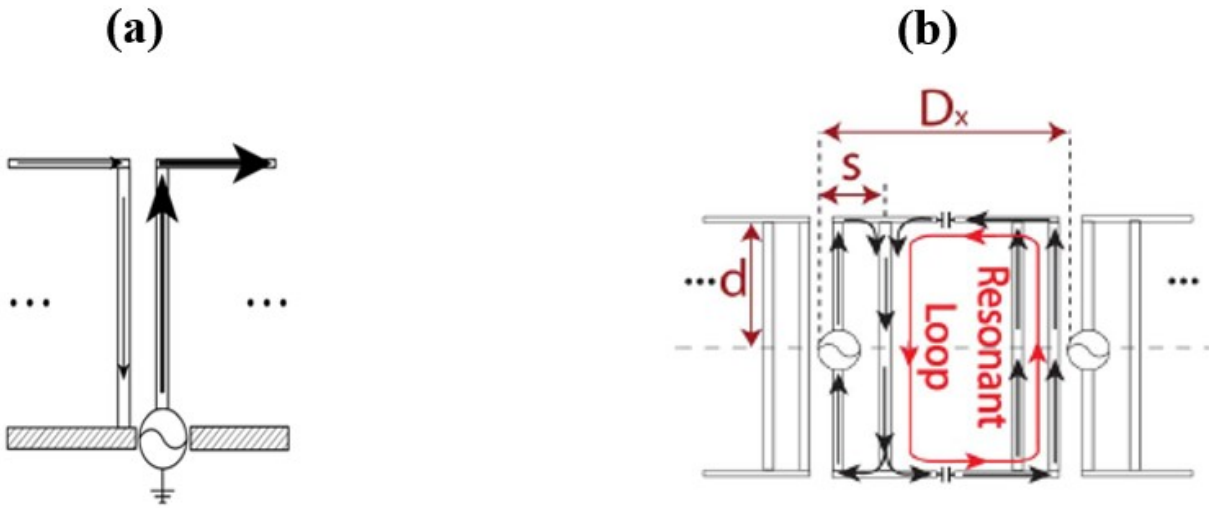

Fig. 1. 11. Common mode and loop currents. (a) Magnitude and direction of the currents on an unbalanced fed antenna [52]. (b) Loop currents on a PUMA array with shorting posts [52].

The unequal currents on the dipole feed arms due to the unbalanced 50 Ω feed, leads to common mode resonance between the mid and high end of the band. The positioning of the shorting posts shown in Fig. 1.11 (b) is used to push the common mode resonance outside the operational band [50]. However, the shorting vias forms two circulating current loops, which alter the low-frequency behavior of the array. To obtain more bandwidth, the shorting vias should be placed closer to the feed lines. This reduces the circumference of the small "driving loop" and increases the circumference of the large "resonant loop" which controls the low-frequency behavior. Alternatively, the shorting post on the grounded arm could be removed to increase the resonant loop size and move the common mode resonance, f_{cm}, above the operating band, and the loop resonance, f_{loop}, below the operating band [52].

PUMA arrays are embedded in thick PTFE dielectric substrates for mechanical support, impedance matching and for simplicity of the dipole arms [53]. This PTFE substrate can trap surface waves which can lead to scan blindness. Perforations on the thick antenna substrate are necessary to reduce its effective permittivity and to help control the amount of surface waves as illustrated in Fig. 1.12.

PUMAv1[50] use a novel unbalanced direct feeding scheme with carefully grounded dipole arms, effectively mitigating in-band common-mode resonances but deteriorating low-end performance.

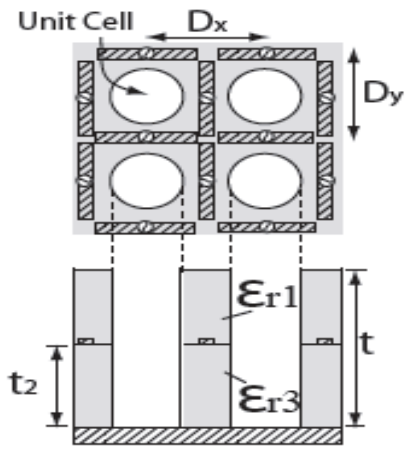

Fig. 1. 12. PUMA feed showing perforations on substrate [52].

Subsequent PUMA arrays have been developed [51, 53] to extend their performance to higher frequencies. However, these arrays require the addition of a backplane matching network and blind vias, which increases their complexity and give rise to high cross-polarization levels. PUMAv3 [51, 53] shown in Fig. 1.13, improves low frequency operation by utilizing capacitively coupled shorting vias in a frequency-selective manner at frequencies afflicted by common-mode resonances. A single shorting via is positioned at the location where the four dipole arms meet and capacitively couples to them, effectively shorting them out near the common-mode frequency, f_{cm}. This arrangement acts as a high-pass filter for the frequency-selective common-mode mitigation and enhances low-frequency inter-element capacitance. Fig. 1.14 shows a comparison between PUMAv1 and PUMAv3 with and without shorting vias.

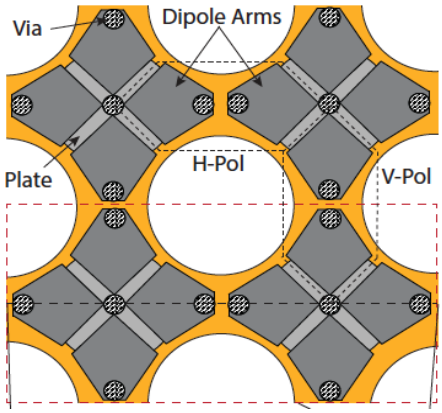

Fig. 1. 13. PUMAv3 [51, 53] with diamond-shaped dipoles and capacitively coupled shorting vias.

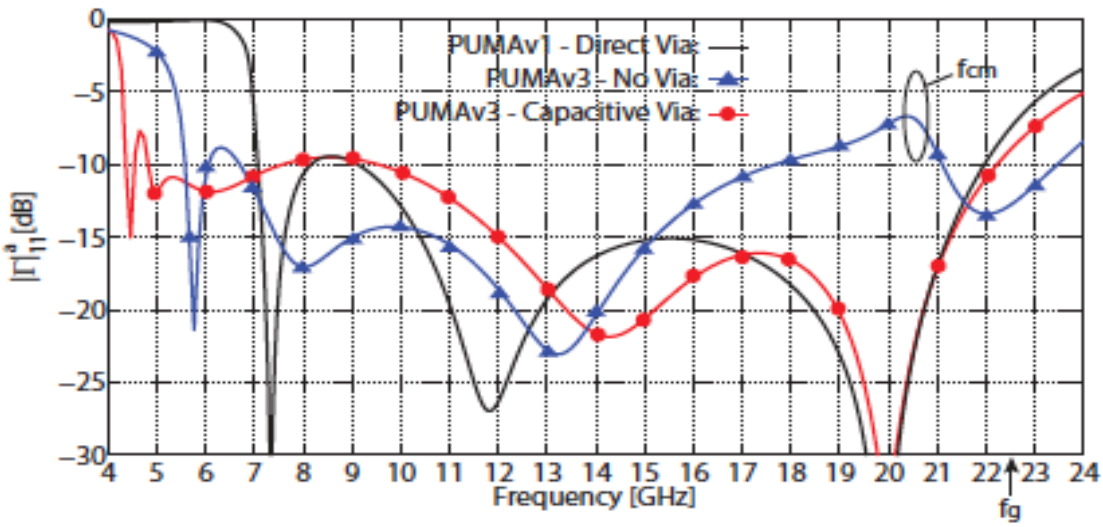

Fig. 1. 14. Comparison between PUMAv1 and PUMAv3 with and without shorting vias [53].

1.3.2.3 Wide angle impedance matching

Another major challenge in TCAA design is the difficulty in compensating for the increased scan loss due to the impedance mismatch at the aperture–air interface. This scan loss is caused by the variations in the array's active impedance that arise from changes in the mutual coupling between the radiating elements as the scan angle and frequency change [54]. To address this problem, wide angle impedance matching (WAIM) superstrates have been employed. Several WAIM schemes have been introduced and used over the years. The earliest techniques involved using thin high-dielectric-constant superstrates in front of an array aperture [11] (see Fig. 1.15) or dielectric slabs adjacent to the array aperture [55, 56]. The above WAIM schemes either improve scanning in one plane at the expense of the others [11], or increase the overall weight of the array and the chance of array blindness [55, 56]. These WAIM techniques were also limited to single frequency or narrow bandwidth operations.

To improve the bandwidth of WAIM structures, multi-layered metamaterial [57, 58] structures and dielectrics [9] have been used. Unfortunately, the overall volume and weight of the array is also increased. To enable wide angle scanning without increasing the volume and weight of antenna arrays, metasurfaces (MS) have been employed. The anisotropic MS-WAIM in [59] provided an improved match for an array of open-ended circular waveguides to free space over several angles.

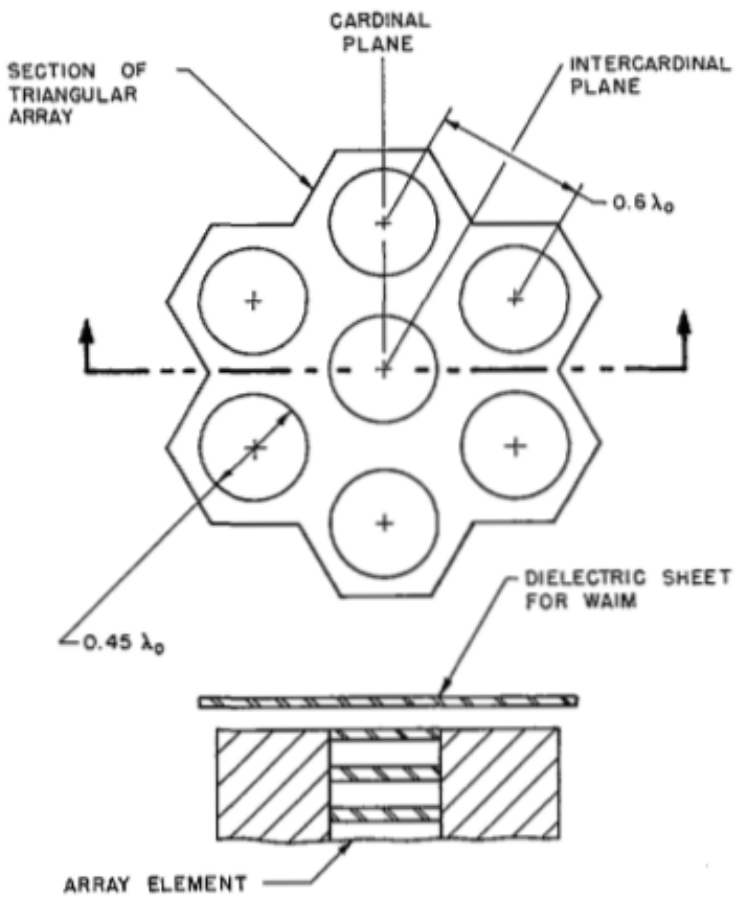

Fig. 1. 15. A waveguide array with a thin high-dielectric-constant WAIM superstrate in front of the array aperture [11].

However, only the scanning results for the H-plane were presented; the associated E-plane and D-plane (diagonal plane of a radiating aperture) results were not reported. Moreover, wide angle scanning over a narrow bandwidth was the focus of the design, which was achieved over a 3.3% bandwidth. The works reported in [11, 59] were extended in [60]. The dielectric slab was replaced with an ultra-thin MS composed of subwavelength split-ring resonators (SRRs) as shown in Fig. 1.16, for an improved scan in the H and D-planes. Simulation results showed that wide angle scanning was achieved over a 20% impedance bandwidth. While there has been some advancement on WAIM metasurfaces, most of the past work has been focused on wide angle scanning over narrow bandwidths [59, 60].

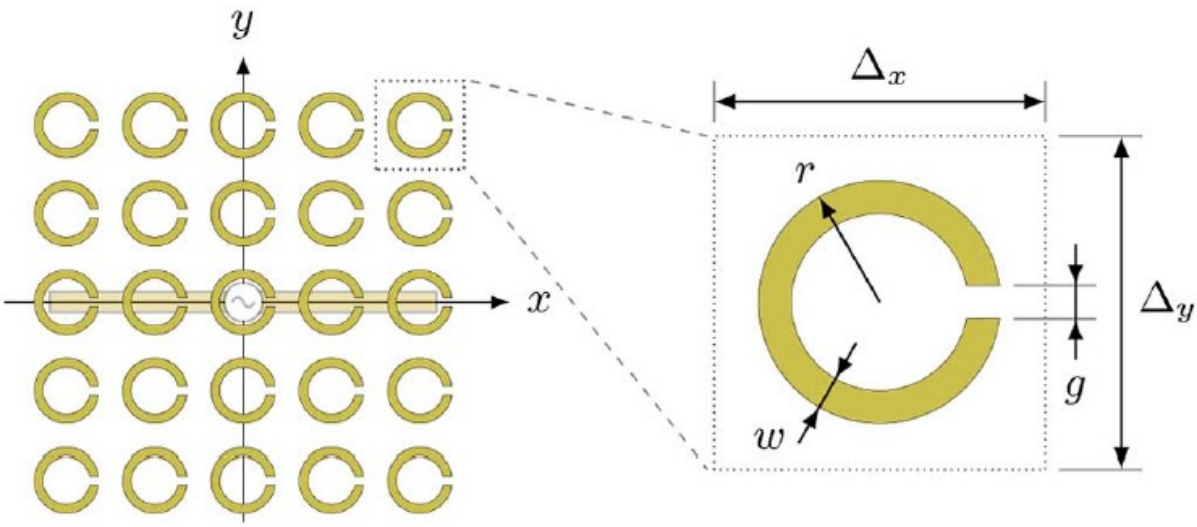

Fig. 1. 16. MS-WAIM composed of 5x5 subwavelength split-ring resonators per unit cell of the antenna array [60].

1.3.3 Fabry-Perot Antenna

Despite the many appealing features of wideband TCAAs, they can be quite costly and the complexity of their feed networks renders them impractical for some applications. A fitting alternative is the highly directive Fabry-Perot antenna (FPA) [13] with a simpler structure, less lossy feed network, and of cheaper cost. In this section, we present a brief survey of existing FPAs including their challenges and the variety of methodologies devised to improve their performance.

Recent enhancement of FPA performance has concentrated on profile reduction, [61 - 63], scan extension, [63 - 66], and bandwidth enhancement [67 - 81]. The majority of the research effort has been concentrated on different methods of enhancing the gain bandwidth (GBW). In the early days, the achievable bandwidth was extremely narrow and usually < 3% [67, 68]. Over the years, bandwidth has steadily increased by adopting three main techniques, namely, array feed source [69 - 72], phase correcting structures (PCS) [73 - 77], and positive reflection phase structures [78 - 81].

The use of an array instead of a single antenna to excite the Fabry-Perot cavity has been shown to improve both the directivity and GBW [69 - 72]. In [71], a 3 dB GBW of 17% and a maximum directivity of 23 dB is obtained using a multisource fed FPA with a double-layer frequency selective

surface (FSS) superstrate. The multi-feed system allows relatively large array spacings (larger than a wavelength) without obtaining high sidelobe levels. The sidelobe levels are spatially filtered by the FPA due to the interlaced radiating aperture as shown on the right hand side of Fig. 1.17. However, due to the requirements of a feed network, some of the inherent qualities of a FPA such as simplicity and radiation efficiency are compromised.

PCSs have been constructed using tapered-size elements [73, 74], dielectrics with a permittivity gradient in the transverse direction [75, 77] and shaped ground planes [76]. They provide a uniform phase distribution at the antenna aperture, which can lead to bandwidth enhancement. Phase correction is achieved either by gradually changing the size of the elements, the superstrate permittivity, or the cavity height (by changing the shape of the ground plane) to compensate for the difference in path lengths of the fields arriving at the aperture. In [74], a near zero index (NZI) metasurface (MS)

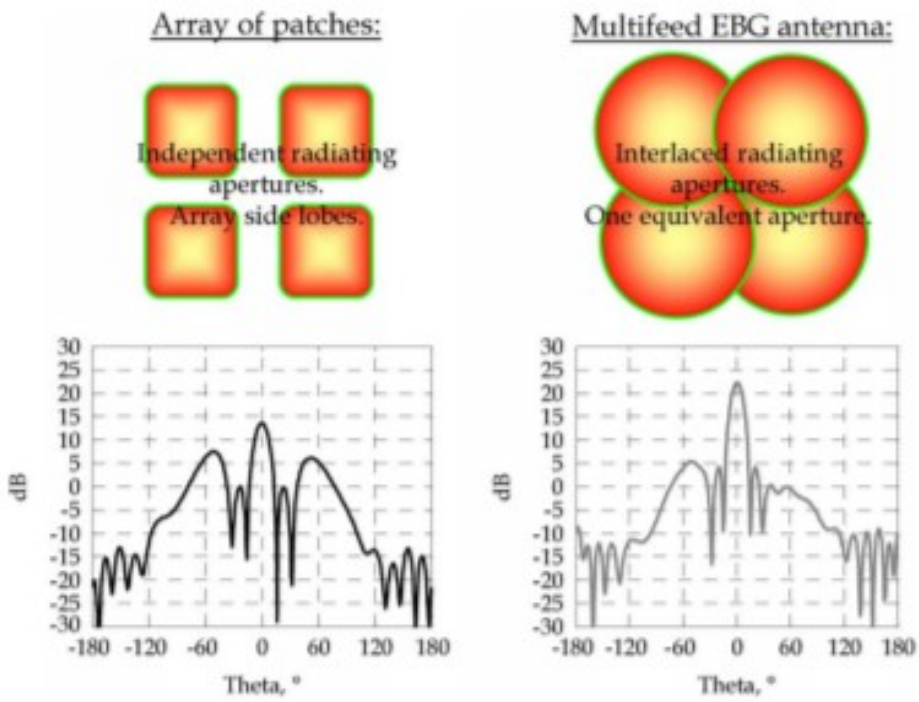

Fig. 1. 17. FPA spatial filtering due to interlaced radiating apertures (right) as opposed to independently radiating apertures (left) [71].

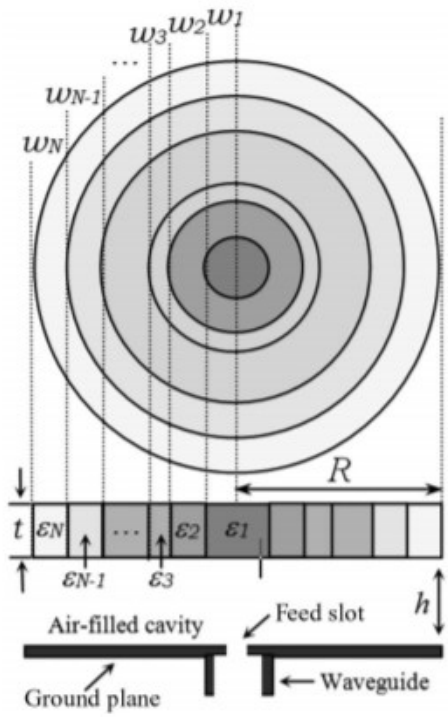

Fig. 1. 18. A typical phase correcting superstrate structure with a permittivity gradient from the centre to the edges [77].

made up of tapered-size square-ring unit cells is used to increase the 3-dB GBW and directivity of a FPA to 20.3% and 17.9 dBi respectively. The permittivity gradient PCSs have shown much improvement in directivity-bandwidth products (DBWP). The FPA shown in Fig. 1.18 [77] has a 3-dB directivity bandwidth (DBW) of 52.9% and a peak directivity of 16.4 dBi was demonstrated. However, the total antenna profile is $1.01\lambda_C$, where λ_C is the free space wavelength at the central frequency.

Various methods have been devised to make the reflection phase of the partially reflective surface (PRS) increase linearly with frequency as this has been shown to maximize the GBW [78]. Some of these methods include using multi-layered metasurface superstrates with sub-wavelength cavities [79], single-layer double-sided complementary [80] and dipole-type [82] FSSs, and multi-layered dielectric superstrates [80]. An FPA in [79] with a three layer metamaterial superstrate and a total height of $0.68\lambda_C$ achieved a 3-dB bandwidth of 10.7% and a directivity of 16.9 dBi. With the aid of the Metamaterial superstrates, the profile of the antenna is kept low even though it uses multiple layers as

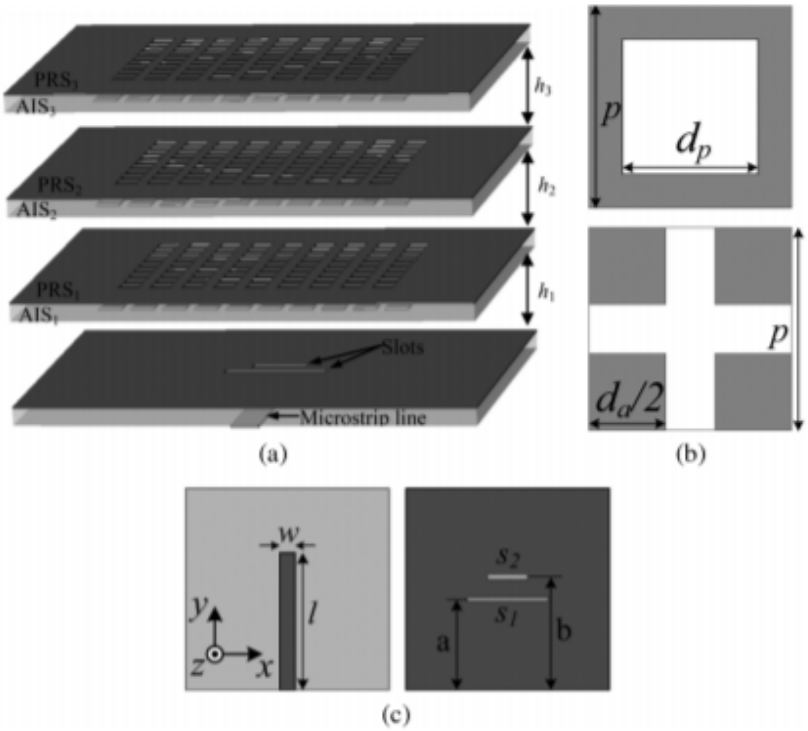

Fig. 1. 19. Multi-layered Metamaterial superstrate FPA. (a) Perspective view of antenna. (b) Top and bottom unit cells of superstrates. (c) Back and front view of ground plane with the microstrip line and slots [79].

shown in Fig. 1.19. The bandwidth though, is still quite narrow. In [80], a 3-dB GBW of 28%, with a peak gain of 13.8 dBi in the X-band was also achieved.

1.4 Thesis Organization and Main Contributions

The contents of this Thesis are organized as follows. Chapter 1, presents the background and significance of the research problem and the intended objectives. A detailed literature review on tightly coupled antenna arrays (TCAA) and Fabry-Perot antennas (FPA) is presented highlighting the current problems and existing solutions.

Chapter 2 present the design, analysis, and practical realization of a novel ultra-thin metasurface (MS) based wide angle impedance matching (WAIM) layer that can achieve both wideband operation and wide angle scanning. The wideband operation of the single sided (SS) MS-WAIM is obtained by incorporating tight coupling within and between the multi-resonant elements. The SS MS-WAIM effectively addresses the problem of scan loss in antenna arrays by utilizing tightly-coupled unequal arm Jerusalem cross (TC-UAJC) elements. The SS MS-WAIM is designed for an effective permeability value near zero over a wide bandwidth ($\mu_{eff} \approx 0$). As a result, it is able to transform the cylindrical waves from the array into plane waves with minimal phase variation to enable wide angle scanning. This waveform transformation also help to lower the array profile since all the energy is concentrated in the forward direction. The metasurface is integrated with a lumped port fed TCAA to validate its feasibility. The detailed design process of the TCAA is left for Chapter 3. It is shown that the metasurface-array combination provides improved scanning along the E (72°), H (80°), and D (79°) planes over a 6:1 impedance bandwidth without the need for bulky dielectrics or multi-layered structures, resulting in a light-weight antenna system with reduced profiles. The major contributions in this Chapter are:

1. The development of an ultra-thin SS MS-WAIM superstrate that reduces the profile and weight of antenna arrays.
2. The development of a SS MS-WAIM that operates over a very wide bandwidth.
3. The development of a SS MS-WAIM that can facilitate very wide scanning angles across all planes.

Chapter 3 develops the theory and operating principles of the component parts of the TCAA. In addition, an improved version of the SS MS-WAIM first introduced in chapter 2 is developed. Detailed

array analysis and design guidelines are presented for several thicknesses of the double sided (DS) MS-WAIM. A fully characterized 10 x 10 TCAA prototype with a very high figure of merit is presented that validates the design concepts and simulation methodology employed in this work. An improved design of the fabricated array has a performance that approaches the fundamental limits of low profile arrays with a bandwidth of 5.5:1, a maximum scan range of 80° along the E-plane, and a profile of ~$\lambda_L/12$, where λ_L is the wavelength at the lowest frequency of operation. This excellent performance is enabled by a newly introduced feed network that is simple, inexpensive, and extremely wideband; in conjunction with the novel MS-WAIMs. The new wideband, low-profile feed network is composed of meandered impedance transformer and balun sections. The feed is designed based on Klopfenstein tapered microstrip lines. It can provide more than 6:1 impedance bandwidth while maintaining a high level of current balance. An array figure of merit (P_A) was also calculated for several TCAA designs, to make comparisons with similar designs in the literature. The figure of merit values of the four designs presented in Chapter 3 are reproduced in Fig. 1.20 below, shown in bold grey, green, orange, and red. The figure of merit value of the optimum design, $P_A = 5.49$, is highest reported to date.

The major contributions in this Chapter are:

1. The development of an improved version of the SS MS-WAIM superstrate introduced in Chapter 2.
2. The introduction of a new feed network that is simple, inexpensive, and extremely wideband, constructed from Klopfenstein tapered microstrip lines.
3. The design, fabrication and testing of a fully characterized 10 x 10 TCAA prototype with a very high figure of merit.
4. Development of two optimized TCAA designs with the highest array figures of merit to date.

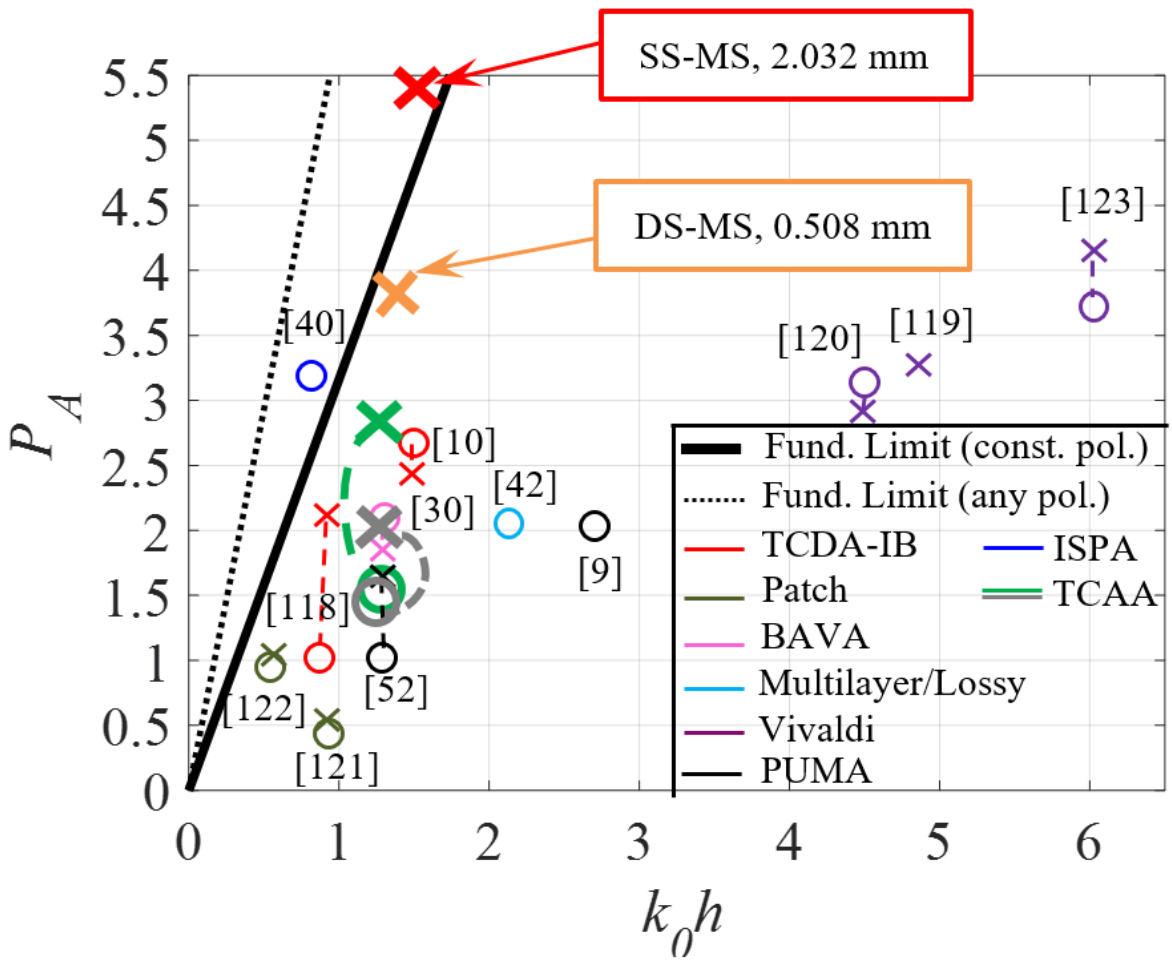

Fig. 1. 20. Performance comparison of wideband PEC-backed antenna arrays using the array figure of merit (P_A) versus electrical thickness (k_0h) plot. This figure is reproduced here courtesy of the work done in [108] with the addition of some recently reported works. The fabricated array and the working design that was used to establish the design guidelines are shown in bold grey and bold green respectively. The improved designs are shown in bold orange and bold red. The circles represent broadside performance and the crosses represent scanning performance along the E or H planes.

Chapter 4 presents an alternative solution to TCAAs in the form of a wideband, low-profile, Fabry-Perot antenna (FPA) empowered by a novel multi-resonant metasurface (MS) superstrate. Unlike the usual method of bandwidth extension using multiple superstrate layers, this new approach uses a single multi-resonant superstrate to create multiple resonances satisfying the resonance condition. This ensures substantial bandwidth extension without further increase in height. The superstrate consists of a patch-type and an aperture-type MS (PMS and AMS) placed on the top and bottom surfaces, of a dielectric. The PMS behaves like a low-pass filter and the AMS acts like a conventional partially

reflective surface with a high-pass filter response. In addition, by inserting varied thicknesses of dielectric slabs within the cavity, the 1-dB or 3-dB gain bandwidths can be enhanced while reducing the antenna height. Using this new method, two antennas are designed, fabricated and measured with an aperture efficiency of 64%. The 3-dB gain bandwidths of the two designs are > 40%. Because of the small foot print of the antenna, it is suitable for space limited applications or as an element in a sparse antenna array for further increases in directivity. At the same time, the number of active elements will be significantly reduced compared to the dense TCAAs leading to substantial cost reductions.

The major contributions in this Chapter are:

1. The development of a novel multi-resonant metasurface (MS) superstrate that can facilitate wide bandwidth, low profile FPAs.
2. Presentation of a viable cost effective alternative to dense dipole arrays

Finally, in Chapter 5 is presented the conclusions, recommendations and future work.

Section I - Tightly Coupled Antenna Arrays

Chapter 2 – Ultra-thin Metasurface for Wide Bandwidth, Wide Angle Impedance Matching

2.1 Chapter Introduction

This Chapter will present the design, analysis, and practical realization of one of the major components in ultra-wideband antenna array design; namely, a wideband metasurface (MS) based wide angle impedance matching (WAIM) layer. MSs are planar, two-dimensional equivalents of metamaterials (MTM). MTMs are engineered materials composed of sub-wavelength unit cells with unique properties that may not usually be available in nature [84 – 88]. Modification of the MTM geometry can be used to tune its electric and or magnetic response thereby producing tailored values of permittivity or permeability. The resulting modification of the effective material properties may also affect the MTM's transmission, reflection, absorption, and coupling capabilities [89]. Due to the thickness and weight requirement of MTMs, MSs are usually preferred. Metasurfaces also planar, easier to fabricate, and weigh much less than 3-D MTM structures. They are also less lossy due to their reduced size [90]. Some applications of MSs include: absorbers [91 – 93], radar cross section reduction surfaces [94], wave front shapers [95], and wide angle impedance matching layers [59, 60]. WAIMs are usually employed to minimize the amount of scan loss in phased array antennas.

In this Chapter, we propose a new ultra-thin single side (SS) MS-WAIM that can achieve both wideband operation and wide angle scanning. The SS MS-WAIM is composed of tightly-coupled unequal arm Jerusalem cross (TC-UAJC) elements. The TC-UAJC is an evolved version of the Jerusalem cross [96]. The wide bandwidth is obtained by taking advantage of the tight coupling within and between the multi-resonant elements. The band of operation is located much lower than the SS MS-WAIM's resonance frequency to avoid the associated highly dispersive and lossy regions [59]. These losses are due to the total power absorbed by the SS MS-WAIM near its resonance frequency. At frequencies near its resonance, the field concentration per unit cell in the metallic layers of the structure is increased, which in turn leads to an increase in the resistive heating [97]. This SS MS-WAIM is fairly

2.2 Metasurface WAIM Design

2.2.1 Unit Cell Structure and Operation

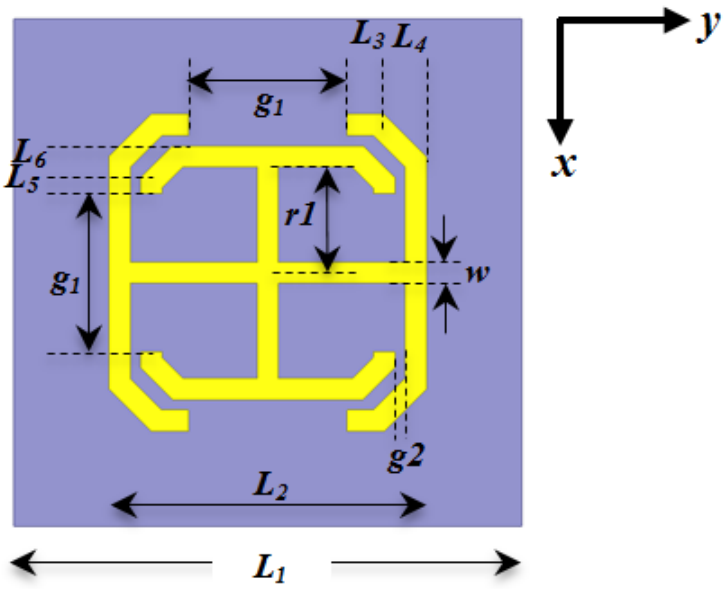

Fig. 2. 1. Top view of the SS MS-WAIM unit cell geometry. The optimized unit cell dimensions for the SS MS-WAIM are: $w = 0.2$ *mm*, $H_{sub} = 0.254$ *mm*, $g_1 = 1.5$ *mm*, $g_2 = 0.1$ *mm*, $L_1 = 4.8$ *mm*, $L_2 = 3.0$ *mm*, $L_3 = 0.35$ *mm*, $L_4 = 0.4$ *mm*, $L_5 = 0.15$ *mm*, $L_6 = 0.3$ *mm*, and $r_1 = 1.0$ *mm*.

insensitive to the changing phases of the signals incident upon it over a wide bandwidth. As a result, it is able to maintain its performance for scanning angles of up to 70° from the normal to the SS MS-WAIM for both transverse magnetic (TM) and transverse electric (TE) polarized incident waves. The metasurface is integrated with a tightly coupled antenna array to validate its feasibility. It is shown that the metasurface-array combination provides improved scanning along the E (72°), H (80°), and D (79°) planes over a 6:1 impedance bandwidth without the need for bulky dielectrics or multi-layered structures, resulting in a light-weight antenna system with reduced profiles. The unit cell configuration of the SS MS-WAIM is depicted in Fig. 2.1. The metallic pieces (in yellow) are etched on the top surface of a dielectric substrate. The TC-UAJC element consists of two orthogonal, bent-arm capacitively-loaded-strips. They are tuned for the desired operating frequencies. These arm segments provide inductance; the gaps between the extremities of its bent arms provide capacitance.

In order to minimize the variation of the array active reflection coefficients at wider scan angles, the SS MS-WAIM introduces a capacitive reactance below its resonance frequency point to counteract the effects of the array's inductively reactive ground plane. The SS MS-WAIM serves as a wideband impedance transformer between the array aperture and free space. To ensure a low loss SS MS-WAIM, its operational bandwidth is located way below its resonance frequency.

The TC-UAJC element presented here uses three main techniques to achieve optimal transmission and minimal reflection over a wide bandwidth below its resonance frequencies. Firstly, tightly coupled elements are used to increase their inter-element capacitance. It should be noted that smaller inter-element spacing produces large bandwidths but can lower the resonance frequency if the resulting capacitance is excessive [98, 99]. The smaller inter element spacing combined with the subwavelength nature of the SS MS-WAIM elements allows field propagation to neighbouring elements and the elimination of impedance variations to give rise to large bandwidths [96]. In the extreme case when the elements are very small and tightly packed, the current distribution across the SS MS-WAIM approaches the Wheeler uniform current sheet concept [32]. The reduction in resonance frequency comes as a result of the well-known relationship, $\omega = 1/\sqrt{LC}$. Secondly, the horizontal and vertical arms of the TC-UAJC element are tightly coupled to each other for increased intra-element capacitance and thin traces are used for increased inductance, thereby enabling both compactness and an inherently wideband element [100]. Thirdly, the constituent parts of the element provide closely spaced multiple resonances [101] which combine to produce a wide bandwidth.

2.2.2 Metasurface Design and Analysis

The proposed SS MS-WAIM is designed and optimized using the commercially available ANSYS High Frequency Structure Simulator, ANSYS-HFSS [102]. A SS MS-WAIM was simulated and an initial optimization was carried out to obtain the optimum transmission and reflection values. A prototype of the optimized SS MS-WAIM was fabricated based on these optimized values and was tested to verify its operation. The effective medium parameters of the SS MS-WAIM were also extracted from the S-parameters using MATLAB [103] and the method described in [104]. To demonstrate the SS MS-

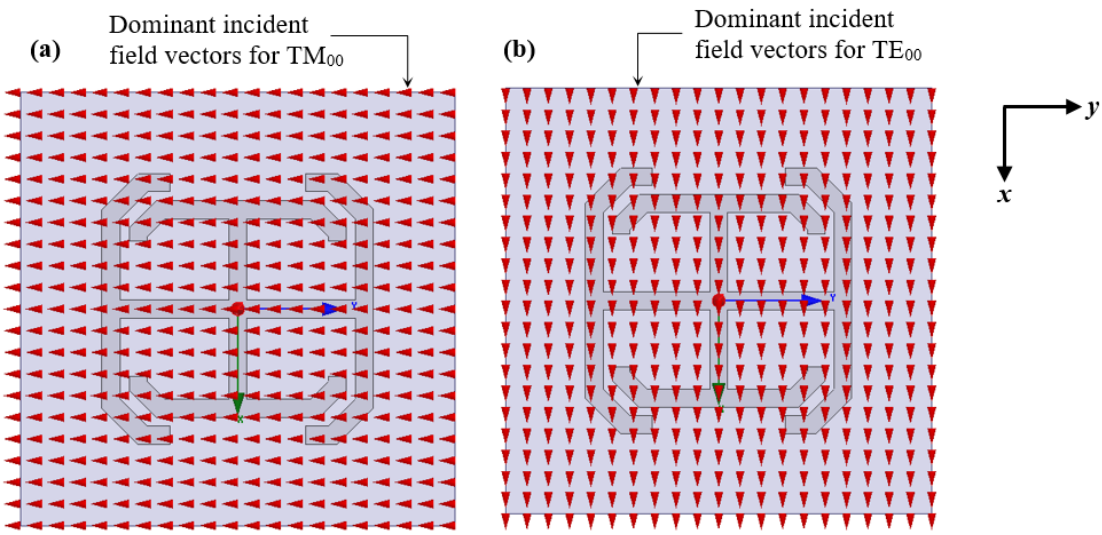

Fig. 2. 2. Top view of the unit cell. **(a)** The TM_{00} floquet mode fields. **(b)** The TE_{00} Floquet mode fields at the face of the top Floquet port.

WAIM capability across a wide frequency range, it is then integrated with a tightly coupled antenna array (TCAA) in an HFSS model for a final optimization. The antenna array consists of a set of tightly coupled dipole antennas [9] with less than 0.4 l spacing between them.

2.2.2.1 Single sided metasurface

The single sided SS MS-WAIM was modeled using master-slave periodic boundary conditions in the *x* and *y* directions of the unit cell of Fig. 2.1. The periodic boundaries enforce a linearly progressive phase shift between the master and slave boundary pairs with uniform amplitude to enable beam scanning in the required directions. Two Floquet ports were used to illuminate both sides of the SS MS-WAIM, one located at the top face and the other at the bottom face of the model's air box. The length of the air box was chosen to ensure that all higher order modes other than the two propagating zeroth-order Floquet modes experience at least 70 dB of attenuation.

The copper-cladded Rogers RT/Duroid™ 5880 substrate with a relative dielectric constant of *2.2* and a height of H_{sub} = 0.254 *mm* was selected. The TC-UAJC element was etched on the 17 *mm* thick copper sheet on its upper surface. The HFSS solution frequency was selected to be 20 GHz for a (0.5 – 20) GHz frequency sweep. The maximum scan volume was $\theta = 70^o$. To minimize the simulation time and the amount of discretization, the metals in the HFSS model were taken to be perfect electric

conductors (PECs). The zeroth-order Floquet modes, TM_{00} and TE_{00}, were used for scanning in the *y-z* and *x-z* planes respectively as shown in Fig. 2.2. The electric field of the TM_{00} Floquet mode is parallel to the plane of incidence (along the *y*-direction) and the electric field of the TE_{00} Floquet mode is perpendicular to the plane of incidence (along the *x*-direction).

To determine the orientation of an antenna with respect to the TC-UAJC element, the surface current distribution on the element is studied. The resulting surface current densities on the element for the corresponding TE and TM reflection (i.e., $|S_{11}| \longrightarrow 0$) and transmission (i.e., $|S_{21}| \longrightarrow 0$) resonances for

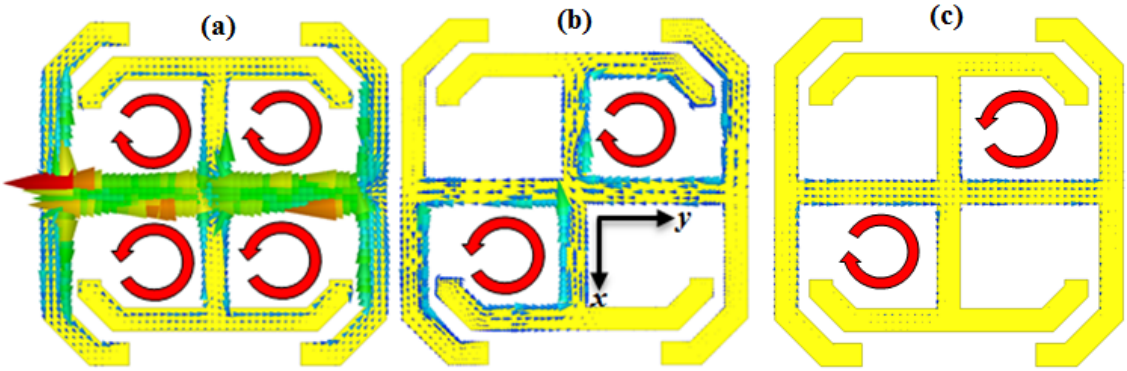

Fig. 2. 3. The surface current densities on the TC-UAJC element for normal incidence showing circulating current loops. **(a)** TM reflection resonance at 15.8 GHz. **(b)** TE reflection resonance at 19.5 GHz. **(c)** TE transmission resonance at 19.7 GHz.

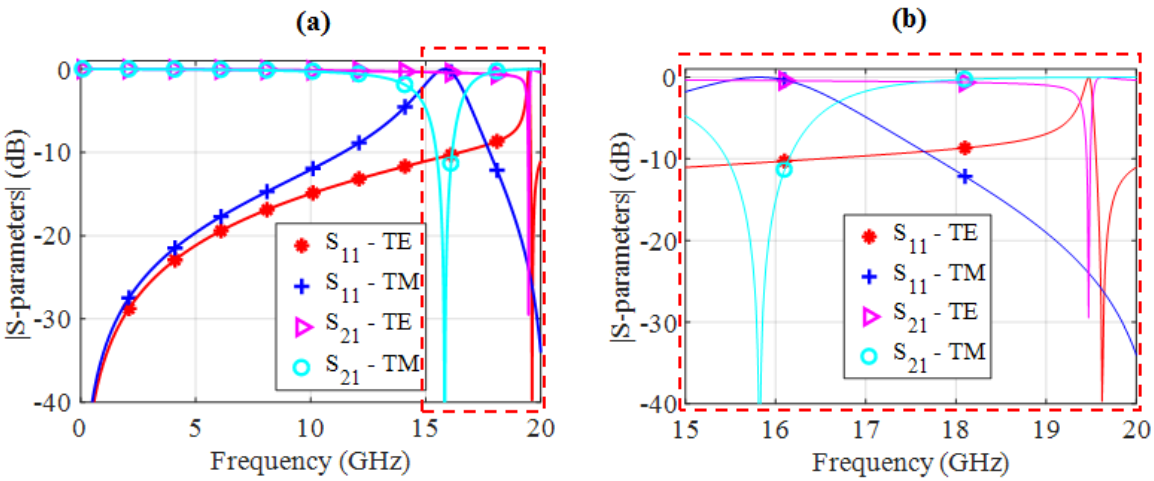

Fig. 2. 4. Magnitudes of the S-parameters for normal incidence. **(a)** TE and TM excitations of the TC-UAJC element. **(b)** An expanded view showing the first TM reflection resonance at 15.8 GHz and the first TE reflection resonance at 19.5 GHz. A TE transmission resonance can also be seen at 19.7 GHz.

normal incidence are shown in Fig. 2.3. For the TE reflection and transmission resonance cases, the element is only weakly excited. For the TM reflection resonance case on the other hand, the element is strongly excited with opposite sense circulating current loops. The circulating surface currents flow in equal and opposite directions in adjacent regions of the SS MS-WAIM indicating that the magnetic fields created cancel out each other leaving no net magnetic response. Current flow is maximum along the *y*-direction suggesting that the optimum radiator and SS MS-WAIM coupling is achieved when a radiator's E-plane is aligned with the *y*-axis of the SS MS-WAIM.

For a MS to act as an efficient wideband WAIM, it must be able to fulfil certain basic criteria. Firstly, the intended operational frequencies of the antenna array should be considerably lower than the resonance frequencies of the MS to avoid the highly dispersive and lossy regions [59]. Secondly, it should have little effect on the phases of the signals incident upon it during scan across the whole band of interest in order to facilitate the same output response. Thirdly, it should be thin and light weight to help reduce the volume and profile of the antenna array.

In Fig. 2.4, we show with the simulated scattering parameters (S-parameters) at broadside, that the reflection resonance frequencies of the MS are above 15.8 GHz, which is much higher than the intended operational frequencies of the antenna array (below 5.0 GHz). The return loss for both the TE and TM polarizations is greater than 20 dB across the frequency band of interest and, hence, the insertion loss is virtually zero. Due to the unequal lengths of the two arms of the TC-UAJC element, they exhibit slightly different reflection resonance frequencies when illuminated by the TM and TE incident waves. Each resonance frequency is directly proportional to the unwound length, L, of the TC-UAJC element [105]. The first reflection resonance occurs at 15.8 GHz for the TM excitation when the electric field is along the longer arm; the second one occurs at 19.5 GHz for the TE excitation when it is along the shorter arm.

The transmission phase variation with frequency for the TM polarized incident fields for various angles of incidence is shown in Fig. 2.5. The phase varies by only 3° for a 0° - 70° change in the incident angle. This small change in phase implies that the MS will hardly alter the phase of electromagnetic

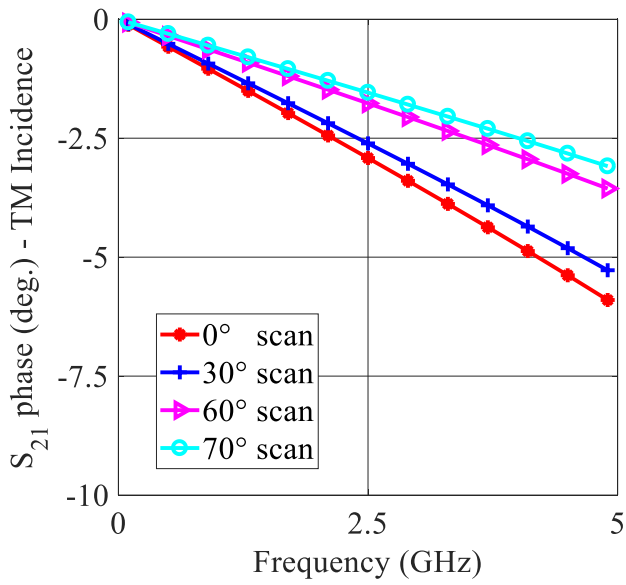

Fig. 2. 5. Transmission phase variation with frequency for the TM polarized incident fields for various angles of incidence.

waves traversing it [91]. The resulting SS MS-WAIM is very thin and light weight. It is only *0.254 mm* thick.

2.2.2.2 Design parameter studies

One of the major goals was to make the reflection magnitude and transmission phase across the frequency band of interest as small as possible without having an adverse impact on the bandwidth of the SS MS-WAIM. Consequently, several of the design parameters were studied to determine the values that produced the minimum reflection magnitude and transmission phase. It was found that the parameters g_1, g_2, r_1, and H_{sub} have the most impact on the SS MS-WAIM performance.

The effects of g_1 on the reflection magnitude and transmission phase values are shown in Figs. 2. 6 (a) and 2.6 (e), respectively. Increasing g_1 reduces both the reflection magnitude and transmission phase values. However, further increase beyond *1 mm* has negligible impact.

The effects of g_2 are shown in Figs. 2.6 (b) and 2.6 (f). Decreasing g_2 gives decreasing values for both the magnitude and phase. The value of g_2 is limited by manufacturing tolerances so it has been confined to a minimum value of *0.1 mm*. The parameters g_1 and g_2 control the amount of intra-element

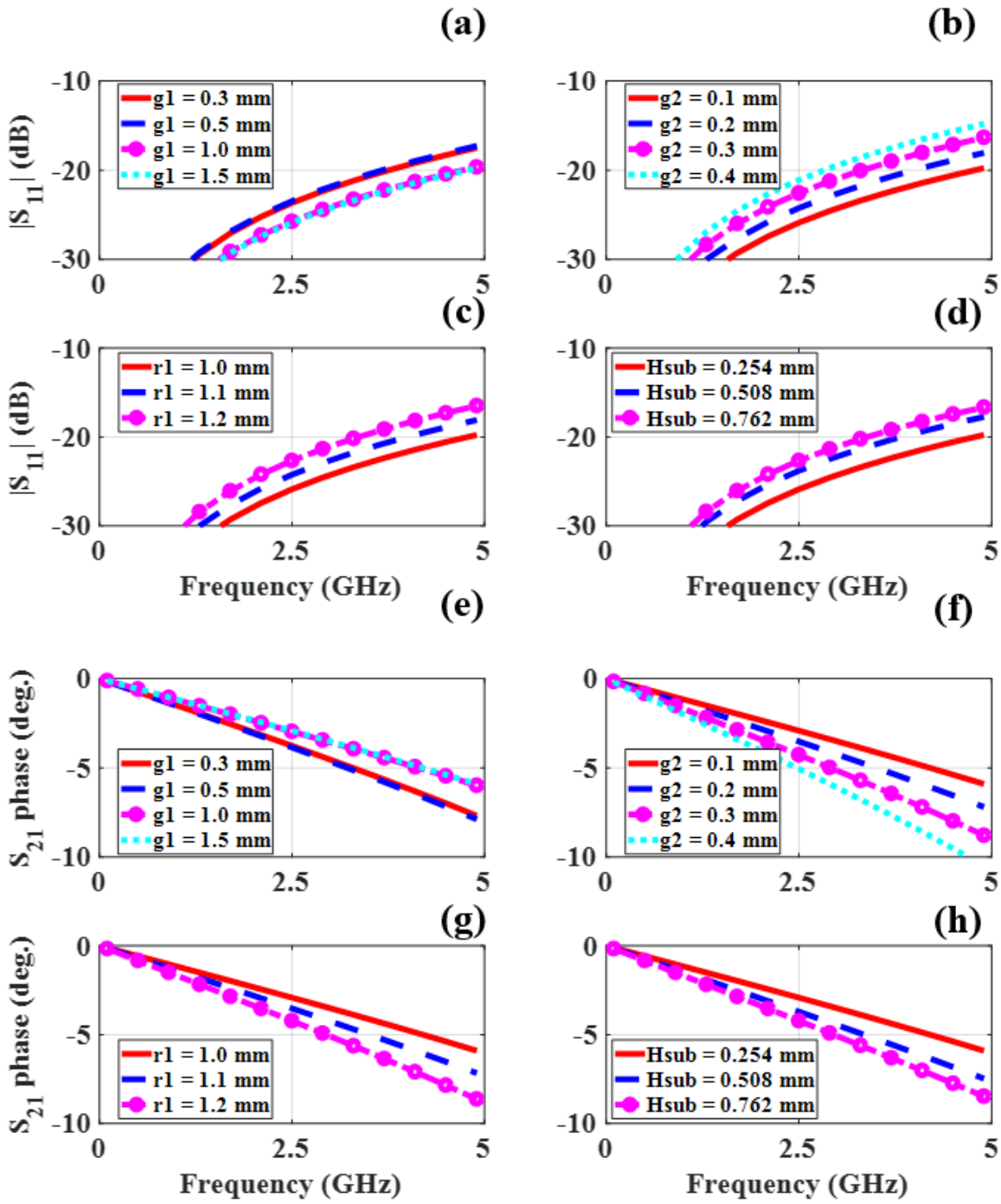

Fig. 2. 6. The effects of various SS MS-WAIM design parameters on the reflection magnitude **(a – d)** and transmission phase **(e – h)** as functions of the excitation frequency for the TM incidence case. **(a)** and **(e)** g1. **(b)** and **(f)** g2. **(c)** and **(g)** r1. **(d)** and **(h)** Hsub.

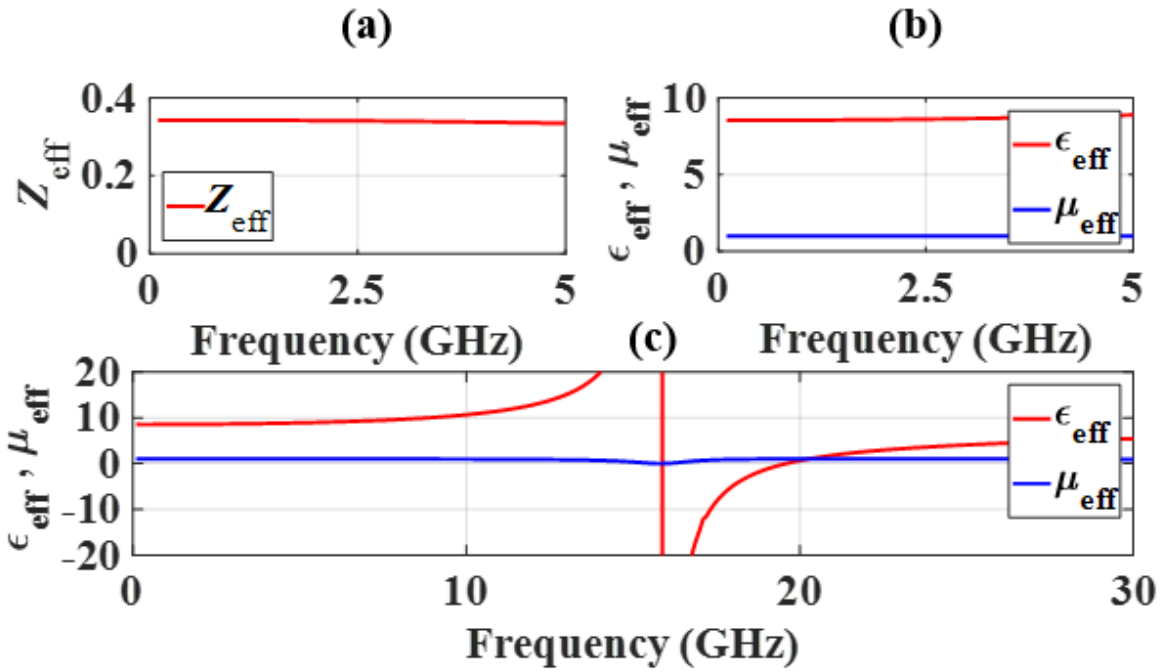

Fig. 2. 7. Extracted parameters of the SS MS-WAIM for the TM excitation. **(a)** Effective impedance. **(b)** Effective permittivity and effective permeability at the frequencies of interest and **(c)** across the whole band showing TM resonance at 15.8 GHz.

coupling. Smaller values of g_2 indicate a tighter coupling between the horizontal and vertical arms of the TC-UAJC resulting in a large coupling capacitance. When this coupling capacitance is combined with the high loop inductance produced by the thin traces of the structure, the element bandwidth is enhanced.

Figs. 2.6 (c) and 2.6 (g) show the effects of r_1. Decreasing r_1 gives decreasing values for both the magnitude and phase. The minimum value of r_1 has been restricted to *1 mm* for ease of fabrication. The resonance frequency of the unit cell is essentially determined by r_1. Smaller values of r_1 lead to smaller elements with correspondingly higher resonance frequencies, creating a wider separation between the frequency band of interest and the element resonance frequency. The result from this wide separation is a smaller transmission phase variation with respect to the scan angle. The inter-element coupling is controlled by the values of r_1.

The effects of H_{sub} are shown in Figs. 2.6 (d) and 2.6 (h). Decreasing H_{sub} gives decreasing values for both the magnitude and phase of the S-parameters. Thinner substrates, i.e., smaller H_{sub}, ensure higher transmission and minimal reflection of the incident signal. From all of these reflection magnitude and transmission phase plots given in Fig. 2.6, the optimum values are: $g_1 = 1.5$ *mm*, $g_2 = 0.1$ *mm, r1= 1.0 mm* and *Hsub = 0.254 mm.*

2.2.2.3 Parameter extraction

To further characterize the SS MS-WAIM's response, it is of interest to determine its effective material and wave parameters. Various techniques have been proposed for retrieving the effective parameters of metamaterials and metasurfaces. One of those techniques, based on the Kramers-Kronig relationship [106, 107], makes use of the simulated or measured S-parameters. A version of this technique, described in [104], is used to extract the effective wave impedance Z_{eff}, the effective dielectric constant ε_{eff}, and the effective permeability μ_{eff} of our SS MS-WAIM from its simulated S-parameters.

For normal plane wave incidence on a homogeneous slab, the wave impedance and the refractive index are related to the S-parameters as follows:

$$S_{11} = \frac{R_{01}(1 - e^{i2N_{eff}k_0 d_{eff}})}{1 - R_{01}^2 e^{i2N_{eff}k_0 d_{eff}}} \tag{2.1}$$

$$S_{21} = \frac{(1 - R_{01}^2)e^{i2N_{eff}k_0 d_{eff}})}{1 - R_{01}^2 e^{i2N_{eff}k_0 d_{eff}}} \tag{2.2}$$

where $R_{01} = (Z_{eff} - 1)/(Z_{eff} + 1)$, $Z_{eff}(\omega)$ is the complex wave impedance, $N_{eff}(\omega) = n_{eff}(\omega) + ik_{eff}(\omega)$ is the complex refractive index, $k_{eff}(\omega)$ is the extinction coefficient, d_{eff} is the effective thickness (for metamaterials with symmetrical geometry in the direction of propagation, the effective thickness is the sum of the length of the unit cells it contains), k_0 is the free space wave number, and ω is the angular frequency. Substituting R_{01} into (2.1) and (2.2) we arrive at,

$$Z_{eff} = \pm\sqrt{\frac{(1 + S_{11})^2 - S_{21}^2}{(1 - S_{11})^2 - S_{21}^2}} \tag{2.3}$$

$$e^{i2N_{eff}k_0d_{eff}} = \frac{S_{11}}{1 - S_{11}R_{01}} = X \pm j\sqrt{1 - X^2} \tag{2.4}$$

where $X = \frac{1}{2S_{21}(1-S_{11}^2+S_{21}^2)}$. For passive materials, the signs of (2.3) and (2.4) are determined by imposing the conditions, Re (Z_{eff}) ≥ 0 & Im (N_{eff}) ≥ 0. From the above expressions,

$$N_{eff} = \frac{1}{k_0d_{eff}}\{Im[\ln(e^{i2N_{eff}k_0d_{eff}})] + 2m\pi - iRe[\ln(e^{i2N_{eff}k_0d_{eff}})]\} \tag{2.5}$$

$$[N_{eff} = n_{eff} + k_{eff}]$$

$$n_{eff} = \frac{1}{k_0d_{eff}}\{Im[\ln(e^{i2N_{eff}k_0d_{eff}})] + 2m\pi\} = n_{eff}^0 + \frac{2m\pi}{k_0d_{eff}} \tag{2.6}$$

$$k_{eff} = -\frac{Re[\ln(e^{i2N_{eff}k_0d_{eff}})]}{k_0d_{eff}} \tag{2.7}$$

where m is an integer denoting the branch index and n_{eff}^0 is the refractive index corresponding to the principal branch of the logarithmic function ($m = 0$). The imaginary part of the complex refractive index is not affected by the branches of the logarithmic function. Therefore, it can be calculated from (2.7) without ambiguity. The calculation of the real part of the refractive index involves the evaluation of a complex multi-valued logarithmic function. This uncertainty is referred as the branching problem. To remove this ambiguity, the Kramers-Kronig relation can be applied to estimate the real part of the complex refractive index using:

$$n^{KK}(\omega') = 1 + \frac{2}{\pi}\mathrm{P}\int_0^\infty \frac{\omega k_{eff}(\omega)}{\omega^2 - \omega'^2}d\omega \tag{2.8}$$

where P denotes the principal value of the improper integral. The integral to infinity implies that the S-parameters must be known for the entire frequency range. Since this is usually not possible, a truncation is required to provide an approximation of the refractive index. To obtain more accurate results, the simulation or measurement should be carried out over a very wide frequency range well above and below the resonance frequencies.

Equation (2.8) can be evaluated numerically. Substituting the result obtained from (2.8) into (2.6) the branch number can be obtained.

$$m = Round[(n^{KK} - n_{eff}^{0})\frac{k_0 d_{eff}}{2\pi}] \tag{2.9}$$

Inserting this value of m into (2.5), the exact value of the complex refractive index can be obtained by selecting those branches of the logarithmic function which are closest to those predicted by the Kramers-Kronig relation. The effective magnetic permeability and effective electric permittivity, which determines the macroscopic behaviour of the metasurface, can then be calculated from the relations,

$$\mu_{eff} = N_{eff} Z_{eff} \tag{2.10}$$

$$\varepsilon_{eff} = \frac{N_{eff}}{Z_{eff}} \tag{2.11}$$

During the extraction process, the SS MS-WAIM was assumed to be homogeneous with an effective thickness equal to that of the substrate upon which the TC-UAJC element resides. Homogenization is justified due to the sub-wavelength nature of the SS MS-WAIM inclusions. Owing to the SS MS-WAIM's very thin nature in the direction of propagation, the extraction process was expected to proceed smoothly. Moreover, its thinness led to virtually the same results relative to each port of the unit cell. In order to obtain more complete extraction results, the SS MS-WAIM was simulated up to 30 GHz for the TM excitation, well above its TM reflection resonance frequency of 15.8 GHz. The extracted wave and medium parameters are shown in Fig. 2.7.

Referring to the frequency range of interest, (0 – 5) GHz, the extracted parameters reveal the following. The effective wave impedance Z_{eff} shows that the SS MS-WAIM itself is not matched to free space. As will be demonstrated with its integration with the driven array, it acts as a low loss impedance matching facilitator between the array and free space. The composite antenna and SS MS-WAIM system are found to be well matched to free space over a wide bandwidth.

The extracted value of the effective permeability μ_{eff} is equal to one; i.e., the SS MS-WAIM acts as a purely electric surface with no bianisotropic behaviour. The value of ε_{eff} changes by less than 4%, 8.545 – 8.882, over the entire frequency range of interest. These results further illustrate that by working well below the resonances, the lossy regions of the SS MS-WAIM are avoided.

2.2.2.4 Measurements

To verify the simulation results, a 40×40 unit cell SS MS-WAIM was fabricated and measured in an anechoic chamber. The test setup was in both reflection and transmission modes. As shown in Fig. 2.8 (a), the reflection mode included two horn antennas for transmit and receive on the same side of the SS MS-WAIM. An expanded view of the fabricated SS MS-WAIM is also given in Fig. 2.8 (b). The simulated and measured transmission and reflection results for the SS MS-WAIM are shown in Fig. 2.9. It is noted that the measurements were carried out only up to 18.0 GHz again to due to the chamber limitations. Consequently, only the TM reflection resonance at 15.8 GHz could be verified experimentally. The simulated results show very good scanning up to 70° with acceptable transmission and reflection losses for both the TE and TM excitations. Measurements were carried out for broadside and for 30° incidence; those results show good agreement with the simulated results. For the reflection measurements, the simulated and measured results agree very well except below 3.0 GHz. These discrepancies have been determined to be mainly a consequence of the limited functional frequency range of the absorbers available in the anechoic chamber. The transmission measurements on the other hand, agree well with the simulated results across the whole measured band.

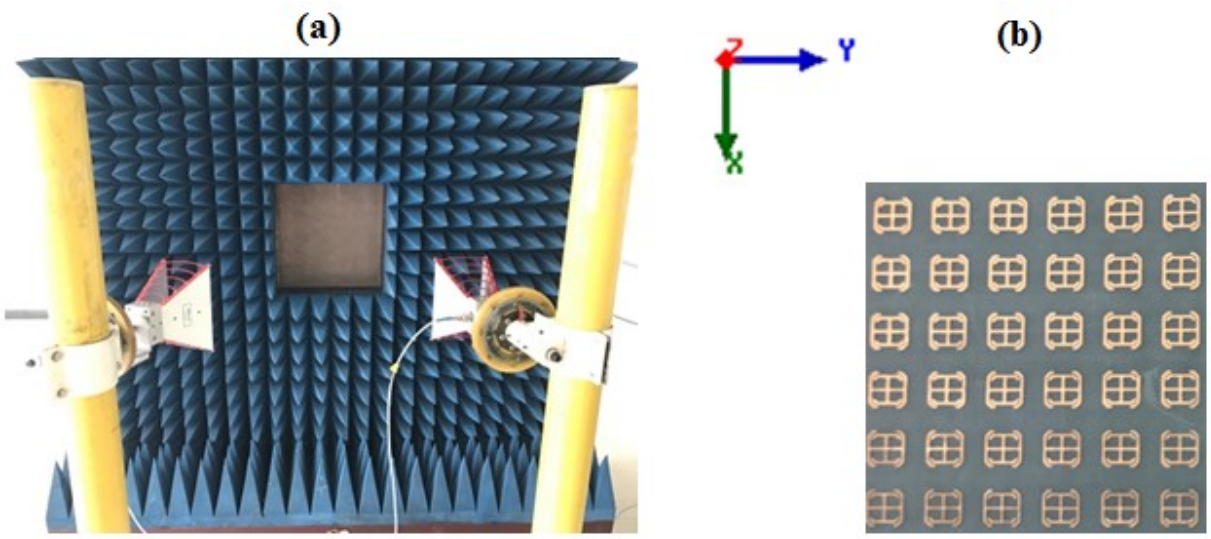

Fig. 2. 8. Measurement setup. **(a)** The reflection measurement and **(b)** an expanded view of the SS MS-WAIM under test.

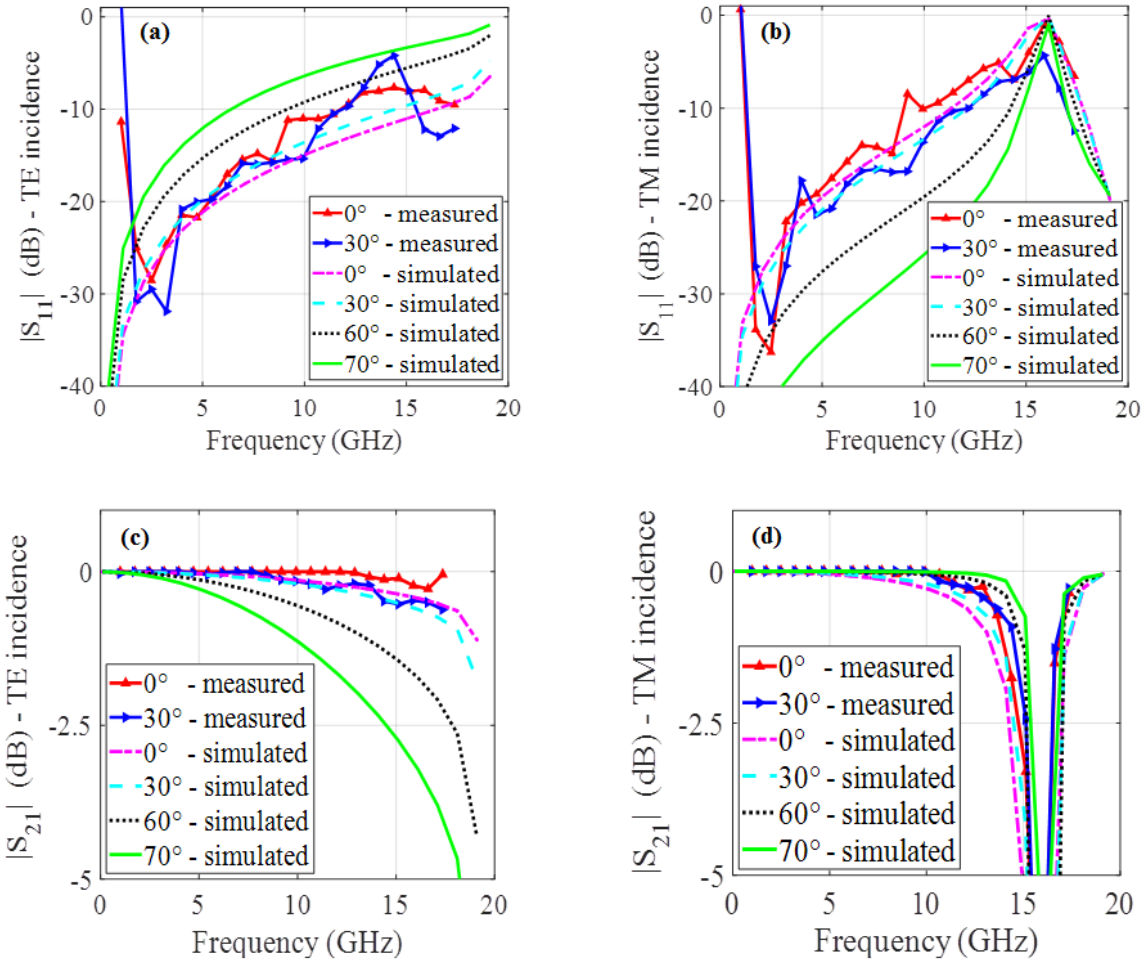

Fig. 2. 9. Simulated and measured transmission and reflection results for the SS MS-WAIM. **(a)** Return loss - TE incidence. **(b)** Return loss - TM incidence. **(c)** Insertion loss - TE incidence. **(d)** Insertion loss - TM incidence.

2.2.2.5 Metasurface integrated with a TCAA

In order to demonstrate the scanning advantages of including a SS MS-WAIM with a driving antenna array, an infinite TCAA was simulated with both an infinite dielectric-WAIM [59, 60] and then with an infinite version of the TC-UAJC based MS-WAIM. The infinite nature of the geometries allowed us to simulate a unit cell of the corresponding finite TCAA-WAIM system. While this choice neglected some minor edge effects, it captures the essence of the performance of the realistic structure given the large extent of the fabricated SS MS-WAIM sample. The TCAA is a wideband array and, hence, was selected to test appropriately the wideband performance of the SS MS-WAIM. To analyze the reference dielectric-WAIM, it was placed directly above the antenna array with the optimized parameters: the relative permittivity $\varepsilon_r = 2.5$ and thickness of dielectric slab $h_{di} = 12.0\ mm$.

Fig. 2.10 (a) shows a side view of one unit cell of the TCAA integrated with the SS MS-WAIM structure. The TCAA is made up of an infinite dipole array with overlapping arms and fed with lumped ports. It is oriented vertically along the *y-z* plane with arms printed on opposite sides of a thin printed circuit board (PCB) substrate. The blue colored arm of the dipole is on the top layer of the substrate and the orange colored arm is on its bottom layer. The purple region, indicated by y_3, represents the amount of overlap with the arms of the adjacent elements. The arms were assumed to be perfect electric conductors (to significantly reduce the computational overhead) mounted on a Rogers RT/Duroid 6010 substrate with a dielectric constant of 10.2 and a thickness of *0.254 mm*. Each element was driven with a lumped port whose active input impedance was $(170 - j38)$ Ω. Fig. 2.10 (b) shows the top view of the SS MS-WAIM which is made up of a 5×5 array of the TC-UAJC elements within the TCAA unit cell. The dimensions of the SS MS-WAIM were adjusted to account for the interactions between it and the antenna. The new optimized dimensions were: $r_1 = 1.59$ *mm*, $g_1 = 0.9774$ *mm*, $g_2 = 0.2384$ *mm*, $L_2 = 4.4568$ *mm*. All other dimensions remained the same.

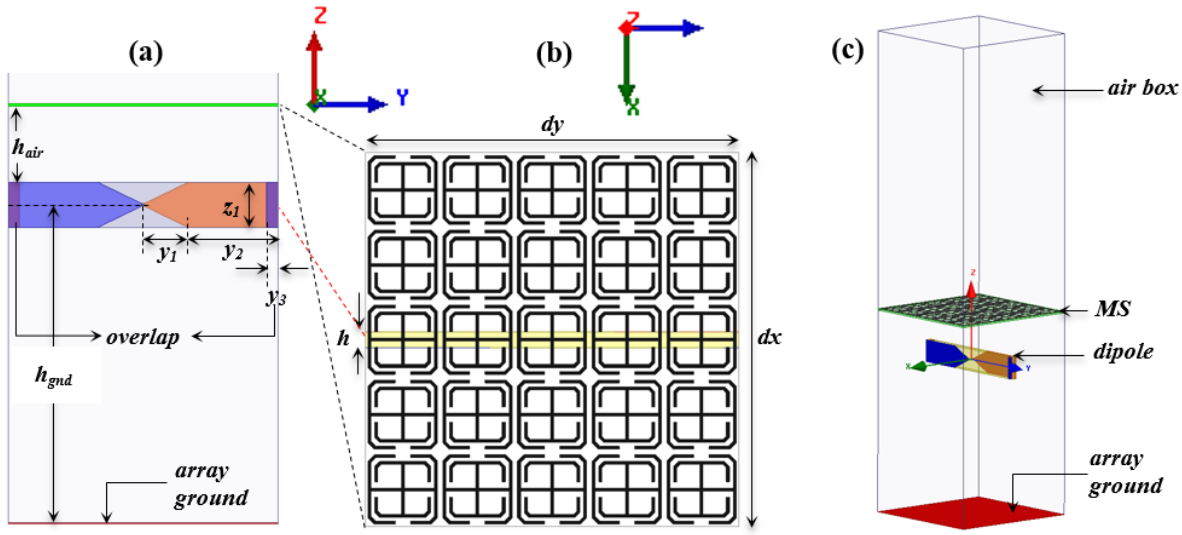

Fig. 2. 10. TCAA integrated with the SS MS-WAIM. **(a)** Side view of a unit cell with horizontally oriented dipole arms printed on opposite sides of the PCB. Blue = top layer, orange = bottom layer, purple = overlap with adjacent elements. **(b)** Expanded top view of the modified SS MS-WAIM within one unit cell. The dimensions of the various parameters of the TCAA-WAIM unit cell are: $z_1 = y_1 = 4.0$ *mm*, $y_2 = 8.0$ *mm*, $y_3 = 1.0$ *mm*, $h_{air} = 6.76$ *mm*, $h_{gnd} = 28.25$ *mm*, $h = 1.016$ *mm*, and $dx = dy = 24.0$ *mm*. **(c)** Perspective view of the unit cell.

The scanning abilities of the SS MS-WAIM and dielectric-WAIM systems are compared in Fig. 2.11 across the E, H, and D (diagonal) planes over a wide bandwidth. The dashed lines represent the dielectric-WAIM results and the solid lines represent the SS MS-WAIM results. At broadside, the simulated performance characteristics of the TCAA integrated with the dielectric- and MS- WAIMs are virtually identical. However, the SS MS-WAIM system has the added advantage of more degrees of freedom with the potential to provide a better impedance match to the assumed *50*-Ω source. Across the E-Plane, both the MS- and dielectric- WAIMs can scan to 60°, however, the SS MS-WAIM can do so with a lower VSWR at wider scan angles. Across the H- and D-Planes, the two systems have very similar performance with the dielectric-WAIM system being slightly better over the lower frequency band while the SS MS-WAIM performs better over the higher frequency band. Nevertheless, both the dielectric- and MS- based WAIM systems scan well out to 70° across their D-planes. Moreover, it can be observed that the SS MS-WAIM system covers a wider bandwidth for all scan angles. The array and SS MS-WAIM combination (*37.264 mm*) is also of a lower profile compared to the dielectric-WAIM and array combination (*42.25mm*).

The transmittance values of the MS- and dielectric- WAIMs for all scan angles across the E, H, and D planes are compared in Fig. 2.12 at 4.0 GHz. It is interesting to find that the SS MS-WAIM outperforms the dielectric-WAIM across both the E and D planes and performs the same as the dielectric-WAIM in the H plane. Previous works on single layer WAIMs based purely on the modification of the free space region above the array aperture are overwhelmingly carried out at a single frequency of operation. Therefore, to make a direct comparison to them, we compare in Table 2.1 the performance of the SS MS-WAIM at 4.0 GHz to those reported in two key works in this area. The work in [59] only presents scanning across the H-plane for two designs. One scans up to 55° and another scans between 40° and 80°. It is shown here that the SS MS-WAIM achieves wider scanning in both the E and H planes in comparison to the results reported in both [59] and [60]. Moreover, it falls only 2° short of the D-plane scan in [60].

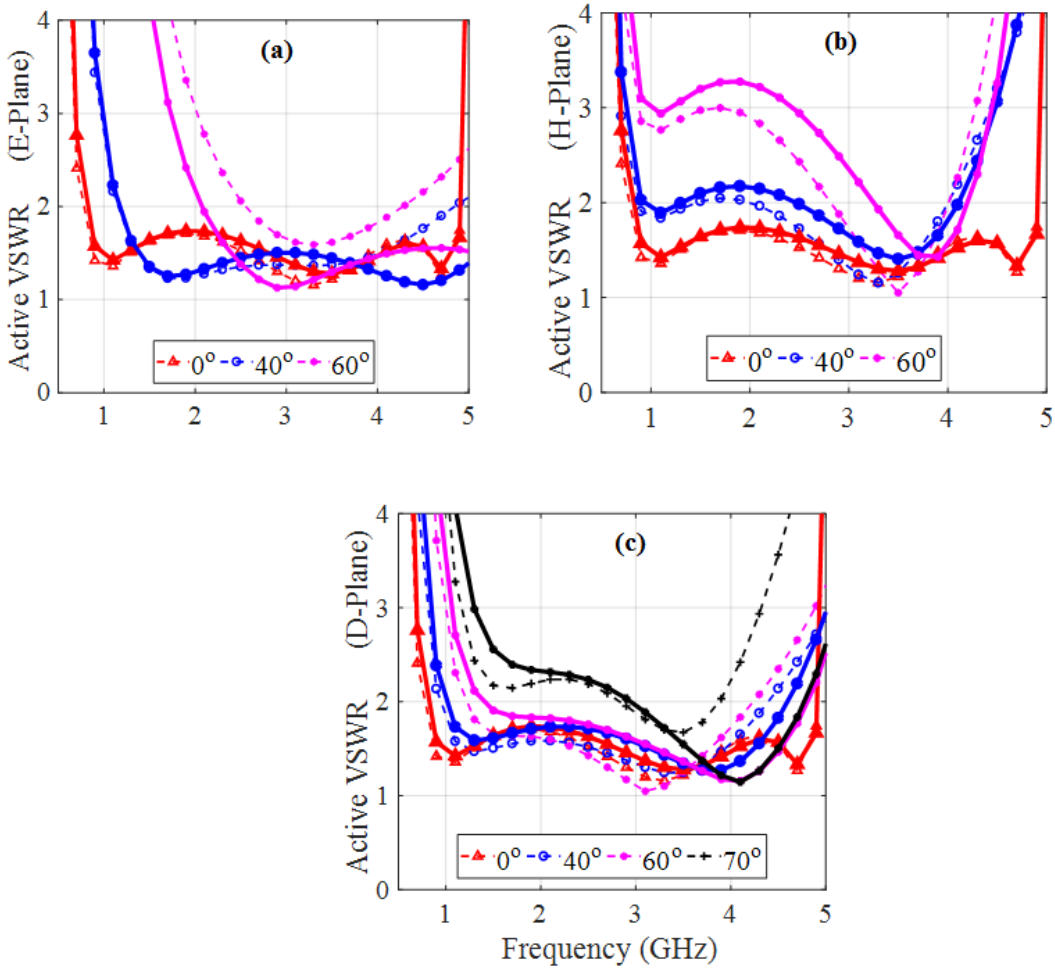

Fig. 2. 11. Scanning of the SS MS-WAIM (solid lines) and dielectric-WAIM (dashed lines) systems. **(a)** E-plane. **(b)** H-plane and **(c)** D-plane.

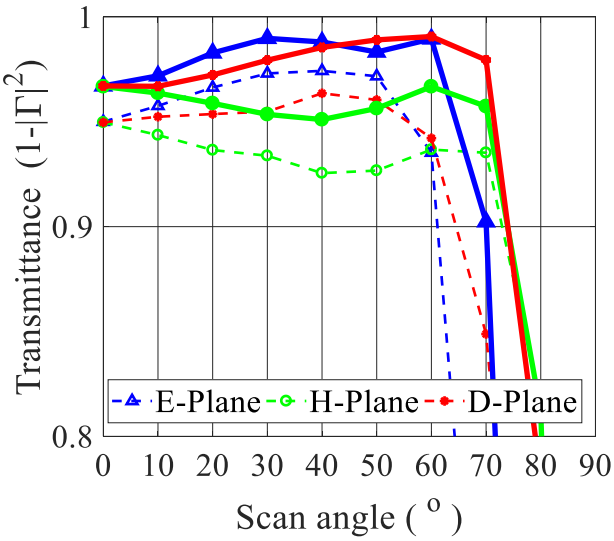

Fig. 2. 12. Comparison of the MS- (solid lines) and dielectric- WAIM (dashed lines) across the E, H, and D planes at a minimum of 80% transmittance (equivalent to VSWR < 3) at 4.0 GHz.

TABLE 2. 1 - Maximum Scan Range at a Single Frequency

	Previous work		*This work*	
	[59]	*[60]*	*Dielectric-WAIM*	*SS MS-WAIM*
E-Plane	*N/A*	45°	64°	72°
H-Plane	*55°*	*65°*	*80°*	*80°*
D-Plane	*N/A*	81°	72°	79°

2.3 Chapter Conclusion

A wideband SS MS-WAIM layer has been systematically designed and its characteristics were experimentally validated. Its effective material parameters were extracted to show the constancy of ε and μ over the desired, very wide operational band of frequencies. The optimized SS MS-WAIM was used as a superstrate over a TCAA of simple printed dipoles to reduce the impedance mismatch of the system to its source when the array is scanning. It was shown that the SS MS-WAIM provides improved scanning along the E and D planes over its wide bandwidth without the use of bulky isotropic dielectrics or multi-layered structures. Furthermore, it maintained the scanning performance in the H plane. An improved doule sided (DS) MS-WAIM and TCAA prototype integrated with a realistic feed network will be reported in Chapter 3.

2

Chapter 3 – Tightly Coupled Antenna Array with a High Figure of Merit

3.1 Chapter Introduction

Following on from Chapter 2 where we presented a novel solution to the wide angle impedance matching (WAIM) problem using a single sided metasurface (SS-MS) superstrate; in this Chapter, we present an improved version of that superstrate using a double sided (DS) metasurface (MS) WAIM layer. The DS MS-WAIM, used to improve the scan performance over a wide bandwidth, is composed of tightly-coupled unequal arm Jerusalem cross (TC-UAJC) elements printed on its two sides. Interestingly, the DS MS-WAIM also improves the cross-polarization levels as the scan angle increases. In addition, we report a new wideband, low-profile feed network, composed of meandered impedance transformer and balun sections. The feed is designed based on Klopfenstein tapered microstrip lines. It can provide more than 6:1 impedance bandwidth while maintaining a high level of current balance. The new superstrate and feed structure represent the key components of a multifunctional tightly coupled antenna array (TCAA) with a very high figure of merit reported herein.

Detailed array analysis and design guidelines are presented for several thicknesses of the DS MS-WAIM. A fully characterized 10 x 10 array prototype is presented that validates the design concepts and simulation methodology employed in this work. The array profile is only $0.088\lambda_L$, where λ_L is the wavelength at the lowest frequency of operation. The optimum array design can scan to 80° along the E-plane and 55° along the H-plane, with an active VSWR ≤ 3.1. The broadside impedance bandwidth is 5.5:1 (0.77 – 4.20) GHz. The improved scan performance was obtained by optimizing the array dimensions for both broadside and at the widest scan angles. An array figure of merit (P_A) [108] was calculated for several TCAA designs, to make comparisons with similar designs in the literature. The figure of merit value of the optimum design, $P_A = 5.49$, is highest reported to date.

This Chapter is organized as follows. Section II gives the theory of operation of TCAAs. Section III is devoted to the tightly coupled antenna array unit cell design that incorporates the feed network and metasurface superstrate. The radiation performance of the computed finite array and manufactured

prototype are presented in Section IV. Sections V gives a set of design guidelines for improved array design. Section VI present the discussion and implications of our results. Finally, in Section VII, our Chapter conclusions are presented.

3.2 Background Theory of TCAAs

Tightly coupled antenna arrays (TCAAs) [7 - 10] are periodically fed wideband arrays, which sample the incoming wave front at less than the Nyquist rate by keeping the element spacing less than $\lambda_H/2$, where λ_H is the wavelength at the highest frequency of operation. At lower frequencies, the array is over sampled resulting in the effective aperture (A_{eff}) remaining roughly constant with frequency. Their operation is based on Wheeler's infinite uniform current sheet (UCS) concept [31, 32], which is an ideal case of a phased array with no reflecting boundary, radiating equally at all frequencies. This concept is equivalent to an infinite number of very small, tightly packed electric or magnetic dipoles, carrying continuous current over an open circuit or short circuit boundary. However, as the dipole lengths approach half a wavelength at the highest frequency, the array performance decrease sharply.

Most practical arrays require a ground plane backing, which causes their input impedance to change drastically, thus limiting their bandwidth. The change in input impedance is manifest such that at low frequencies, the array's radiation resistance tend towards zero (short circuited) and its reactance becomes mostly inductive. The increased array inductance at low frequencies due to the presence of the ground plane, was addressed by Dr Ben Munk [9], through the use of capacitively coupled array elements. The additional coupling capacitance at the tips of the dipoles perform several other functions. It facilitates resonance of the short dipoles given their very low inductance values. It helps to equalize the currents at the feed points of the dipoles to those along the rest of their lengths across a wide frequency range for a constant radiation resistance [31]. In addition, the capacitive loading at the tips of the dipoles make them behave as much longer elements. The controlled mutual coupling introduced by the additional capacitance allows field propagation to neighbouring elements and the elimination of impedance variations to give rise to large bandwidths in low profile implementations.

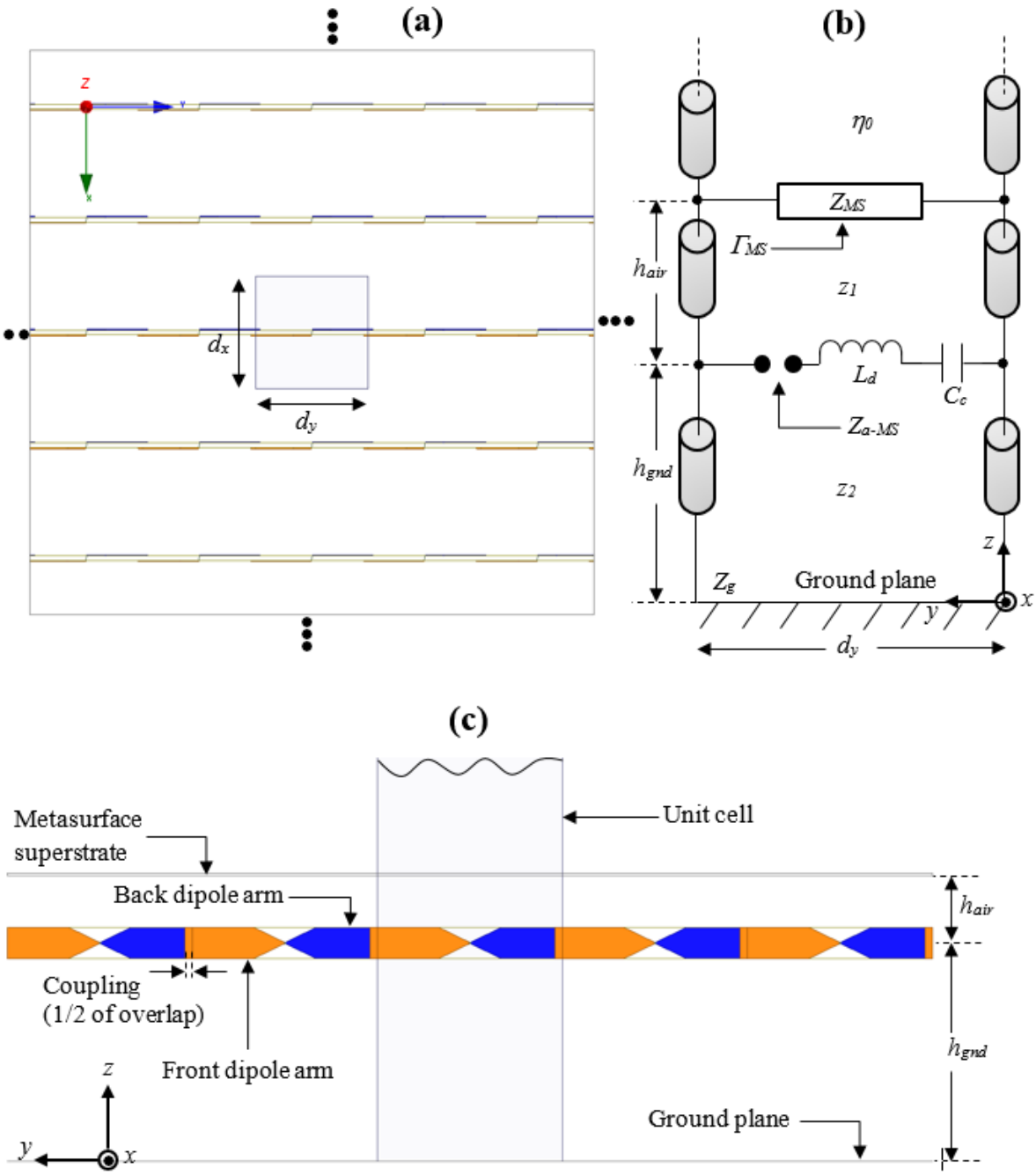

Fig. 3. 1. Tightly Coupled Antenna Array (TCAA). **(a)** Top view of an infinite TCAA above a conducting ground plane. The overlapping arms of adjacent dipoles are printed on opposite sides of a dielectric substrate. A unit cell with dimensions d_x and d_y is shown in the middle of the figure. **(b)** Equivalent circuit of the TCAA [109] with a MS-WAIM superstrate. **(c)** Front view of the infinite TCAA with detailed view of the vertically oriented dipoles, the MS-WAIM superstrate, and the ground plane.

To gain further insight into the working mechanisms of the TCAA, a quasi-analytic approach is employed with the help of an equivalent circuit model together with the extracted scattering parameters of the metasurface. This approach can fairly accurately predict tha active scan impedance of the array and hence its active reflection coefficient and active voltage standing wave ratio.

The top and side views of an infinite TCAA above a PEC ground plane is shown in Figs. 3.1 (a) and 3.1 (c) respectively. The equivalent circuit [109] of a single-polarized version of this array is shown in Fig. 3.1 (b). In this equivalent circuit model, the dipole is represented by an inductance, L_d, and a coupling capacitace with neighbouring elements, C_c. The intervening layers between the ground plane, the dipole array, and the MS-WAM are represented by transmission line sections which may or may not be free space. For a well sampled array where only the fundamental TE and TM Floquet modes are propagating, the admittances in each layer [110] are given by,

$$Y_{00}^{TE} = \frac{k_{z00}}{\omega\mu_0\mu_r} \tag{3.1}$$

$$Y_{00}^{TM} = \frac{\omega\varepsilon_0\varepsilon_r}{k_{z00}} \tag{3.2}$$

Where k_{z00} is the propagation constant in the z direction for each layer and is defines as:

$k_{z00} = k_0\sqrt{\mu_r\varepsilon_r}\cos(Sin^{-1}(\frac{sin\theta}{\sqrt{\mu_r\varepsilon_r}}))$, ($k_0$ is the free space wavenumber, μ_r is the relative or effective permeability of a given layer, ε_r is the relative or effective permittivity of a given layer, ω is the angular frequency, and θ is the scan angle).

The impedances of each layer when scanning along the E-plane (ϕ = 90°, TM polarized, along *y-z* direction) and H-plane (ϕ = 0°, TE polarized, along *x-z* direction) are given by [31],

$$Z_r^E = \frac{d_y}{d_x}\frac{1}{Y_{00}^{TM}} = \eta_0\sqrt{\frac{\mu_r}{\varepsilon_r}}\frac{d_y}{d_x}\cos\left(Sin^{-1}\left(\frac{sin\theta}{\sqrt{\mu_r\varepsilon_r}}\right)\right) \tag{3.3}$$

$$Z_r^H = \frac{d_y}{d_x}\frac{1}{Y_{00}^{TE}} = \eta_0\sqrt{\frac{\mu_r}{\varepsilon_r}}\frac{d_y}{d_x}\frac{1}{\cos(Sin^{-1}(\frac{sin\theta}{\sqrt{\mu_r\varepsilon_r}}))} \tag{3.4}$$

where η_0 *is* the intrinsic impedance of free space, d_x and d_y are the unit cell dimensions along the *x*- and *y*-axis. In the case of the MS-WAIM, the effective parameters values extracted as was described in Chapter 2 will have to be used in place of the relative ones.

The active or scan impedance of the infinite periodic TCAA backed by a PEC ground plane, Z_a, is the input impedance of each antenna element in the array, when all other elements are similarly excited [111]. Z_a is given by,

$$Z_a = \frac{2\eta_0}{\pi^2}\frac{a^2}{d_x d_x}\sum_{m=-\infty}^{\infty}\sum_{n=-\infty}^{\infty} F_m^2 G_n^2 H_{mn}(1 - e^{-2jk_{mn}h_{gnd}}) \tag{3.5}$$

where

$$F_m = \frac{2\sin(\frac{k_{xm}b}{2})}{k_{xm}b} \tag{3.6}$$

$$G_n = \frac{\cos(\frac{k_{yn}a}{2})}{1 - (\frac{k_{yn}a}{\pi})^2} \tag{3.7}$$

$$H_{mn} = \frac{1 - (\frac{k_{yn}}{k_0})^2}{k_{mn}/k_0} \tag{3.8}$$

and

$$k_{xm} = k_{x0} + \frac{\lambda m}{d_x} = k_0 sin\theta sin\varphi + \frac{k_0 \lambda m}{d_x} \tag{3.9}$$

$$k_{yn} = k_{y0} + \frac{\lambda n}{d_y} = k_0 sin\theta cos\varphi + \frac{k_0 \lambda n}{d_y} \tag{3.10}$$

$$k_{mn} = k_0\sqrt{1 - \left(\frac{k_{xm}}{k_0}\right)^2 - \left(\frac{k_{yn}}{k_0}\right)^2} \tag{3.11}$$

a = length of the dipole, *b* = width of the dipole, λ is the free space wavelength, k_0 is the free space wave number, and k_{x0}, k_{y0}, k_{z0}, are the propagation constants in the ***x***, ***y***, and ***z*** directions.

When considering higher order TE and TM Floquet modes (*mn*), the active impedance seen from the dipole layer looking into the free-space impedance (η_0) shunted MS superstrate can be written as follows [60, 111],

$$Z_{a-MS} = \frac{2\eta_0}{\pi^2}\frac{a^2}{d_x d_x}\sum_{m=-\infty}^{\infty}\sum_{n=-\infty}^{\infty} F_m^2 G_n^2 \left(H_{mn}^{TE}\frac{\eta_{mn}^{TE}}{k_0}\gamma_{mn}^{TE} + H_{mn}^{TM}\frac{\eta_{mn}^{TM}}{k_0}\gamma_{mn}^{TM}\right) \quad (3.12)$$

where

$$\eta_{mn}^{TE} = \frac{k_0^2}{k_{mn}} \quad (3.13)$$

$$\eta_{mn}^{TM} = k_{mn} \quad (3.14)$$

$$\gamma_{mn}^{TE/TM} = \left(1 + \Gamma_{MS,mn}^{TE/TM} e^{-2jk_{mn}h_{air}}\right) \times \frac{1 + \Gamma_g e^{-2jk_{mn}h_{gnd}}}{1 - \Gamma_{MS,mn}^{TE/TM}\Gamma_g e^{-2jk_{mn}(h_{gnd}+h_{air})}} \quad (3.15)$$

and Γ_g is the reflection coefficient of the ground plane (= -1), $\eta_{mn}^{TE/TM}$ are the TE and TM Floquet impedances, and $\gamma_{mn}^{TE/TM}$ are compensation terms due to reflections from nearby interfaces.

The effective impedance of the MS, Z_{MS}, can be extracted from its S-parameters via full wave simulations as was described in Chapter 2. A number of higher order Floquet modes should be included in the effective impedance extraction process in order to obtain accurate results. This would account for the additional modes excited on the MS when it is inserted into the antenna array unit cell. These additional modes are due to the MSs near field interactions with the antenna array. Having obtained the effective impedance and the reflection coefficient of the MS, the active impedance of the array, $Z_{a\text{-}MS}$, can be obtained from (3.12). Alternatively, and more accurately, $Z_{a\text{-}MS}$ can be obtained via full wave simulations from which can be derived the active reflection coefficient and the active voltage standing wave ratios (VSWR), as detailed in the following sections.

3.3 Tightly Coupled Antenna Array Design

In this section, the design for the constituent parts of the TCAA shown in Fig. 3.2 will be discussed. A unit cell design of an overlapped dipole antenna in an infinite array setting with a 170 Ω lumped port feed is first presented. This is followed by the design of a double sided MS-WAIM and the extraction of its constituent parameters. Next, the design of a realistic wideband balun to feed the array is presented. Finally, following the introduction of a balun in the array, methods are devised to suppress the CM currents that arise, to improve the range of scanning angles in the elevation plane, and to reduce the levels of cross-polarization for the designs presented.

3.3.1 Lumped Port Fed Unit Cell Design

An expanded view of the lumped port fed dipole is shown in Fig. 3.2 (b). In the preliminary simulations, the TCAA unit cell contained an overlapped dipole antenna fed with a 170 Ω lumped port impedance placed at a distance of $h_{gnd} = 28.2473\ mm$ above a PEC ground plane. The dipole is oriented vertically along the *y-z* plane with its arms printed on opposite sides of a RT/Duroid™ 6010 substrate with a

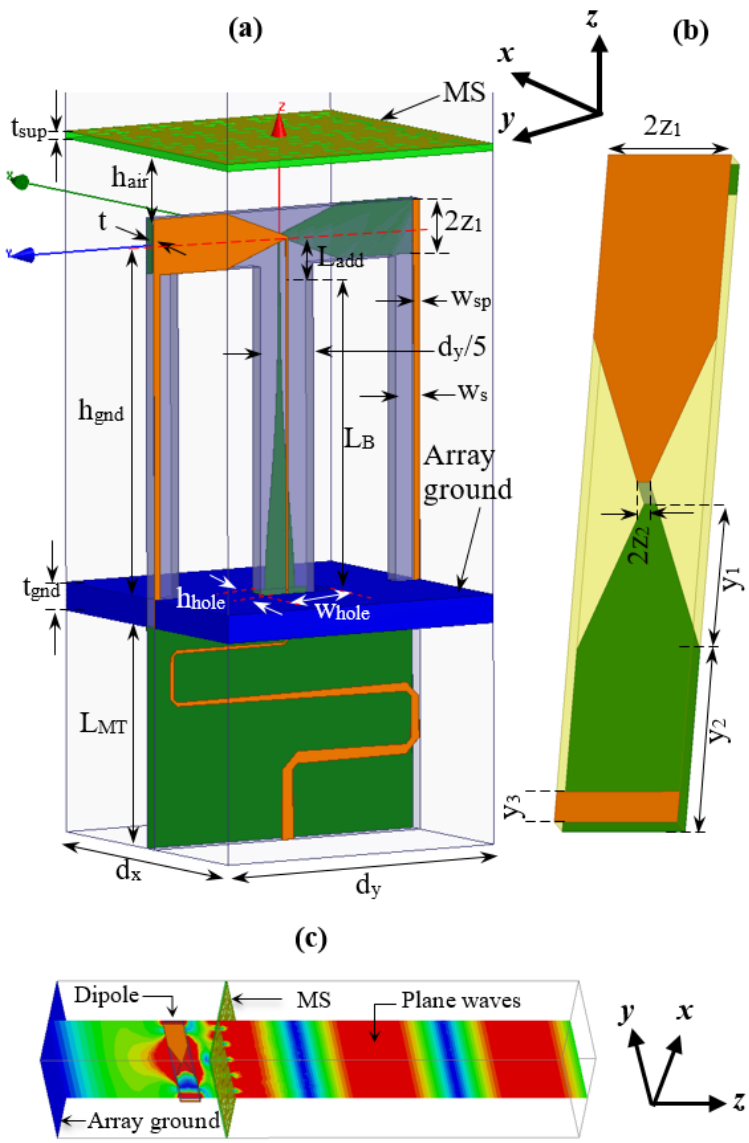

Fig. 3. 2. TCAA unit cell. **(a)** Perspective view of the balun fed TCAA unit cell with a DS MS-WAIM superstrate, shorting pins and a perforated feed substrate. The feed and dipole were designed on a Rogers RT/Duroid™ 6010 substrate with a thickness, $t = 1.016\ mm$ and relative dielectric constant, $\varepsilon_r = 10.2$. **(b)** Expanded view of the lumped port fed dipole. **(c)** Electric fields along the *y-z* plane for the lumped port fed unit cell.

thickness, $t = 1.016\ mm$ and relative dielectric constant, $\varepsilon_r = 10.2$. The period of the unit cell is $d_x = d_y = 24\ mm$. The infinite array is created using Floquet mode analysis plus master-slave periodic boundary conditions along the x and y directions. To achieve a wideband impedance match for the dipole array, the feed flared section, y_1 *(= 4 mm)*, the length of the dipole arms, y_2 *(= 8 mm)*, the capacitive coupling between adjacent elements, y_3 *(= 1 mm)*, the arm widths, $2z_1$ *(= 4 mm)*, and the width of the lumped port, $2z_2$ *(= 0.12 mm)* were all tuned. The dipole antenna is covered with a 5 x 5 array of the DS MS-WAIM at a height of $h_{air} = 6.761\ mm$. The overall height of the array from the ground plane to the top of the MS is *37.2623 mm*.

The impedance bandwidth of the lumped port fed infinite dipole array at broadside for VSWR ≤ 2 is 6.23:1 (0.79 GHz – 4.92 GHz), which will be discussed in the next sub-section.

3.3.2 Double Sided MS-WAIM Design

The proposed double sided metasurface (DS-MS) unit cell is depicted in Fig. 3.3. It is composed of tightly-coupled unequal arm Jerusalem cross (TC-UAJC) elements printed on the two sides of a Rogers 5880 substrate. The bottom element is rotated 90° relative to the element at the top to ensure uniform performance when excited along the ± z directions. Due to the symmetrical nature of the DS MS-WAIM, it will give a more consistent performance when scanning along the various planes. The effective medium parameters of the DS MS-WAIM were extracted from its reflected and transmitted signals using the method described in [104]. These extracted parameters are shown in Fig. 3.4. It is seen that μ_{eff} is zero and ε_{eff} has a constant value of 8.6 within the frequency range of interest (0 to 5.0 GHz). A mu zero material has a zero index of refraction. According to Snell's law, the angle of refraction from this type of material is zero degrees irrespective of the angle of incidence within the material. As a result, the DS-MS is able to transform the cylindrical waves from the array into plane waves with minimal phase variation to enable wide angle scanning. This waveform transformation can also help to lower the array profile since all the energy is concentrated in the forward direction. This phenomenon is demonstrated in Fig. 3.2 (c).

The DS MS-WAIM also introduce a capacitive reactance to counteract the effects of the array's inductively reactive ground plane thereby minimizing the variation of the array's active reflection coefficients at wider scan angles. The solid red curve in Fig. 3.5. Shows the effectiveness of the DS MS-WAIM as a wideband (6.23:1) impedance matching layer. Without the DS MS-WAIM, the array is highly unmatched across most of the band as indicated by the dotted blue curve.

When the MS structure is integrated with the TCAA, its dimensions were adjusted to compensate for the near field interactions. The final optimized MS dimensions were: $r_1 = 1.59$ *mm*, $g_1 = 0.9774$ *mm*, $g_2 = 0.2384$ *mm*, and $L_2 = 4.4568$ *mm* with the other dimensions as shown under Fig. 3.3.

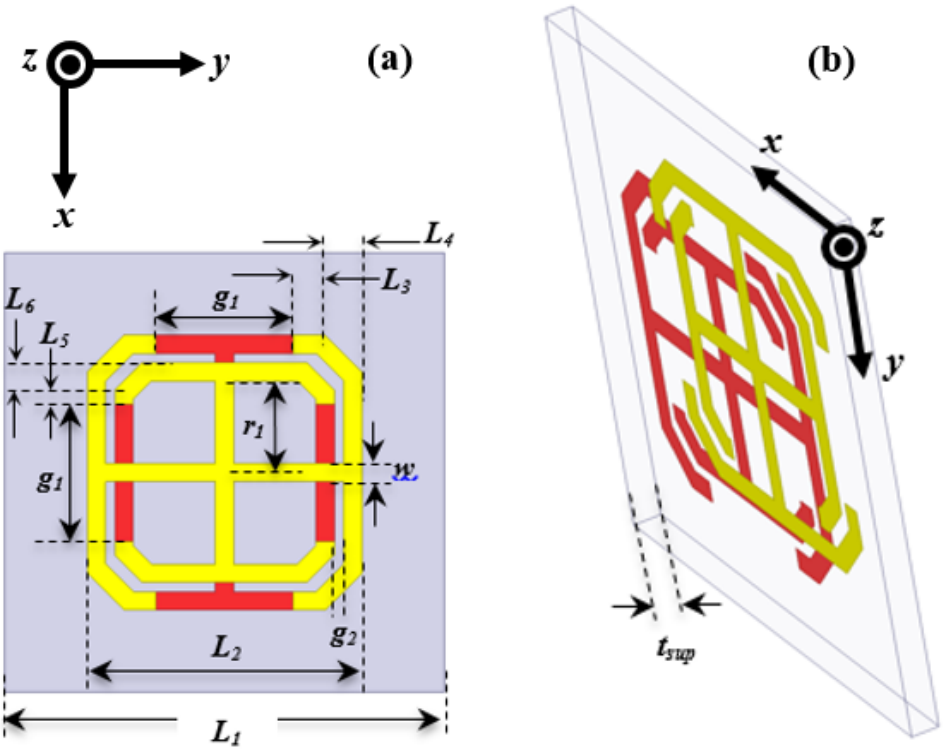

Fig. 3. 3. DS-MS unit cell geometry. **(a)** Top view. **(b)** Perspective view. The DS-MS unit cell dimensions in millimeters are: $w = 0.2$, $t_{sup} = 0.254$, $g_1 = 1.5$, $g_2 = 0.1$, $L_1 = 4.8$, $L_2 = 3.0$, $L_3 = 0.35$, $L_4 = 0.4$, $L_5 = 0.15$, $L_6 = 0.3$, and $r_1 = 1.0$. The substrate is Rogers RT/Duroid™ 5880 with $\varepsilon_r = 2.2$ and $\tan\delta = 0.0009$. The direction of propagation of the exciting wave is along the z-axis.

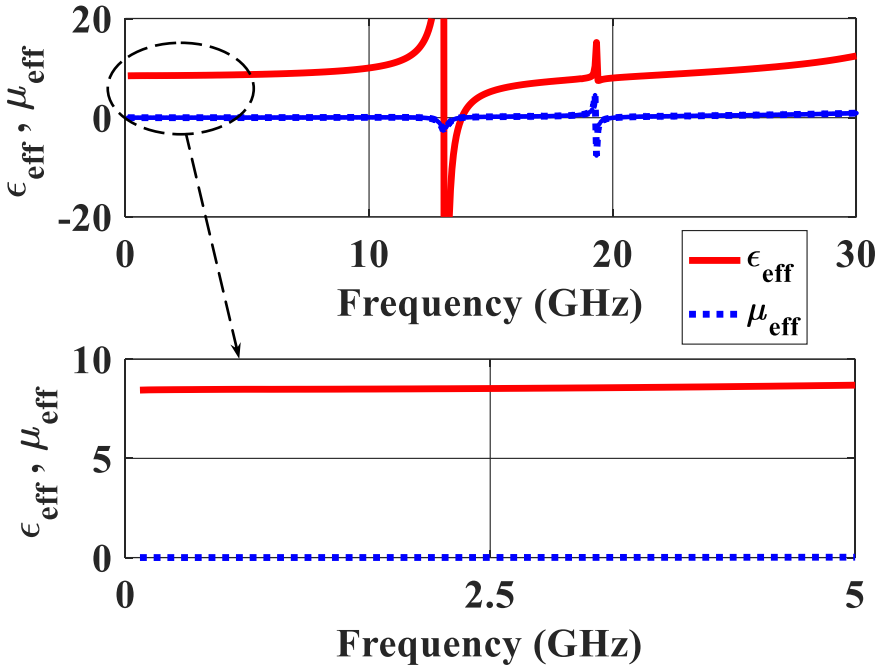

Fig. 3. 4. The extracted ε_{eff} and μ_{eff} for the DS-MS.

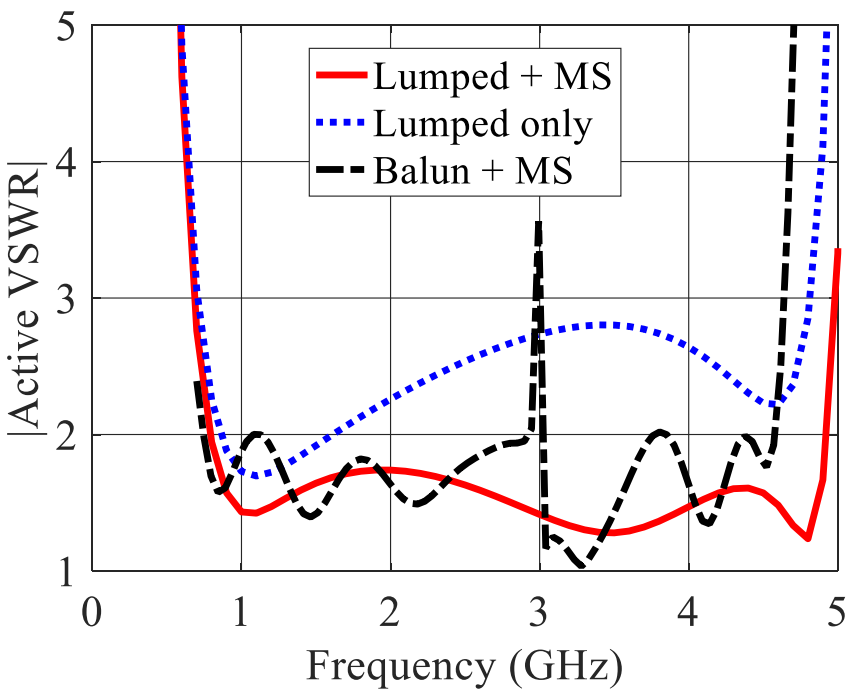

Fig. 3. 5. Active VSWR of the infinite dipole array at broadside. The solid-red curve represents the lumped port fed array with the DS MS-WAIM superstrate. A 6.23:1 impedance bandwidth (0.79 GHz – 4.92 GHz) is obtained (solid-red curve). The dotted-blue curve represents the lumped port fed array with no superstrate. The dashed-black curve represents the balun fed array with the DS MS-WAIM superstrate but without any shorting pins.

3.3.3 Balun Design

To cover the inherent wide bandwidth of the TCAA, an equally wideband feed network is required. The proposed feed network consists of an impedance transformer and a balun (B), both of which were constructed from Klopfenstein [112] tapered microstrip lines. The characteristic impedance variation with distance along the taper is given as:

$$\ln Z(z) = \frac{1}{2}\ln(Z_0 Z_L) + \frac{\Gamma_0}{\cosh A} A^2 \phi\left(\frac{2z}{L} - 1, A\right) \quad for\ 0 \leq z \leq L \tag{3.16}$$

Where:

$$\phi(x, A) = -\phi(-x, A) = \int_0^x \frac{I_1(A\sqrt{1-y^2})}{A\sqrt{1-y^2}} dy \quad for\ |x| \leq 1$$

and $I_1(x)$ is the modified Bessel function. The resulting reflection coefficient of the taper is given as:

$$\Gamma(\theta) = \Gamma_0 e^{-j\beta L} \frac{cos\sqrt{(\beta L)^2 - A^2}}{\cosh A} for\ \beta L \geq A \tag{3.17}$$

and

$$\Gamma(\theta) = \Gamma_0 e^{-j\beta L} \frac{cos\sqrt{A^2 - (\beta L)^2}}{\cosh A} for\ \beta L < A \tag{3.18}$$

In equations (3.16) - (3.18), Γ_0 is the reflection coefficient at zero frequency and it is given as:

$$\Gamma_0 = \frac{Z_L - Z_0}{Z_L + Z_0} \simeq \frac{1}{2}\ln(\frac{Z_L}{Z_0})$$

From (3.17), the maximum ripple in the passband ($\beta L \geq A$) is given as:

$$\Gamma_m = \frac{\Gamma_0}{\cosh A} \tag{3.19}$$

The minimum length of taper for a given Γ_m in the passband can be calculated from equation (3.19). Equations (3.16) – (3.14) were evaluated using MATLAB [103] to obtain the impedance and reflection coefficient variation with distance along the taper. The closed form synthesis equations given in [113]

were then used to calculate the physical dimensions of the taper width for all the impedance values, given the dielectric constant and substrate height. The resulting dimensions were then imported into the commercially available software, ANSYS High Frequency Structure Simulator, ANSYS-HFSS [102], to model and optimize the design. The feed network was designed on the same RT/Duroid™ 6010 substrate as the TCAA and for a lower cut off frequency of 0.5 GHz. The high dielectric constant value of the substrate is necessary to realise a compact and simple design. The high dielectric constant reduces the height of the balun so that it can fit within the small space available between the low profile antenna array and its ground plane.

The straight impedance transformer (ST) was designed for an input impedance of 50 Ω on one end and an impedance of 92.4 Ω on the output. The latter corresponds to a line width of 0.16 mm on the microstrip lines, which in turn gives an impedance of 150 Ω on the parallel strip lines.

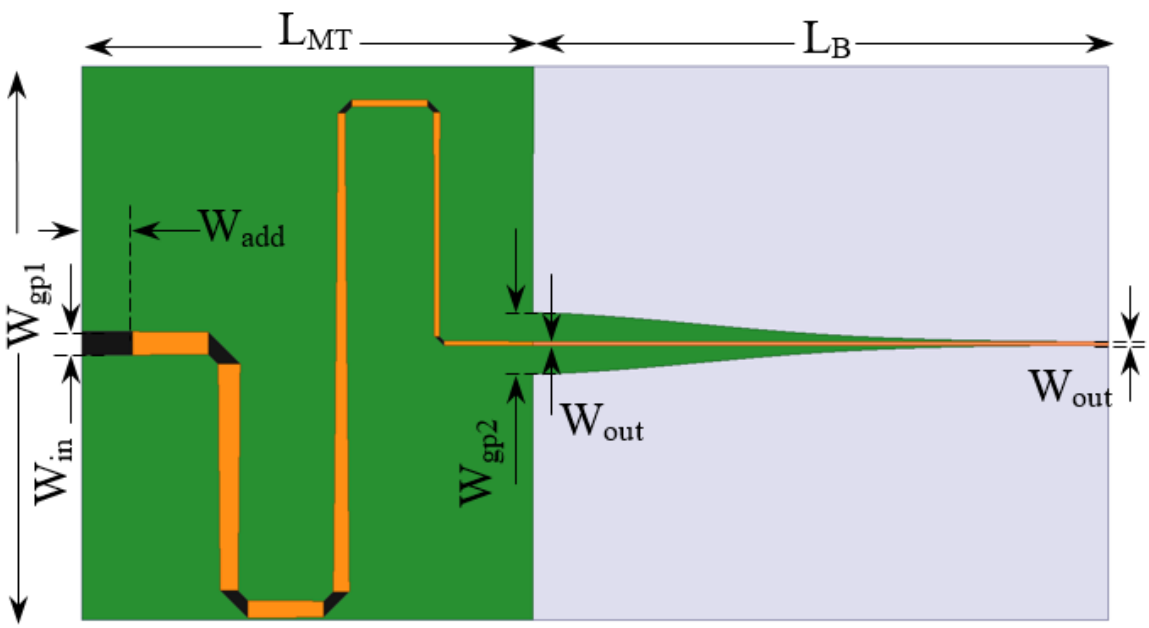

Fig. 3. 6. Top view of the meandered impedance transformer (MT) and balun (B). The optimized balun dimensions are: W_{in} = *0.9279 mm,* W_{out} = *0.16 mm* $W_{gp1} = d_y$ = *22.0 mm,* W_{gp2} = *2.1048 mm,* W_{add} = *2.0 mm,* L_{MT} = *15.8417 mm,* and L_B = *25.2413 mm.*

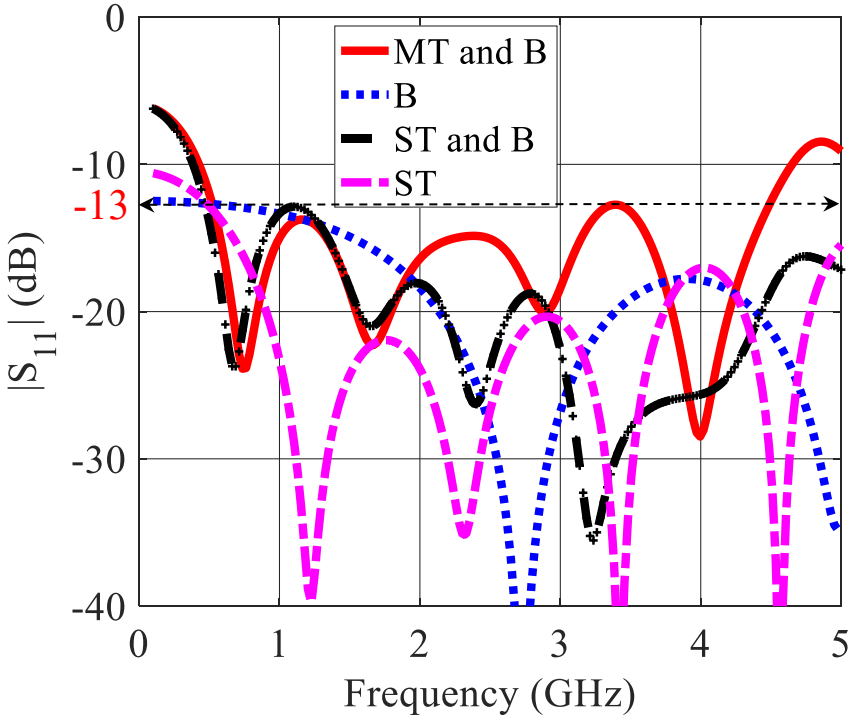

Fig. 3. 7. Magnitude of the reflection coefficient of the meandered transformer and balun (MT and B), balun (B), straight transformer and balun (ST and B), and straight transformer (ST).

The lower 150 Ω impedance was chosen instead of an initial lumped port impedance of 170 Ω since the corresponding line width would be too narrow to be manufactured accurately. The length of this transformer, L_{ST}, was found to be *50.5368 mm*. To reduce the profile of the array, the transformer was meandered using the optimum miter formulation [114]. During this design, it was discovered that using the optimum mitre bends, resulted in extremely thin bends. To overcome this problem, both the inner and outer corners of the bends were mitered by equal amounts which gave rise to bends with more surface area. These mitered bends are shown as solid black in Fig. 3.6. Also shown in Fig. 3.6 is an additional solid black rectangular pad of length $W_{add} = 2\ mm$ at the commencement of the trace. This pad was added to act as a connection point of the SMA connector, which was included in the simulation to produce realistic results. The meandered version of the ST is indicated by the L_{MT} section in Fig. 3.6. To produce a balanced feed for the TCAA, the ground plane at the 92.4 Ω port of the unbalanced transformer was gradually tapered to a balanced parallel strip of equal width with the top trace. The width of the top trace of the balun, W_{out}, remained uniform along its length. The balun section of the

feed structure is indicated by L_B in Fig. 3.6. The full and tapered sections of the ground plane are shown in green in Fig. 3.6.

The simulated magnitude of the reflection coefficient of the meandered transformer and balun (MT and B), balun (B), straight transformer and balun (ST and B), and straight transformer (ST) are shown in Fig. 3.7. The reflection coefficient for all four cases are < -13 dB from 0.5 GHz to 4.5 GHz. We can see that in the "MT and B" cases, the high frequency performance deteriorates compared to the "ST and B" cases. This is due to increased reflections at the bends. Nevertheless, the "MT and B" performance is < -13 dB within the frequency range of interest.

To find out the current balance on the feed structure, the ratio of the surface currents along a line for the top and bottom conductors was computed using HFSS. It can be seen from Fig. 3.8 that the currents on the last (5 – 10) mm sections of the B, MT and B, ST and B are practically identical indicating a high level of current balance within those sections.

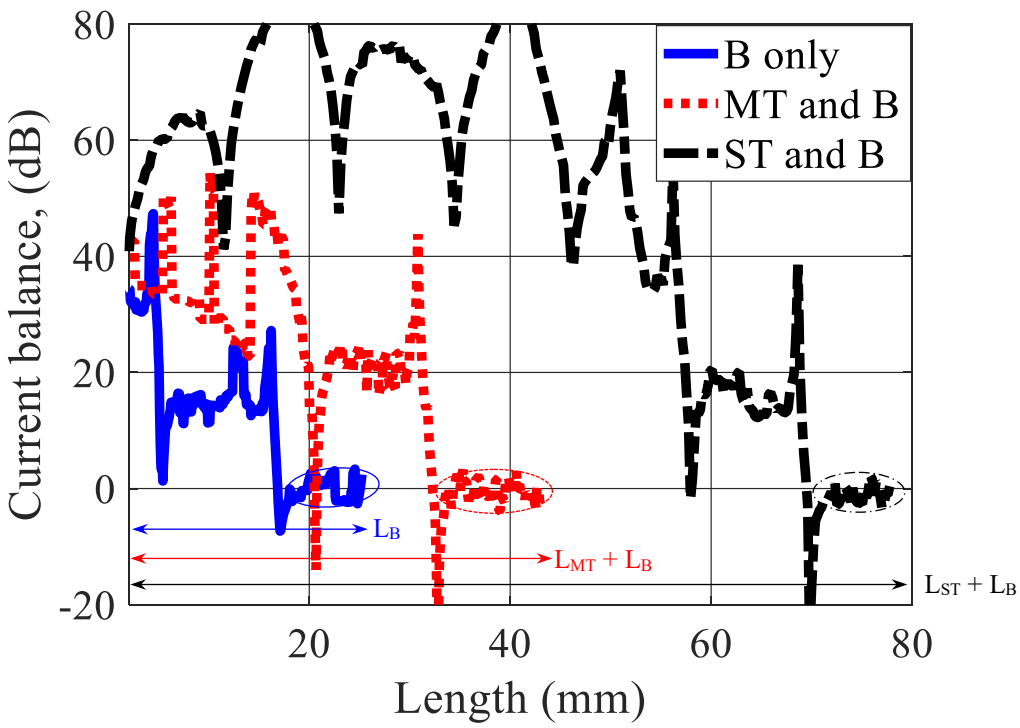

Fig. 3. 8. Magnitude of the line current balance along the axis of the balun (B), meandered transformer and balun (MT and B), and straight transformer and balun (ST and B). The portions of the traces within the ovals is where the line currents on the top and bottom conductors are practically identical.

These portions of the traces are enclosed within the solid-blue, dotted-red, and dashed-black ovals respectively.

3.3.4 Balun Fed Unit Cell Design

A detailed view within the TCAA unit cell incorporating a meandered wideband balun is shown in Fig. 3.2 (a). The E-plane is along the *y-z* direction and the H-plane is along the *x-z* direction.

Following the successful design of the MS, the lumped port fed antenna array, and the wideband balun, the next step was to integrate all the parts and perform an overall optimization. Several adjustments were made to bring the whole antenna inside the unit cell into balance. A variable length of transmission line, L_{add}, of equal width was added to the tips of the top and bottom conductors of the balun. This additional length of line was used to equalize the antenna input impedance to the characteristic impedance of the balun.

3.3.4.1 Common mode suppression

Although the stand-alone balun was well matched, when placed in the array setting, the strong mutualcoupling between adjacent units causes the feed to be unbalanced. These unbalanced currents led to an induced common-mode resonance around mid-band (see dashed curve in Fig. 3.5) as was reported in [52] and a reduction in the achievable bandwidth. To eliminate these CM currents, the first step was to reduce the array unit cell size by reducing y_1 from *6 mm* to *5 mm*. The inner radius of the MS unit cell, r_1, was also reduced from *1.59 mm* to *1.4 mm* to fit into the new array unit cell. In the consequent step, a shorting pin to ground was also introduced on the excited arm of the dipole. Finally, cuts were made on the thin substrate on either side of the balun to reduce the amount of coupling and the possibility of surface waves.

With the addition of the shorting pins, the CM resonance moved higher up in frequency but not entirely out of band. A parametric study was carried out on L_{add}, and the dipole overlap, y_3. The result of this study is displayed in Fig 8. In Fig. 3.9 (a), when L_{add} is reduced from *4.0 mm* to *0 mm* ($y_3 = 1.0\ mm$), the CM resonance is moved almost entirely out of band, but the low frequency behavior of the array deteriorates.

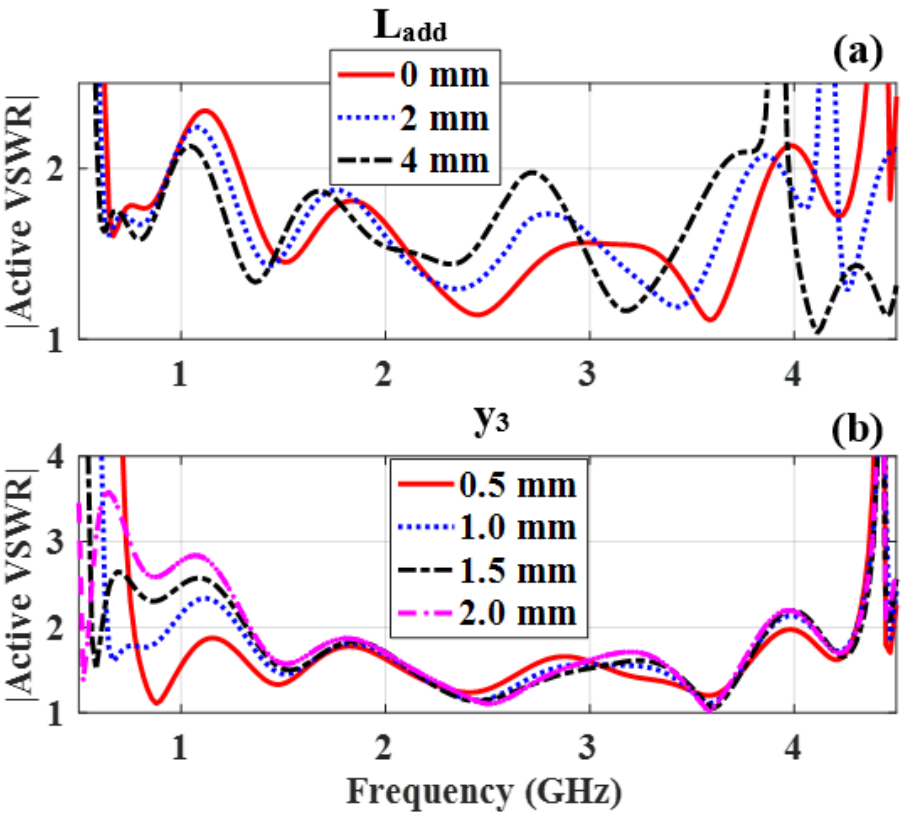

Fig. 3. 9. Parametric study on the CM resolution process for the infinite array. **(a)** The additional length of transmission line, L_{add}. **(b)** The dipole overlap, y_3. A 5.58:1 broadside impedance bandwidth (0.77 GHz – 4.3 GHz) was obtained.

The shorting pin creates a resonance loop with the driven arm of the dipole and the array ground plane. By reducing the value of L_{add}, the CM resonance is shifted to higher values and eventually out of band. This method has the added benefit of reducing the array height by *4 mm* whilst ensuring a CM-resonance free array. To improve the low frequency behavior of the array, the optimum value of $L_{add} = 0\ mm$ found from the previous step was utilized. The value of y_3 was then varied from *0.5 mm* to *2.0 mm* and the result is displayed in Fig. 3.9 (b). For $y_3 = 0.5\ mm$, the low frequency behavior was restored, and the infinite array was matched over a slightly reduced impedance bandwidth of 5.58:1 (0.77 GHz – 4.3 GHz) compared to the lumped port fed design.

3.3.4.2 Common mode resonance free design

In the previous case, L_{add} was decreased to *0 mm* to match the array and reduce the array profile in the process. To further reduce the array profile and to provide more flexibility in matching the array over wider scan angles, the balun was redesigned as was described earlier but with a reduced height of

22.7145 mm. The impedance transformer section remained unaltered. This balun is henceforth referred to as the shorter balun (SB) throughout this Thesis. The rest of the antenna dimensions are given in Table 3.1. With L_{add} = *2 mm* and h_{air} = *5mm*, scans of up to 70° along the E-plane and 55° along the H-plane were obtained over a maximum VSWR value of 3.15 as shown in Fig. 3.10 (a). The broadside impedance bandwidth is 5.5:1. The co- and cross-polarization discrimination is > 20 dB across the whole band as can be seen in Fig. 3.10 (b). In this work, Ludwig's third definition of cross-polarization [115] is utilized.

When scanning to wider angles, we need to find the effect on the cross-polarization levels. In Fig. 3.11 (a), we see that the E- plane cross-polarization levels around f_{mid} and f_H improves as the scan angle increases. Around f_L, the increase in the cross-polarization levels while scanning from broadside to 70° is only 3 dB. The parameters f_L, f_{mid}, and f_H refers to the low frequency, mid frequency, and high frequency regions of the band respectively.

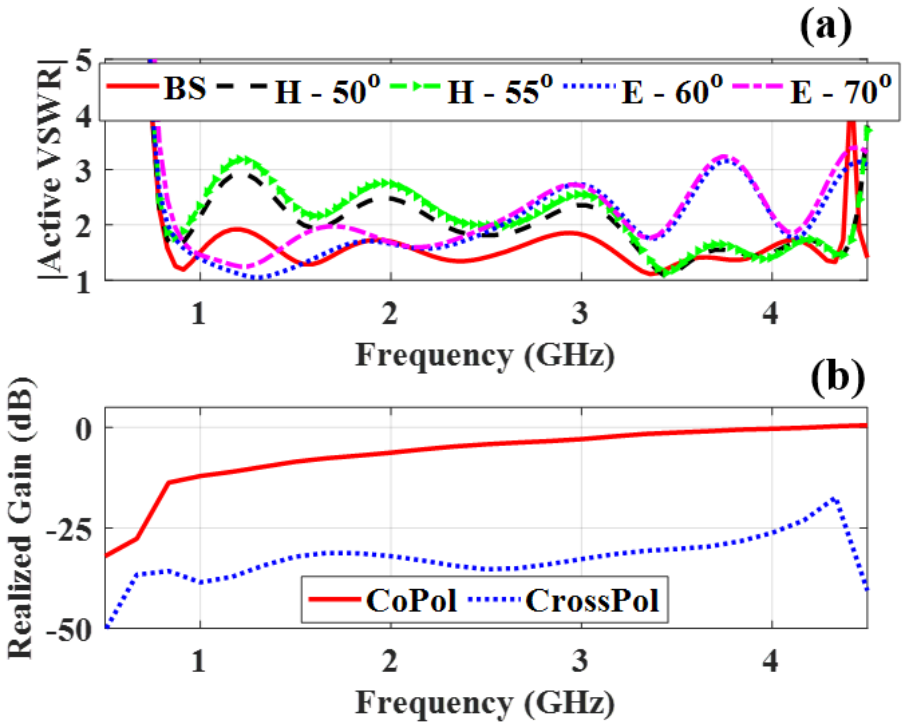

Fig. 3. 10. The infinite array performance using the DS-MS (0.254 mm thick) superstrate and the shorter balun feed. **(a)** Scanning ability. **(b)** Co- and cross-polarized realized gains.

(a)

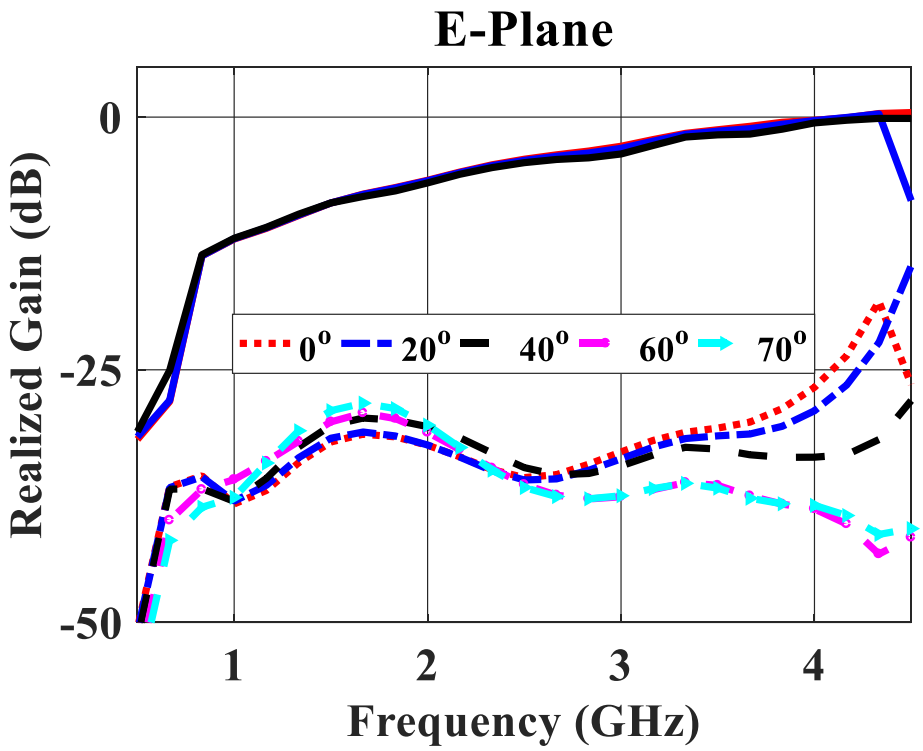
E-Plane
0
-25
-50
Realized Gain (dB)
1
2
3
4
Frequency (GHz)
0°
20°
40°
60°
70°

(b)

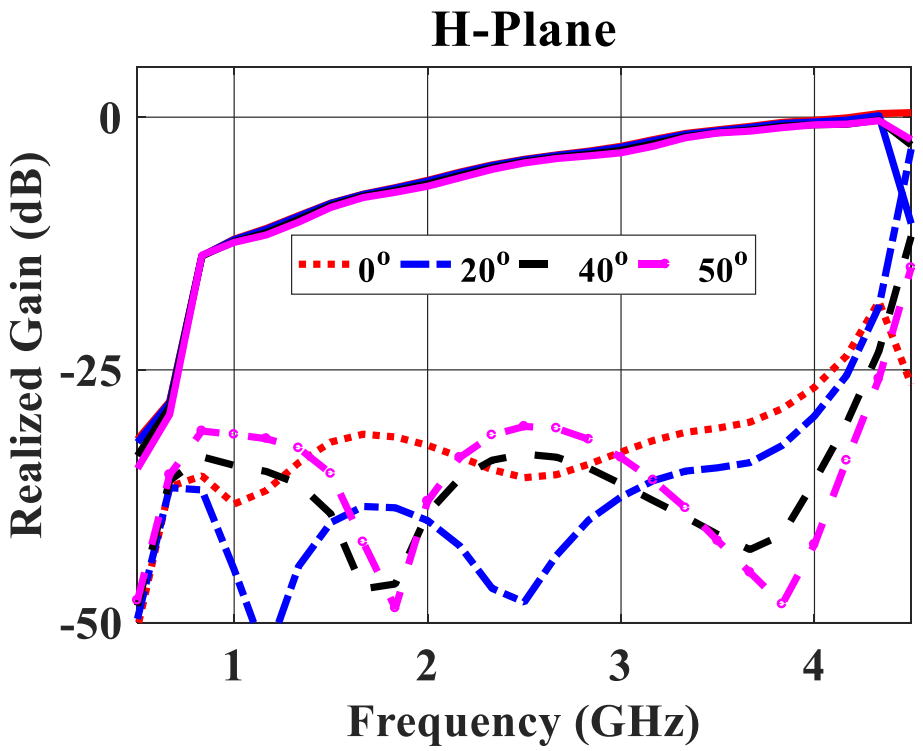
H-Plane
0
-25
-50
Realized Gain (dB)
1
2
3
4
Frequency (GHz)
0°
20°
40°
50°

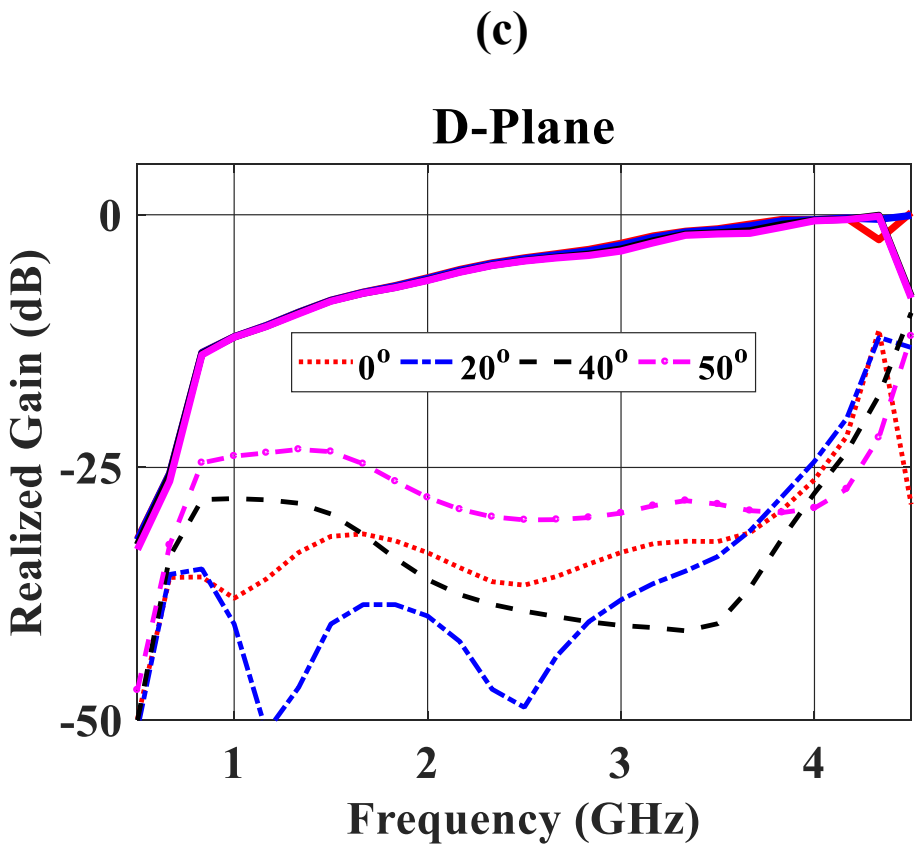

Fig. 3. 11. The Co- and cross-polarization variation with frequency for various scan angles of the infinite array using the DS-MS (0.254 mm thick) superstrate and the shorter balun feed. **(a)** E-plane scan. **(b)** H-plane scan.**(c)** D-plane scan.

The H-plane cross-polarization levels shown in Fig. 3.11 (b), improves across the whole band for the lower scan angles and across the f_H region for all other angles. Around f_L and f_{mid}, the cross-polarization levels are either comparable to or better than those at broadside. The D-plane cross-polarization levels shown in Fig. 3.11 (c), are virtually unchanged around the f_H region and slightly worsens around the f_L and f_{mid} regions for the wider scan angles. These are rather significant results as they indicate that this array can scan to wider angles without worrying about increasing cross-polarization levels. This phenomenon can be attributed to the DS MS-WAIM whose transmission phase variation with frequency for the TM polarized incident fields improves with increasing incidence angles [116].

TABLE 3. 1 - Unit Cell Dimensions (mm)

t_{sup}	L_{add}	h_{air}	L_B	w_{out}	y_1	y_2	y_3	r_1
0.254 →	2.0	5.0	22.71	0.16	5.0	6.0	0.5	1.4
0.508 →	2.5	4.7	22.71	0.16	5.0	6.0	0.5	1.4
	z_1	w_{sp}	w_s	w_{hole}	h_{hole}	t_{gnd}	d_x	d_y
0.254/0.508 →	2.0	0.5	2.0	6.0	3.0	2.0	22.0	22.0

TABLE 3. 2 - Array Performance

t_{sup} *(mm)*	*Array height (mm)*	*E-scan*	*H-scan*	*Range (GHz)*	*Bandwidth*
0.254 →	31.97	70°	55°	0.80-4.38	5.48:1
0.508 →	32.42	50°	55°	0.79-4.32	5.47:1

***Array height = $L_B + L_{add} + h_{air} + t_{sup} + z_1$.**

The DS MS-WAIM discussed earlier is only 0.254 mm thick. This thickness was found to be too thin to hold its shape firmly above the array when constructed. A second array with a DS MS-WAIM thickness of *0.508 mm* was designed with $L_{add} = 2.5$ *mm*, $h_{air} = 4.7$ *mm*, and an overall array height of *32.4225 mm* as shown in table 3.1. The performance comparison of the two arrays is given in table 3.2. The two arrays were found to have the same broadside impedance bandwidth but the second array was about *0.45 mm* taller. It was discovered later that this small increase in height led to a reduction in the E-plane scan. As a proof of concept, the *0.508 mm* MS was used during fabrication instead of the *0.254 mm* one to minimise difficulties during assembly and measurement.

3.4 Results of Fabricated Array

A 10 x 10 prototype of the fabricated array utilizing the *0.508 mm* DS MS-WAIM is depicted in Fig. 3.12. The elements along the first, second, ninth, and tenth columns were terminated by 50 Ω loads to reduce the array edge effects. Only the edge elements along the E-plane were terminated given that the amount of mutual coupling is strongest along this plane and thus have a bigger impact on the edge effects. The active area of the array is the inner 6 x 10 elements. The electrical performance of this array was evaluated in terms of its matching and radiation characteristics.

3.4.1 Antenna Construction

The built array prototype and its constituent parts are shown in Fig. 3.12.

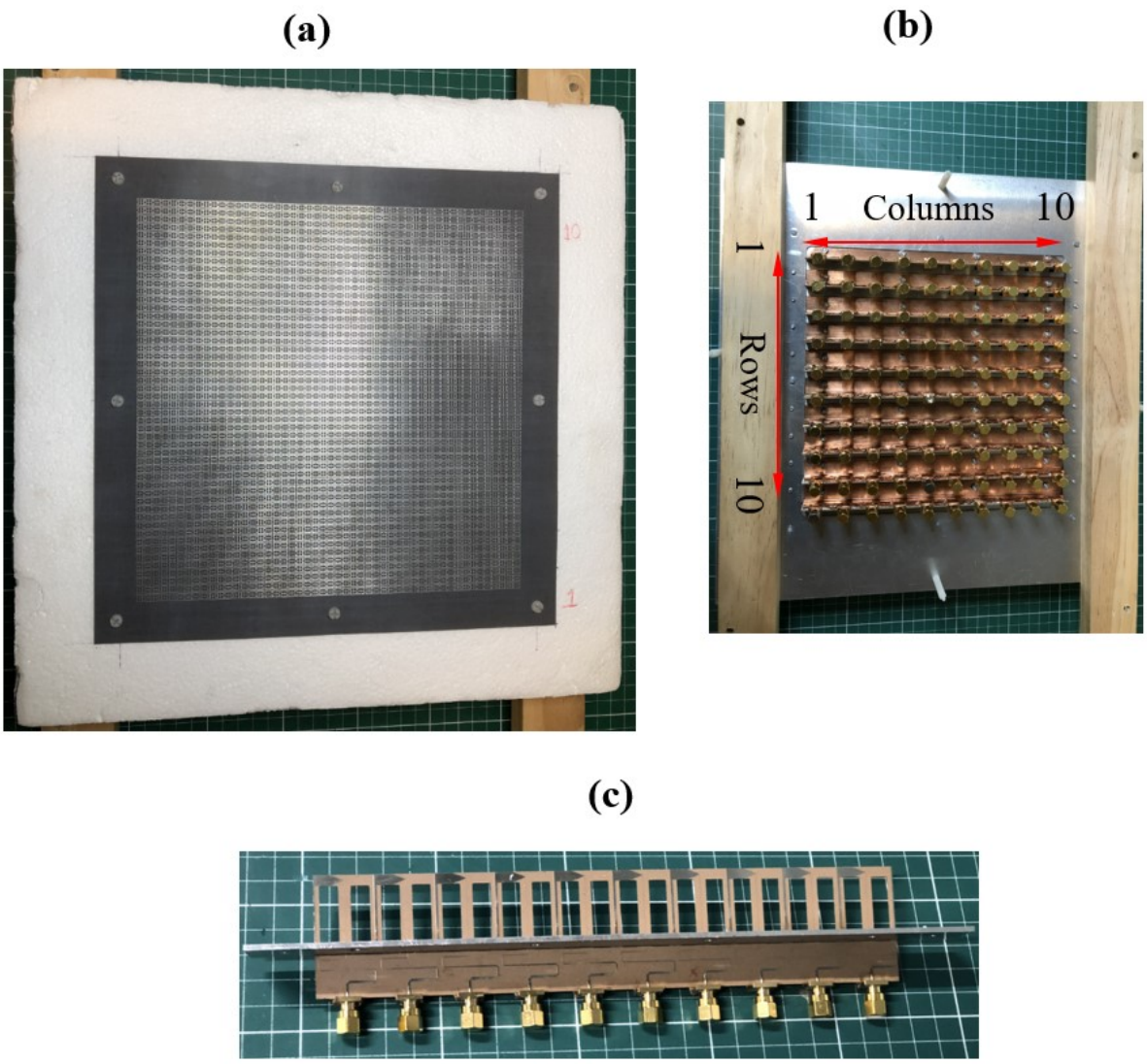

Fig. 3. 12. Constituent parts of antenna prototype. **(a)** Top view of fully assembled array showing DS MS-WAIM and polystyrene foam. **(b)** Bottom view of fully assembled array with 50 Ω terminations and the wooden planks used for mounting. **(c)** A sample antenna card containing 10 tightly coupled antennas attached to a strip of the inner portion of the aluminum ground plane.

The top and bottom of the fully assembled array is shown in Figs. 3.12 (a) and 12 (b) respectively. A block of expanded polystyrene foam ($\varepsilon_r = 1.03$) was inserted into the array to help hold the antenna cards upright and to provide a platform upon which the MS can rest. The MS was held in place by the foam platform and nine precisely cut plastic screws. Strips of copper tape was also used at the top of the array ground plane to enable soldering of the shorting pins from the dipole to the aluminium ground plane.

Below the array ground plane, ninety-degree copper brackets were manufactured and attached to the underside of the array to keep the antenna cards upright. One leg of the bracket was attached to the bottom surface of the array ground plane with metal screws while the other leg is attached to the ground plane portion of the antenna cards with copper tape and solder. Two long wooden planks, *40 mm* wide, were attached to the bottom side of the array ground plane to act as the mounting points during testing.

The array aluminium ground plane is made up of an inner portion that is *2 mm* thick and an outer cage that is *4 mm* thick. The inner ground plane dimension is *264 mm x 264 mm*. It was cut into strips to allow for the insertion of the antenna cards. Each of the ten antenna cards contains ten tightly coupled antenna elements attached to a strip of the inner ground plane as shown in Fig. 3.12 (c). A 2 mm deep by *22 mm* wide portion was machined off on the inside perimeter of the outer ground plane to allow the inner ground plane to sit flush with the outer ground plane. The outer ground plane dimension is *352 mm x 352 mm*.

3.4.2 Active Matching Characteristics

The active reflection coefficient of the built array was calculated from the measured coupling coefficients between the element in row 5 and column 5 (element 5, 5) and every other element in the array. Measurements were carried out using a Keysight Technologies N5225A PNA. During each measurement period, the 98 non-active elements were terminated with 50 Ω loads. The active reflection coefficient for element *i,* scanning in the (θ_o, φ_o) direction can be estimated using [28]:

$$\Gamma_a(\theta_o, \varphi_o) = \sum_{n=1}^{N} S_{ni}|a_n|e^{-jk_o(xd_x sin\theta_o cos\varphi_o + yd_y sin\theta_o sin\varphi_o)} \tag{3.20}$$

where S_{ni} is the measured complex coupling coefficients between element *i* and the other elements of the array, $|a_n|$ is the magnitude of the excitation of the radiating element, *N* is the total number of

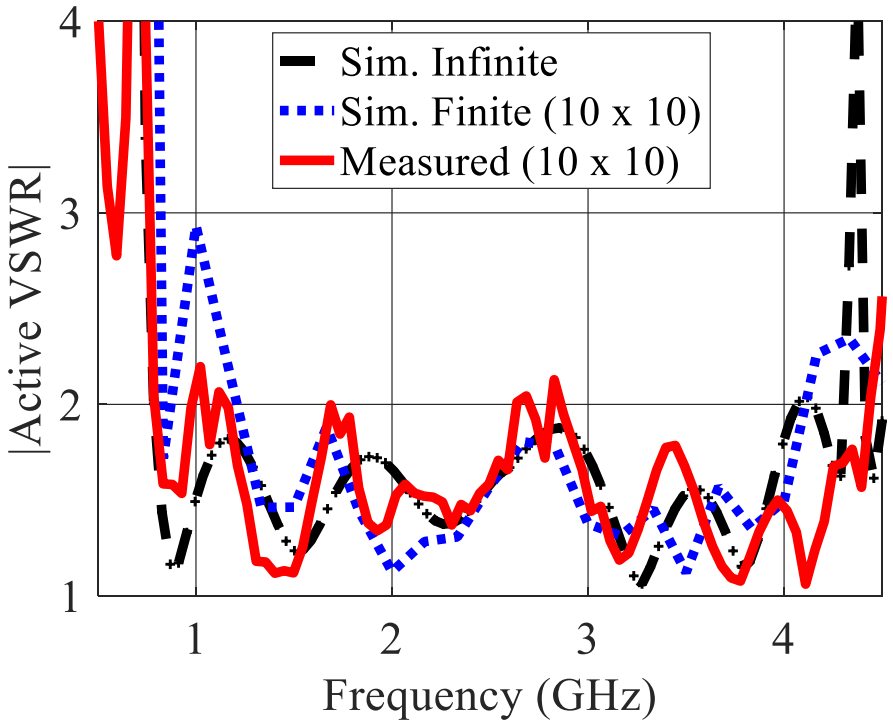

Fig. 3. 13. The broadside active VSWR of the simulated infinite array, the simulated 10x10 finite array with 60 active elements, and the measured results obtained from the measured coupling coefficients.

elements, k_o is the free space wave number, x and y are the element numbers, and d_x and d_y are the element spacings along the ***x***- and ***y***-directions respectively.

The active VSWR was deduced from the active reflection coefficient for broadside and for scanning in the E, H, and D (diagonal) planes. The broadside active VSWR of the simulated infinite array, the simulated 10x10 finite array with 60 active elements, and the measured results obtained from the measured coupling coefficients are displayed in Fig. 3.13. There is a high degree of correlation between the three results across the band from 0.80 GHz – 4.38 GHz. The resonance around 4.4 GHz in the infinite array is less pronounced in the finite array and measured results. There are some ripples on the measured results due to diffraction along the array edges and the finite ground plane. The low frequency behavior of the simulated and measured finite arrays show reduced matching due to the small number of active elements. Better matching can be obtained by using a larger sized array but with significantly higher computational overheads.

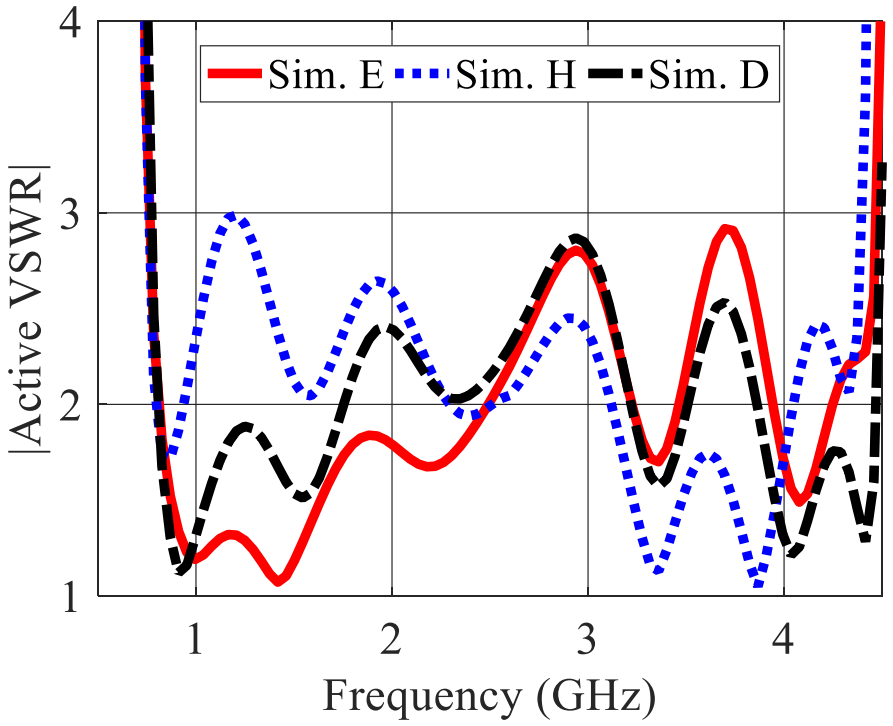

Fig. 3. 14. The scanning active VSWR of the simulated infinite array across all three planes. Scan results shown are for 50° along the E-plane, 55° along the H-plane and 65° along the D-plane.

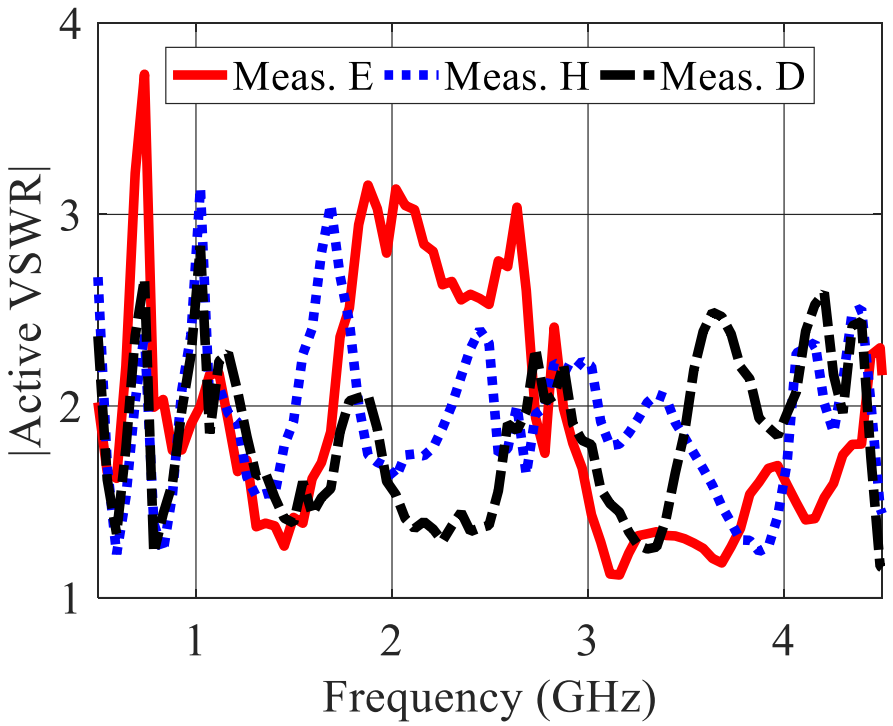

Fig. 3. 15. The scanning active VSWR obtained from the measured coupling coefficients across all three planes. Scan results shown are for 50° along the E-plane, 55° along the H-plane and 65° along the D-plane.

The simulated and measured scanning ability of the array is shown in Figs. 3.14 and 3.15 respectively. The plots for the measured results were obtained by using (3.20) above. The measured and simulated results agree well with each other for scan angles of up to 50° along the E-plane, 55° along the H-plane and 65° along the D-plane all under a VSWR value of 3.2. The array edge effects discussed earlier is manifest more pronouncedly along the E-plane during scan as an increase in the VSWR around mid-band.

3.4.3 Radiation Characteristics

The radiation characteristics of the array in terms of the broadside peak gains, embedded element patterns (pattern of element 5, 5 when all other elements are terminated with 50 Ω loads), and finite array gain patterns are presented in this section.

3.4.3.1 Peak gains

The broadside peak gains were calculated using the following equation:

$$\text{Realized Gain} = 4\pi NA(1-|\Gamma|^2)/\lambda^2 \qquad (3.21)$$

Where N is the total number of elements, A is the area of the unit cell, Γ is the active (all elements excited) or passive (one element excited and the rest terminated in their input impedance) reflection coefficient, and λ is the wavelength.

The ideal broadside peak gain is obtained when the reflection coefficient is assumed to be zero. Referring to Fig. 3.16, the broadside peak gains for the simulated infinite array and the measured results (obtained from the measured active reflection coefficient) agree very closely to the ideal gain when $N=100$. The result for the simulated finite array with 60 excited elements also tracks very closely to the ideal case when $N = 60$.

The passive reflection coefficient, $\Gamma_{5,5}$, was also measured from which the broadside peak gain was calculated. This gain is compared to the measured gain in the anechoic chamber using a standard gain antenna (gain comparison method). The results obtained from the gain comparison method includes all the mismatch and radiation losses unlike the reflection coefficient method which only contain the

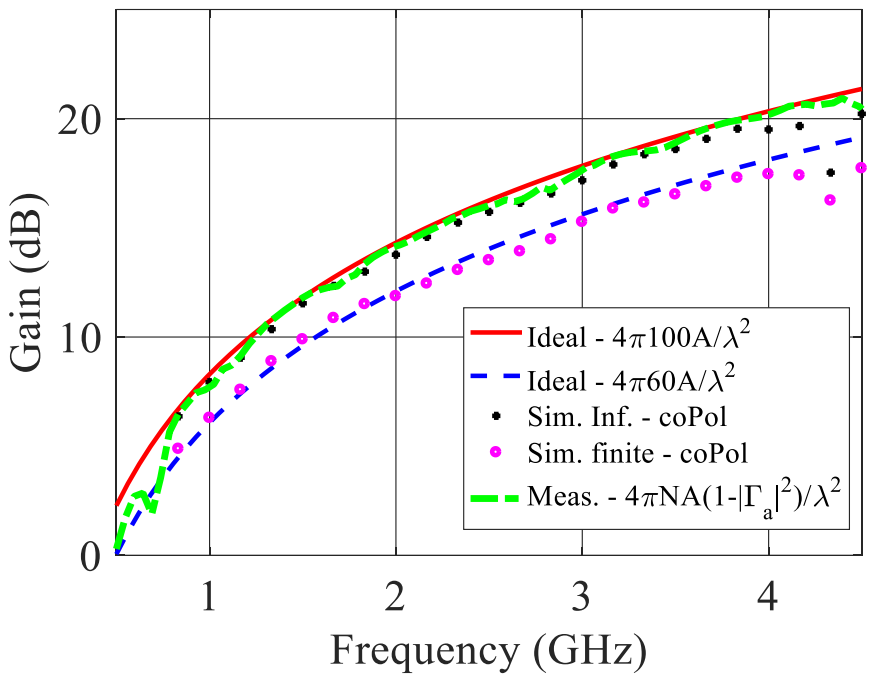

Fig. 3. 16. Measured (obtained from the measured active reflection coefficient) and simulated broadside peak gains of the whole array. The finite array simulation is for 60 active elements with the first two and last two columns of the array terminated in 50 Ω loads.

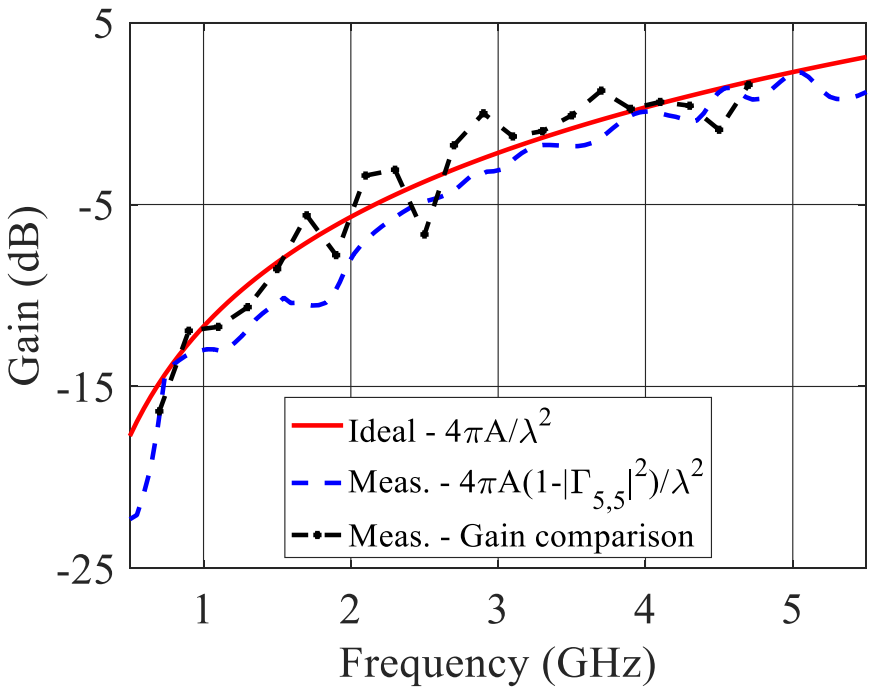

Fig. 3. 17. Measured (obtained from the measured passive reflection coefficient and from the gain comparison method) and ideal broadside peak gains of element 5, 5 with all other elements terminated in 50 Ω loads.

mismatch losses. The results of these measurements are shown in Fig. 3.17 together with the ideal case. The worst-case deviation from the ideal curve is within 2.5 dB which occurs at 1.8 GHz for the reflection coefficient method and at 2.5 GHz and 2.9 GHz for the gain comparison method. These discrepancies are attributed to the small array size and the lack of absorbing material around the cables below the array ground. The copper tape used to hold the antenna cards upright and to enable soldering onto the aluminum ground plane also causes resistive losses resulting in higher than expected gains at certain frequencies. For the rest of the frequency points, there is a high degree of agreement.

3.4.3.2 Embedded element patterns

The embedded element patterns of element 5, 5 were measured in an anechoic chamber and the results compared with simulations. The element patters at 4.1 GHz across the E, H, and D-planes is shown in Fig. 3.18. The simulated and measured results track very well with each other. The small amount of discrepancies is mainly attributed to fabrication imperfections, the small size of the array and ground plane, edge effects, and reflections from the feed cables.

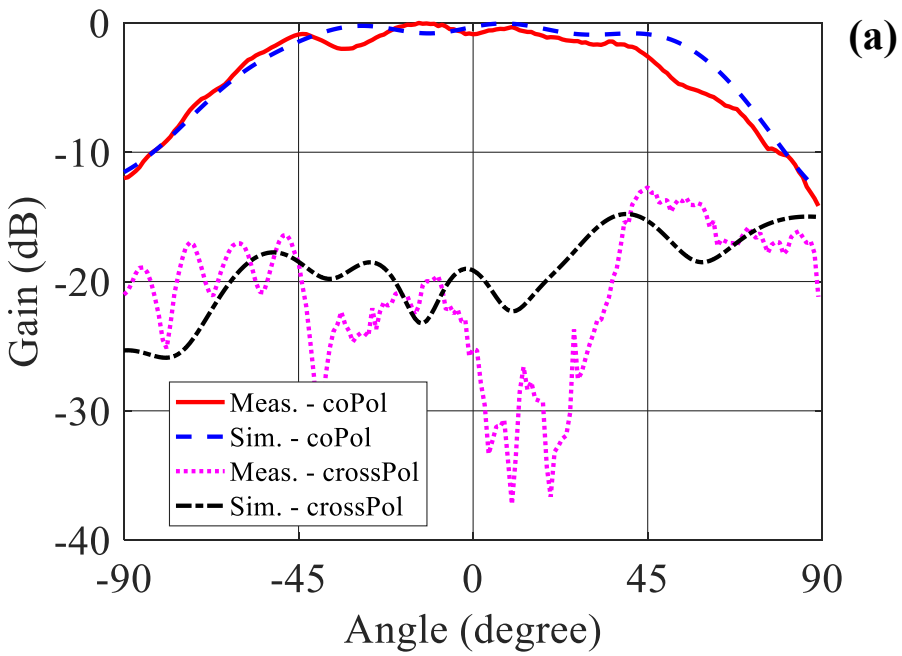

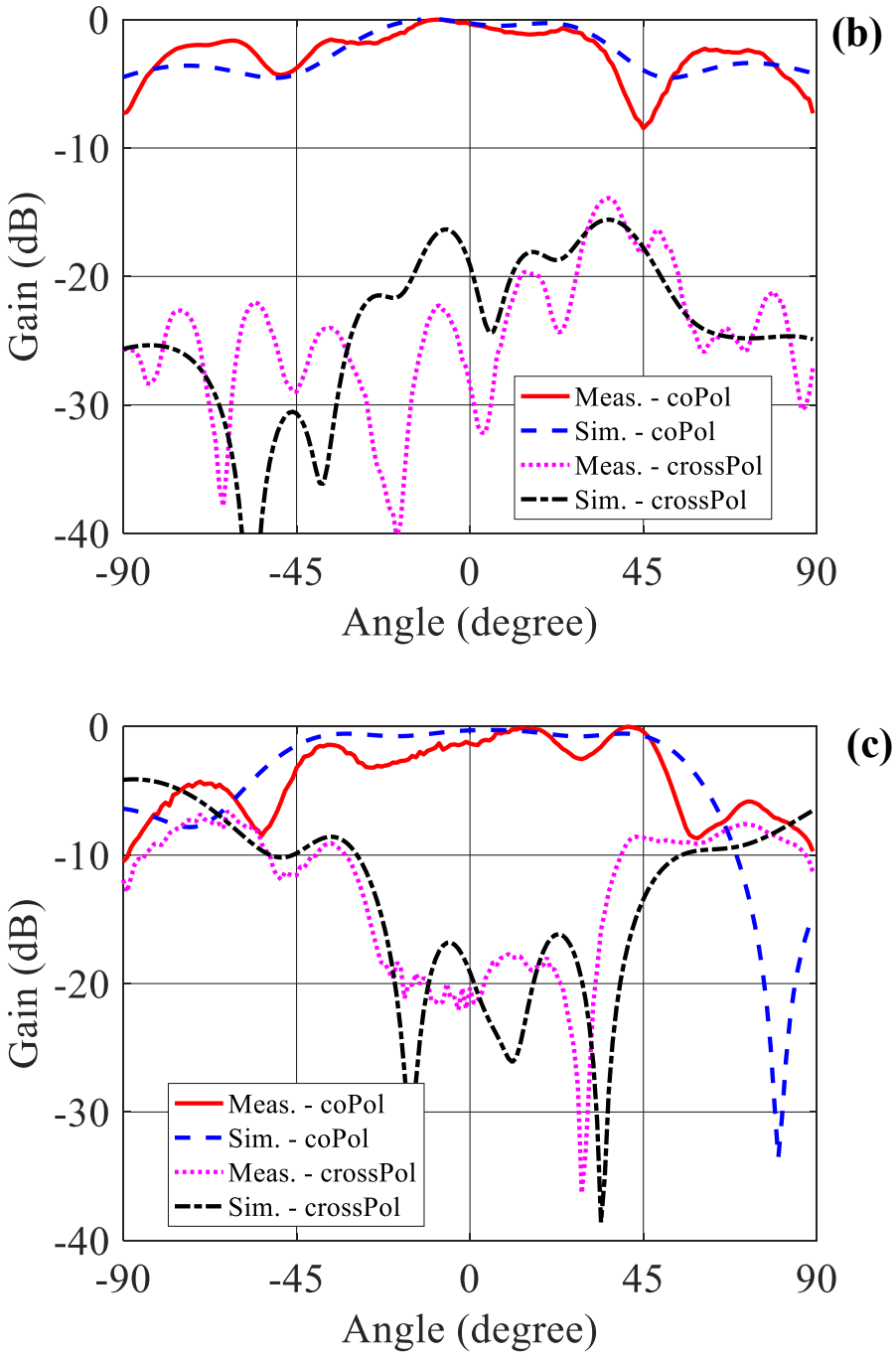

Fig. 3. 18. Embedded element patterns at 4.1 GHz. **(a)** E-plane. **(b)** H-plane. **(c)** D-plane.

3.4.3.3 Finite array patterns

The scanning ability of the array across the E, H, and D-planes, at 4.1GHz are displayed in Fig. 3.19. During E and H-plane scans, the cross-polarization levels improves with scan as was noted in the infinite array simulations. The difference between the co- and cross-polarization levels is > 21 dB for the E and

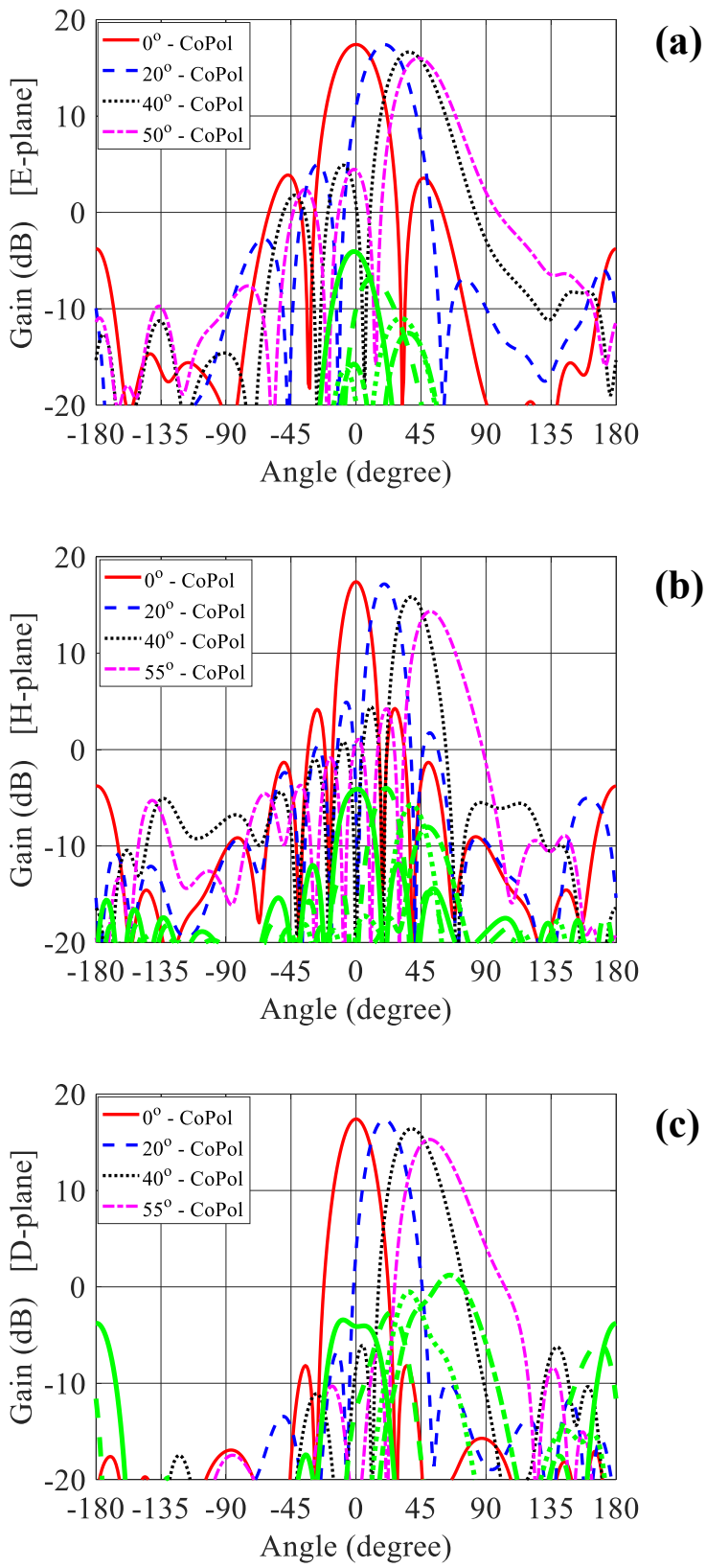

Fig. 3. 19. Finite array gain patterns at 4.1 GHz. The patterns are symmetric for both positive and negative scans but only the positive scans are shown for clarity. The cross polarizations are shown using the green curves. **(a)** E-plane. **(b)** H-plane. **(c)** D-plane.

H-planes, and > 15 dB for the D-plane. The peak broadside gain is 17.42 dB. The maximum scan loss varies from 1.93 dB along the E-plane to 3.3 dB along the H-plane for a maximum scan angle of 55°. The patterns in the negative scan direction are a mirror image of those in the positive direction. For clarity, only the positive scan patterns are shown.

In order to demonstrate the widest scan range of the *0.254 mm* thick DS MS-WAIM design, its E-plane gain pattern for 70° scan is simulated. The edge elements along the E-plane were also terminated in this case in order to obtain a wideband impedance match. The resulting narrower array size causes the beam to spread which leads to an increase in the beam-pointing error for wider scan angles. This behavior corresponds to the fact that the beam pointing error will increase as the array size decreases [117]. To improve the wide angle beam pointing accuracy, the array size was increased from 10x10 elements to 17x17 elements. The consequent beam scanning results for the different array sizes are displayed in Fig. 3.20. It can be seen that the 17x17 array element system provides the desired beam pointing accuracy at 70°.

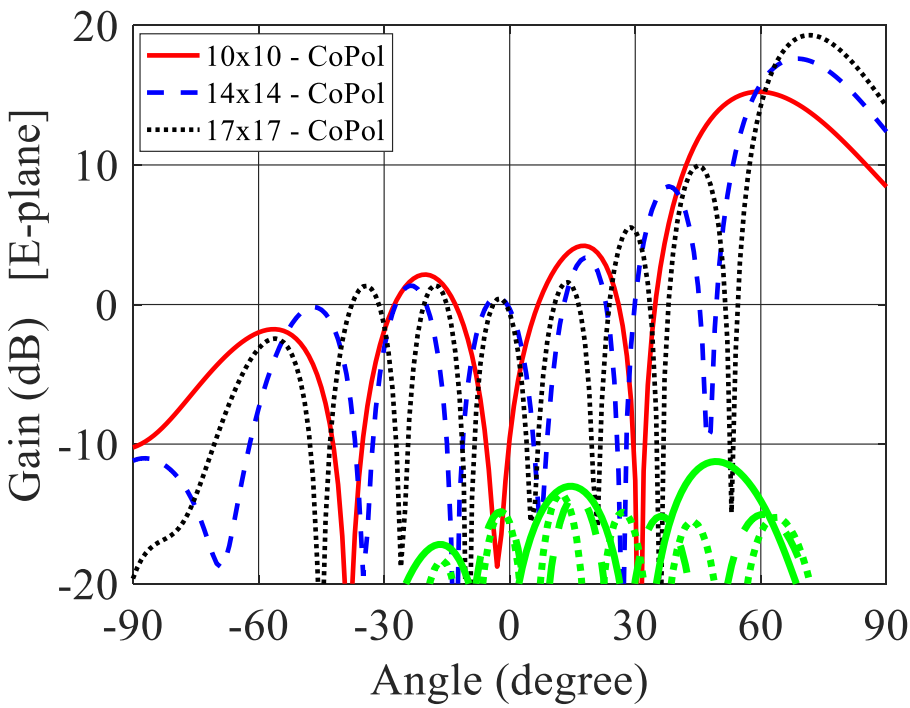

Fig. 3. 20. Simulated E-plane gain patterns pointing at 70° for the 0.254 mm thick DS MS-WAIM design at 4.1GHz. The beam pointing accuracy is shown to improve as the array size is increased from 10x10 to 17x17 elements. The cross polarizations are shown using the green curves.

3.5 Guidelines for Improved Array Design

To further investigate the reasons for the reduction in the E-plane scan of the array prototype described above, a detailed parameter study was carried out on L_{add}, h_{air}, and y_3. This parameter study also serve as guidelines for designing arrays with the widest scan angles whilst maintaining a wide impedance bandwidth.

The parameter study results are presented in Fig. 3.21. The nominal parameter values were: t_{sup}= *0.254 mm,* L_{add} *= 2 mm,* h_{air} *= 5 mm,* and y_3 *= 0.5 mm*. In Fig. 3.21 (a), as t_{sup} is increased, the VSWR around f_L and f_{mid} improves slightly while that around f_H deteriorates more pronouncedly. The direction of the solid arrows in Fig. 3.21 show the change in VSWR relative to changes in the nominal parameter values. From the scanning VSWR plots shown earlier, we can deduce that as the scan angle increases, the E-plane and H-plane scan-deteriorates more pronouncedly around f_H and f_L respectively. This indicates that, increasing the superstrate thickness will reduce the range of the E-plane scan and slightly improve the H-plane scan if no other parameters are adjusted. To improve the E-plane scan, L_{add}, h_{air}, and y_3 needed to be modified. L_{add} was increased while noting that the VSWR at f_L will decrease while that at f_{mid} and f_H will increase as indicated in Fig. 3.21 (b). Both h_{air} and y_3 should also be reduced as the results in Fig. 3.21 (c) and 21 (d) show. A compromise is required between the need to reduce the VSWR at f_H and the corresponding increase around f_{mid} that arises because of the modification of L_{add}, h_{air}, and y_3.

From the study above, it can be clearly seen that the fabricated design was not optimum. To obtain the optimum bandwidth and scan range for the double sided (DS) *0.508 mm* thick superstrate design, h_{air} was reduced from *4.7 mm* to *4.25 mm* in order to equalize its overall array height to that of the *0.254 mm* design. By also changing the dipole overlap, y_3, to *0.6 mm*, the scan range was extended to 75° along the E-plane while maintaining the H-plane at 55° over a 5.75:1 (0.75 GHz – 4.31 GHz) broadside impedance bandwidth as shown in Fig. 3.22 (a). The polarization purity is > 20 dB across the band as can be seen from Fig. 3.22 (b). Increasing the MS thickness improves the scan range and

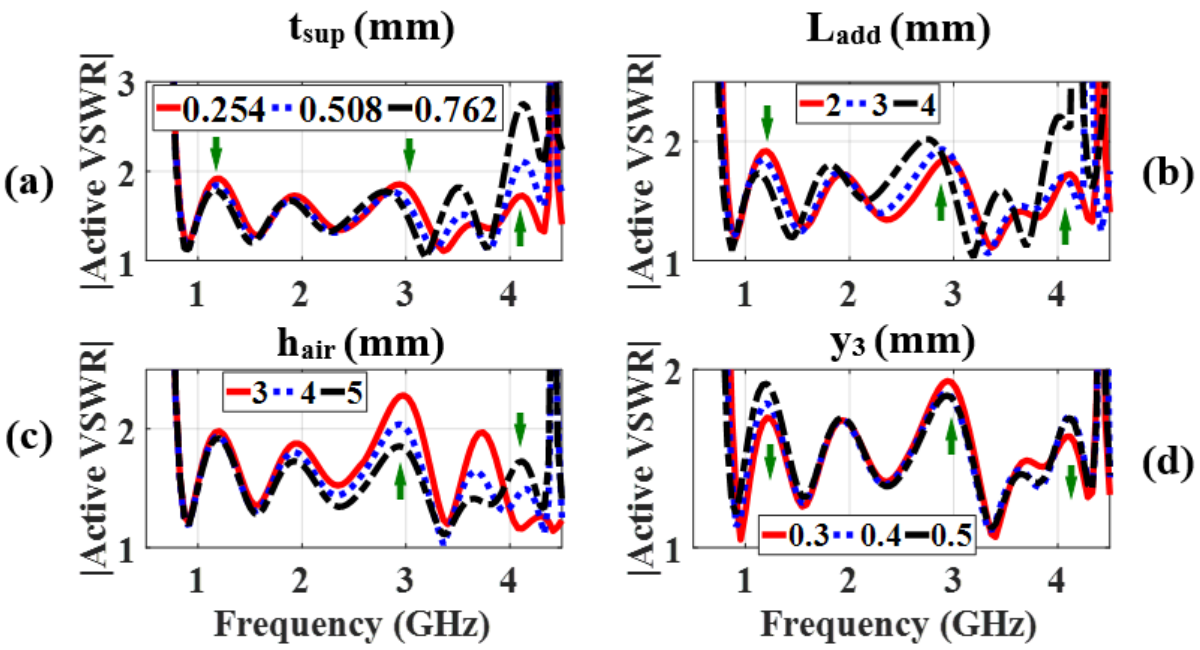

Fig. 3. 21. Parametric study on the effects of **(a)** t_{sup}, **(b)** L_{add}, **(c)** h_{air}, and **(d)** y_3 on the active VSWR. The direction of the green arrows show the change in VSWR relative to changes in the nominal parameter values.

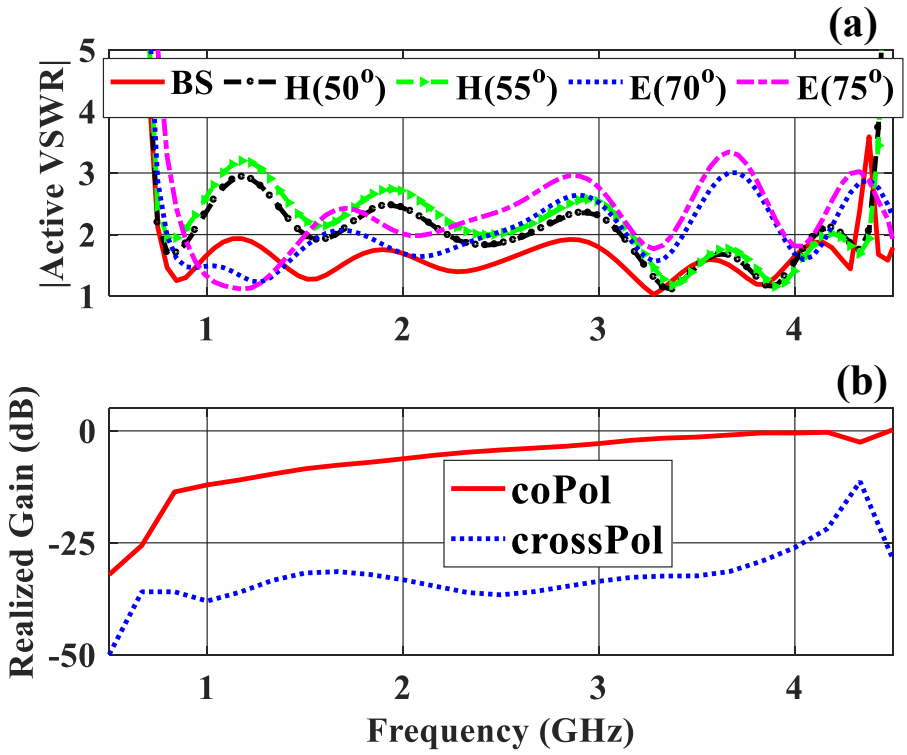

Fig. 3. 22. Optimum design-1 (*0.508 mm*) performance. **(a)** Scanning ability **(b)** Co- and cross-polarized realized gains.

bandwidth provided the array height and capacitive coupling is optimized to the appropriate values. However, it is worth noting that making the MS too thick increases the chance of scan blindness and the likelihood of trapped waves within it.

A second optimized array with a *2.032 mm* thick single sided metasurface (SS-MS) WAIM was also designed. The E-plane scan range was extended to 80° while the H-plane scan, co-, and cross-polarized realized gains remains almost unchanged as shown in Fig. 3.23.

The dimensions and performance parameters of the two optimized arrays are shown in Tables 3.3 and 3.4 respectively. These improved designs were obtained by following the design guidelines listed previously and optimizing the array for both broadside and at the widest scan angles. The DS-MS can achieve similar performance to the SS-MS using a thinner superstrate and a lower profile array, albeit at a huge computational burden. These designs were obtained after the initial prototype had already being built and experimentally validated. Due to cost and time constraints, these optimum designs were not built given that the prototype had already validated the design concepts.

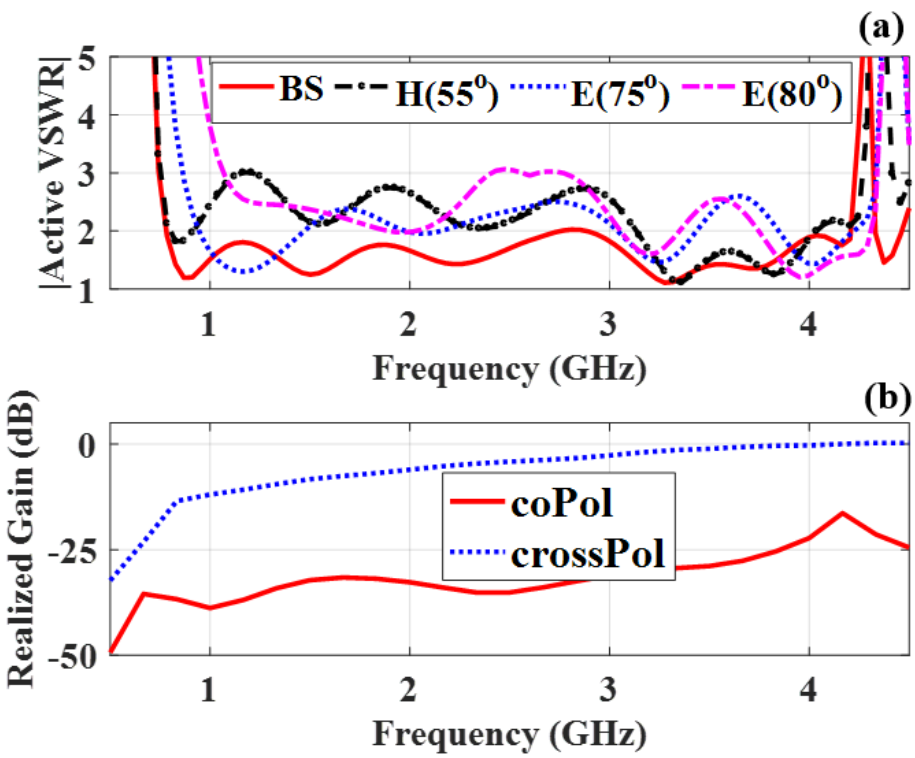

Fig. 3. 23. Optimum design-2 (*2.032 mm*) performance. **(a)** Scanning ability **(b)** Co- and cross-polarized realized gains.

TABLE 3. 3 - Unit Cell Dimensions of Optimum Designs (mm)

t_{sup}	L_{add}	h_{air}	L_B	w_{out}	y_1	y_2	y_3	r_1
0.508 →	2.5	4.25	22.71	0.1551	5.0	6.0	0.6	1.4
2.032 →	3.5	3.6	22.71	0.1551	5.0	6.0	0.5	1.4
	z_1	w_{sp}	w_s	w_{hole}	h_{hole}	t_{gnd}	d_x	d_y
0.508/2.032 →	2.0	0.5	2.0	6.0	3.0	2.0	22.0	22.0

TABLE 3. 4 - Array Performance of Optimum Designs

t_{sup} *(mm)*	*Array height (mm)*	*E-scan*	*H-scan*	*Range (GHz)*	*Bandwidth*
0.508 →	31.97	75°	55°	0.75-4.31	5.75:1
2.032 →	33.85	80°	55°	0.77-4.20	5.46:1

***Array height = $L_B + L_{add} + h_{air} + t_{sup} + z_1$.**

3.6 Discussion

To quantify the implication of our work in terms of fundamental limits and in comparison to other wideband PEC-backed antenna arrays, the array figure of merit [108] is utilised. The array figure of merit is a single number which takes into account the bandwidth, scan range, and total efficiency, for a given array height. The total efficiency is a combination of the radiation and mismatch efficiencies. According to [108], the definition of the array figure of merit depends on whether the array is lossy or if it has negligible losses. For arrays with negligible losses:

$$P_A = B\log(1/\Gamma_{max})/\cos\theta_{max} \quad (7)$$

Where $B = (\omega_{max} - \omega_{min})/\sqrt{(\omega_{max}\omega_{min})}$, θ_{max} is the maximum scan angle, Γ_{max} is the worst-case reflection coefficient, and log is the natural logarithm. For lossy arrays:

$$P_A = B|\log(1-\eta_{min})|/2\cos\theta_{max} \quad (8)$$

Where η_{min} is the minimum of the total efficiency. The total efficiency of the array with the *0.254 mm* and the *0.508 mm* (fabricated prototype) superstrates are displayed in Fig. 3.24. The total efficiency values are shown for broadside and for the widest scan angles. The broadside total efficiency is > 78 % for both designs. For the *0.254 mm* design, the total efficiency is > 62 % for scan angles up to 70°. For the *0.508 mm* design on the other hand, the total efficiency is > 70 % for scan angles up to 55°.

Equation (8) was used to calculate the figure of merit and the electrical thickness, k_0h, where k_0 is the free space wave number and h is the array height measured from the array ground plane to the top

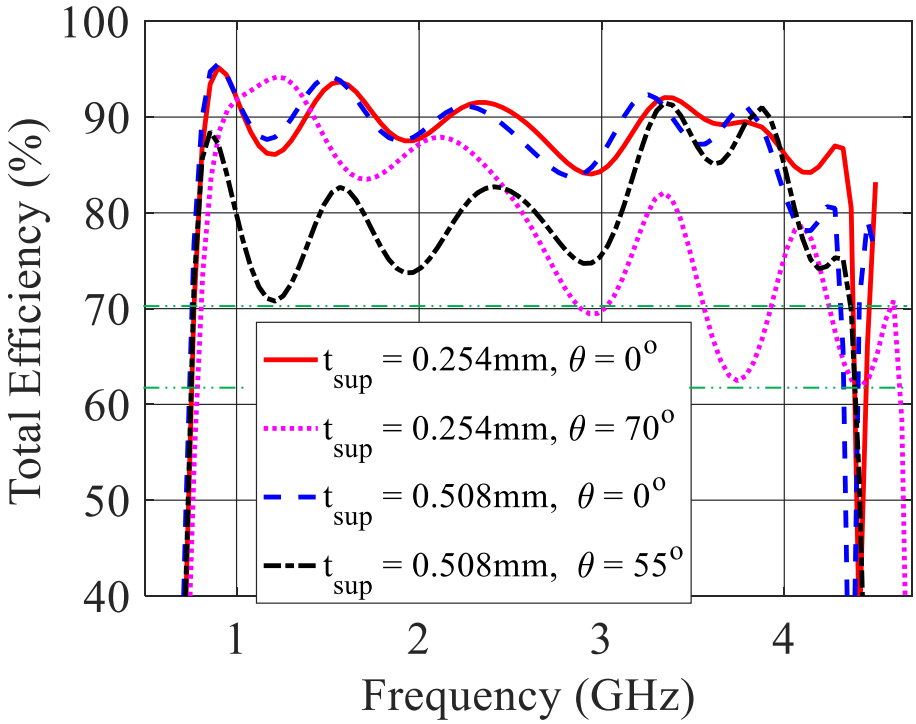

Fig. 3. 24. The total efficiency of the array with the *0.254 mm* and the *0.508 mm* (fabricated prototype) superstrates. Total efficiency values are shown for broadside and for the widest scan angles.

TABLE 3. 5 - Computed P_A and k_0h values

t_{sup} *(mm)*		f_{min} *(GHz)*	f_{max} *(GHz)*	*B*	η_{min}	θ_{max} (°)	P_A	k_0h
0.254 mm	At broadside	0.80	4.38	1.91	0.80	0	1.54	1.33
	At θ_{max}	0.79	4.63	2.01	0.62	70	2.84	1.36
0.508 mm	At broadside	0.79	4.32	1.91	0.78	0	1.45	1.31
	At θ_{max}	0.76	4.36	1.98	0.7	55	2.08	1.29
0.508 mm (optimum-1)	At broadside	0.75	4.31	1.98	0.82	0	1.70	1.27
	At θ_{max}	0.79	4.63	2.01	0.62	75	3.75	1.36
2.032 mm (optimum-2)	At broadside	0.77	4.20	1.91	0.85	0	1.81	1.27
	At θ_{max}	1.05	4.34	1.54	0.71	80	5.49	1.51

of the array at the centre frequency $\omega_0 = \sqrt{(\omega_{low}\omega_{high})}$. The calculated results for the *0.254 mm* and *0.508 mm* (fabricated prototype) designs are shown in table 3.5 and plotted in Fig. 3.25 in bold green and grey respectively. The circles represent broadside performance and the crosses represent scanning performance along the E or H planes.

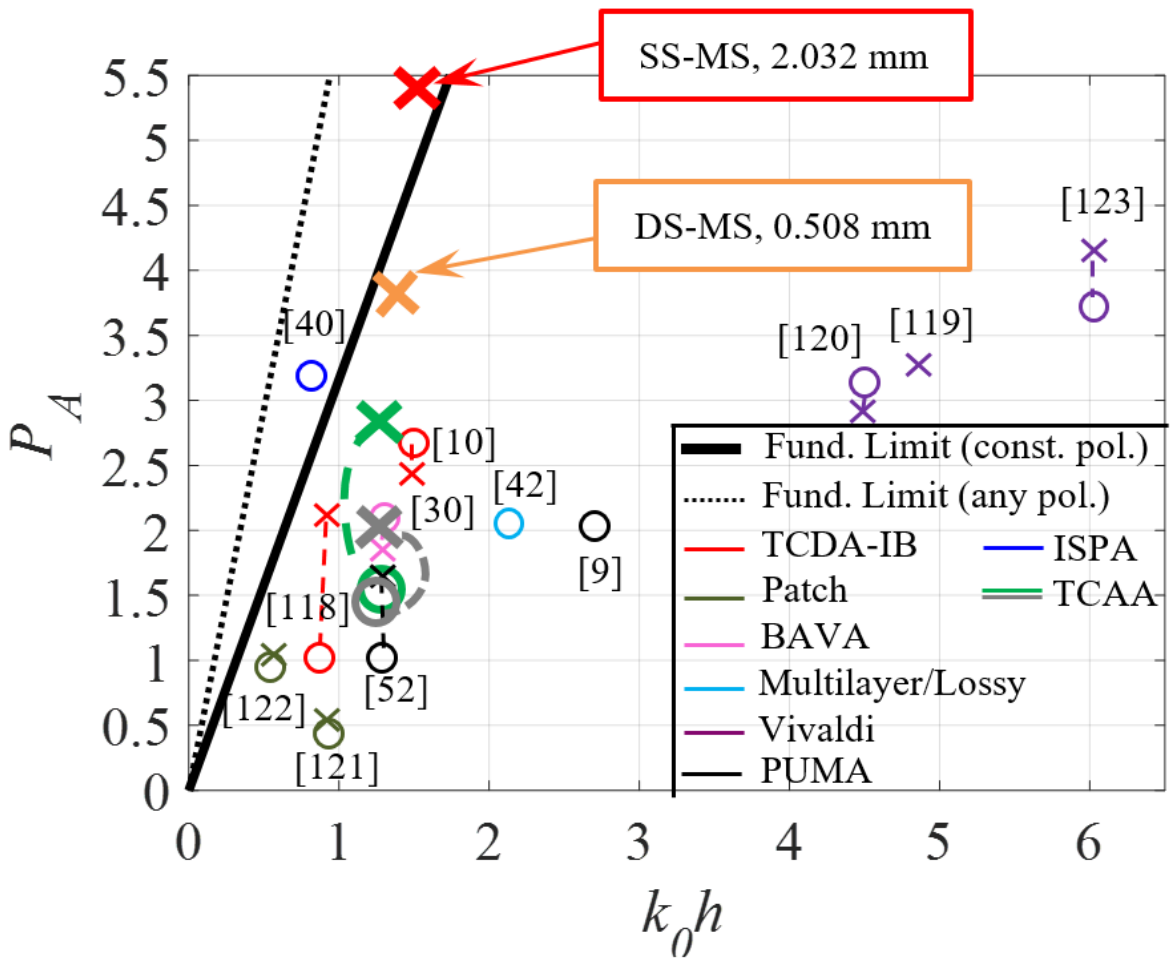

Fig. 3. 25. Performance comparison of wideband PEC-backed antenna arrays using the array figure of merit (P_A) versus electrical thickness (k_0h) plot. This figure is reproduced here courtesy of the work done in [108] with the addition of some recently reported works. The fabricated array and the working design that was used to establish the design guidelines are shown in bold grey and bold green respectively. The improved designs are shown in bold orange and bold red. The circles represent broadside performance and the crosses represent scanning performance along the E or H planes.

The efficiencies and the figures of merit for the two optimum designs were also obtained. The efficiency plot of optimum design-1 (*0.508 mm*) is shown in Fig. 3.26. Its radiation efficiency is > 87 % for all scan angles across the band and its total efficiency is > 80 % at broadside and > 62 % for 75° scan along the E-plane. The array figure of merit for this design is also calculated and displayed in table 3.5 and plotted in Fig. 3.25 in bold orange.

The total efficiency for broadside and for 80° scan along the E-plane for optimum design-2 (*2.032 mm*) is given in Fig. 3.27. Its radiation efficiency is > 90 % for all scan angles across the band

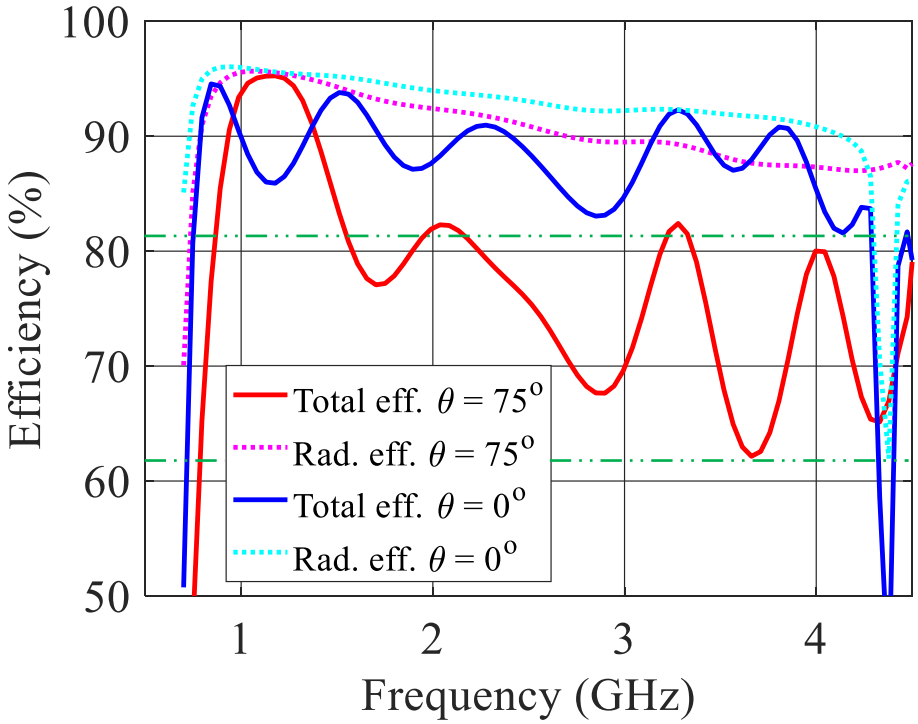

Fig. 3. 26. Simulated total and radiation efficiencies of optimum design-1 (*0.508 mm)* at broadside and at 75° scan.

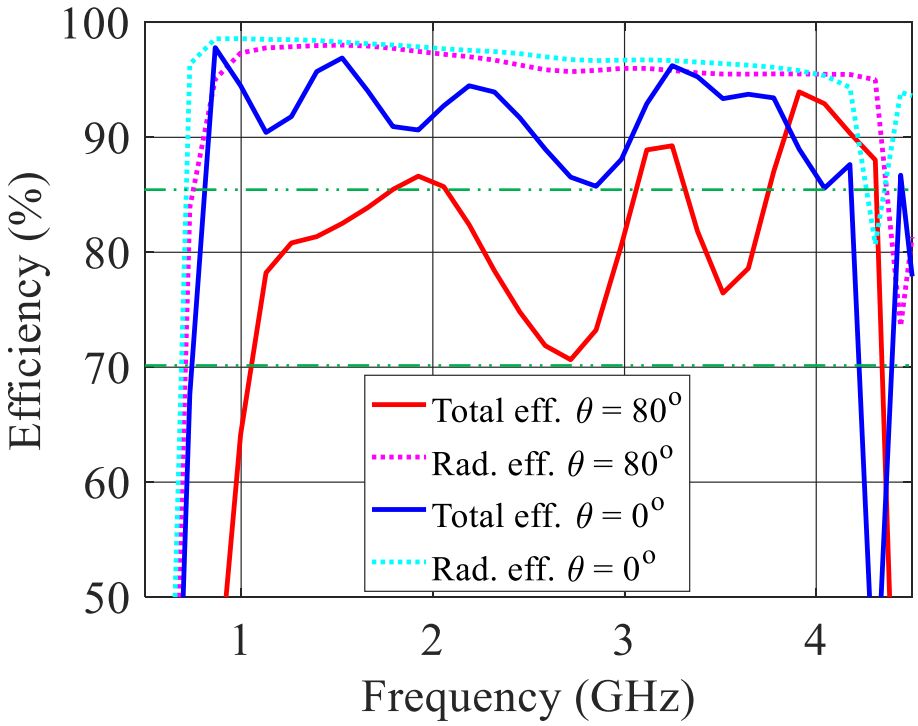

Fig. 3. 27. Simulated total and radiation efficiencies of optimum design-2 (*2.032 mm)* at broadside and at 80° scan.

and its total efficiency is > 80 % at broadside and > 70 % for 80° scan along the E-plane. The array figure of merit for this design is also calculated and displayed in table 3.5 and plotted in Fig. 3.25 in bold red. From Fig. 3.25, it can be clearly seen that the performance of the optimum arrays presented in this chapter has the highest P_A values compared to other similar designs in the literature. In addition, they approach the fundamental limit of arrays with constant polarisation.

3.7 Chapter Conclusion

This Chapter presents a wideband antenna array with an integrated low-profile balun. The balun is simple and compact facilitating an overall array height of just 0.088 λ_L. For the optimum SS-MS design, a bandwidth of 5.5:1 was achieved while scanning to 80° in the E-plane and 55° in the H-plane for an active VSWR value of 3.1. In addition, the fact that the balun and dipoles are printed on the same substrate, ensures simplicity in construction and cost reduction. Due to the unique ability of the MS-WAIM to improve the impedance matching as the scan angle increases, the resulting cross-polarization levels decreases instead of increasing as is usually the case. A 10 x 10 array prototype was fabricated and tested. The measured and simulated results agree quite well. A set of design guidelines were established for designing arrays with the highest figures of merit that approach the fundamental limits. Further improvements to the array can be achieved by extending the H-plane scan range, increasing the array size for better radiation and matching characteristics, implementing a dual polarization setup, and using a stripline or substrate integrated waveguide (SIW) feed to reduce unwanted feed coupling. This wideband, wide scanning, array with an integrated low profile feed can serve as a multifunctional phased array for various radar, communication, and sensing applications.

Section II – Fabry-Perot Antennas

Chapter 4 – Wideband Multi-resonant Fabry-Perot Antenna

4.1 Chapter Introduction

In the previous Chapters, we presented the design and fabrication details of the component parts of a wideband tightly coupled antenna array (TCAA). However, these antennas can be quite costly and the complexity of their feed networks renders them impractical for some applications. In this chapter, we present an alternative solution in the form of a wideband, low-cost, low-profile, and highly efficient Fabry-Perot antenna (FPA) empowered by a novel multi-resonant metasurface (MS) superstrate. FPAs are highly directive with simpler, less lossy, and cheaper feed networks compared to antenna arrays and reflector antennas for example [124, 125]. On the other hand, the FPA is inherently narrow band and existing gain bandwidth improvement attempts has shown marginal success.

A typical FPA consists of a superstrate placed about half a wavelength above a metallic ground plane with a low directivity antenna used to excite the resonant cavity created. The superstrate of a FPA, whether single or multi-layered, is mostly created from uniform dielectric slabs or some type of 2-D or 3-D partially reflective surface (PRS) [126 - 129]. The metallic ground plane can also be replaced by an artificial magnetic conductor (AMC) to reduce the antenna profile. The high directivity of the FPA at boresight is due to the constructive addition of the direct signals from the source antenna and those from the multiple reflections between the partially reflective superstrate and the ground plane [125, 130]. The modes within the cavity are propagating in the broadside direction and evanescent in the transverse direction, thus eliminating the need for reflective sidewalls [131]. Other alternative names of these antennas that indicate the mechanism of operation include 2-D leaky wave antennas, resonant cavity antennas, and electromagnetic band gap (EBG) resonator antennas. Due to their numerous advantages, FPAs find many applications in areas such as satellite communications, electronic warfare, sensor networks, and point-point- links. Although the directivity of FPA can be very high, the gain bandwidth (GBW) can be quite narrow due to the inverse relationship between the two [132], which poses a limitation on their applicability.

In this Chapter, a new method is reported that enhances the 1-dB and 3-dB GBWs of FPAs. Unlike the usual method of bandwidth extension using multiple superstrate layers, this new approach uses a single multi-resonant superstrate to create multiple resonances satisfying the resonance condition. This ensures substantial bandwidth extension without further increase in height. The superstrate consists of a patch-type and an aperture-type MS (PMS and AMS) placed on the top and bottom surfaces, respectively, of a Rogers 5880 dielectric. The metasurface elements are tightly coupled to each other which facilitates a uniform current distribution on the aperture leading to wideband operation and high aperture efficiency. This is another implementation of Wheeler's uniform current sheet concept as discussed more extensively in Chapters 1 – 3. The PMS behaves like a low-pass filter with nearly 0° reflection phase. The AMS acts like a conventional PRS with a high-pass filter response [133, 134]. In addition, by inserting varied thicknesses of dielectric slabs within the cavity, the 1-dB or 3-dB GBWs can be enhanced while reducing the antenna height.

Using this new method, two antennas are designed, fabricated and measured. For both designs, the total antenna size is $2.1\lambda_C$ x $2.1\lambda_C$ x $0.66\lambda_C$ at the central frequency (11.8 GHz) and the aperture efficiency at the peak gain is 64%. The aperture size for the stated efficiency is $1.7\lambda_C$ x $1.7\lambda_C$. The first design had a measured 1-dB GBW of 24% and a 3-dB GBW of 42% with a peak gain of 13.4 dBi. The second design had a measured 3-dB GBW of 40% with a peak gain of 14.3 dBi. Because of the small foot print of the antenna, it is suitable for space limited applications or as an element in a sparse antenna array for further increases in directivity. At the same time, the number of active elements will be significantly reduced compared to the dense TCAAs leading to substantial cost reductions.

This Chapter is organized as follows. Section 4.2 describes the operating principles of the multi-resonant MS by parametric analysis and the equivalent circuit method. A truncated version of the FPA is designed in section 4.3 and experimentally validated in section 4.4. Finally, our conclusions are presented in Section 4.5.

4.2 Background Theory of FPAs

The operation of the FPA can be explained in terms of ray optics as first highlighted in [13]. In this model, it is assumed that the structure is infinite, there is no higher order mode couplings, and no diffraction along its edges. A single cavity FPA with a frequency selective surface (FSS) otherwise known as a partially reflective surface (PRS) superstrate, about half a wavelength above a PEC ground plane is shown in Fig. 4.1. The cavity is excited by a single waveguide antenna.

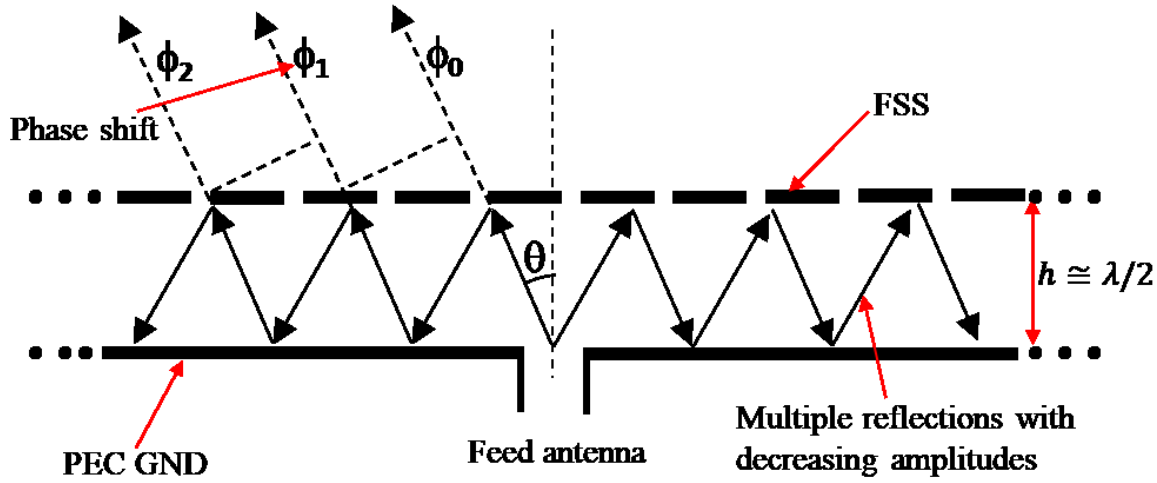

Fig. 4. 1. A ray optics representation of a single cavity FPA.

The excited electromagnetic (EM) waves will be reflected multiple times between the partially reflective superstrate and the PEC ground plane with decreasing amplitudes. The EM waves will eventually emerge out of the partially reflective superstrate but with a certain phase shift, increasing in integer multiples of 2π, due to the differences in path length. Maximum power is obtained at the cavity resonance where the EM waves will add up in phase satisfying the phase condition given in (4.1):

$$\phi_R = \frac{4\pi f h}{c} - \phi_G + 2N\pi \tag{4.1}$$

where φ_R , φ_G are the reflection phase of the FSS and ground plane respectively, h is the resonance height, c is the speed of light, f is the resonance frequency, and N = 0, 1, 2, …. According to (4.1), to

increase the GBW of FPAs, the reflection phase response of the FSS at the cavity resonance should be positive and increase linearly with frequency [78].

For an infinitely large superstrate, the maximum directivity improvement of the FPA with respect to the source antenna can be estimated using its reflection magnitude, $|\Gamma_R|$ [127],

$$D = \frac{1 + |\Gamma_R|}{1 - |\Gamma_R|} = D_f - D_0, \tag{4.2}$$

where D_f and D_0 are the directivities of the FPA and source antennas respectively. From (4.2), it can be deduced that the maximum directivity is obtained when the FSS is highly reflective ($0.5 < |\Gamma_R| < 0.9$) and placed at the resonant height. Because of the inverse relationship between directivity and GBW [132], the reflection magnitude cannot be made too high otherwise the resulting antenna will be extremely narrowband.

The electric field intensity in the far field can be obtained by adding all the partial rays and the results is given by:

$$E = \sum_{n=0}^{\infty} f(\theta) E_0 R^n \sqrt{1 - R^2} e^{j\varphi_n} \tag{4.3}$$

where $f(\theta)$ is the radiation pattern of the source, $R^n\sqrt{1 - R^2}$ is the amplitudes of the transmitted signals, and φ_n represent the phases of the transmitted signals.

4.3 Multi-resonant Superstrate Design

In this section, a new type of multi-resonant superstrate is introduced for wideband low-profile FPAs [124]. The superstrate consists of a PMS and an AMS placed on the top and bottom surfaces of a dielectric, in this case Rogers 5880. The PMS behaves like a low-pass filter with nearly 0° reflection phase. The AMS acts like a conventional PRS with a high-pass filter response [133, 134]. This multi-resonant superstrate is expected to significantly enhance the bandwidth of the traditionally narrowband FPA without resorting to multi-layered superstrates. To realize the wide bandwidth performance, the resonances should be designed to match each other to achieve identical and positive reflection phases

which increase linearly with frequency, in concordance with the phase condition [125] given in (4.1). The magnitude of the resonances should also remain fairly constant with frequency [127].

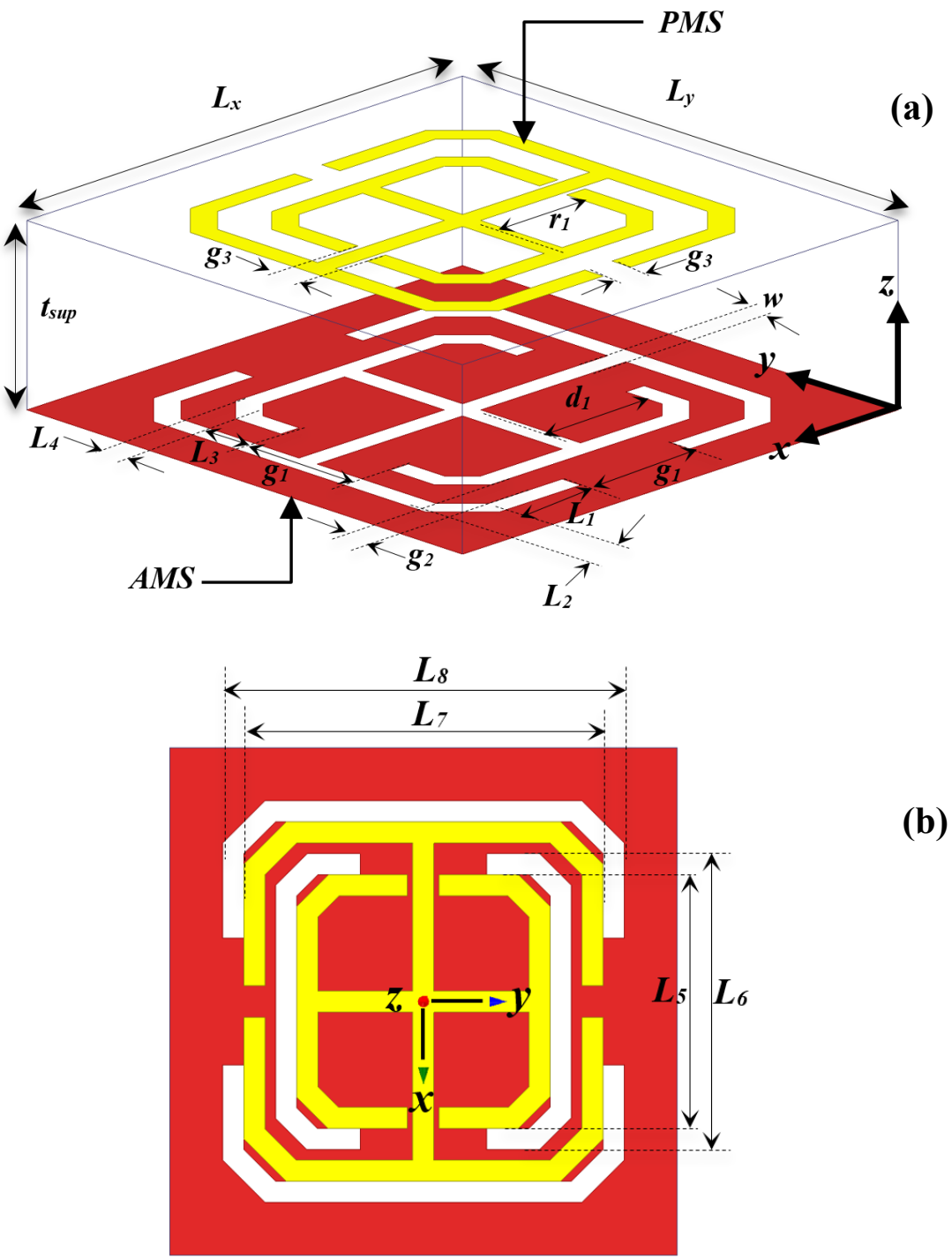

Fig. 4. 2. The multi-resonant superstrate unit cell. (a) Perspective view with the top side showing the patch-type MS (PMS) and the bottom side showing the aperture-type MS (AMS). Dimensions are given in millimeters for resonance at 10 GHz. $w = 0.2$, $t_{sup} = 1.5748$, $g_1 = 1.2$, $g_2 = 0.3$, $g_3 = 0.3$, $L_1 = 0.9$, $L_2 = 0.4$, $L_3 = 0.5$, $L_4 = 0.3$, $L_x = L_y = 4.8$, $r_1 = 1.0$, and $d_1 = 1.2$. (b) Top view with dimensions $L_5 = 2.4$, $L_6 = 2.8$, $L_7 = 3.4$, and $L_8 = 3.8$. The substrate is Rogers RT/Duroid™ 5880 with $\varepsilon_r = 2.2$ and $\tan\delta = 0.0009$.

The detailed dimensions of the superstrate for a 10 GHz resonance are shown in Fig. 4.2. The difference in dimensions between the patch and aperture layers is mainly in the gap openings (g1 and g3) and the inner radii (r1 and d1). The width of the traces and slots in the two layers are the same. The basic structure of the MS element was first introduced in [116]. In the following sections, a detailed parametric study is carried out to fully characterize the superstrate structure and then its equivalent circuit is analyzed with the aid of a Smith chart. In the following sub-sections, we shall refer to the geometry shown in Fig. 4.2.

4.3.1 Superstrate Unit Cell Design

Full wave simulations were carried out on the multi-resonant unit cell shown in Fig. 4.2 using the 3D Electromagnetic software, ANSYS-HFSS. Master-slave periodic boundary conditions and two Floquet ports were employed to replicate an infinite array environment. Port-1 is located on the PMS side of the superstrate and port-2 is located on the AMS side. The TE polarized incident wave is aligned with the x-axis while the TM-polarized incident wave is aligned with the y-axis. Preliminary studies involved carrying out optimizations on g_1, g_2, g_3, r_1, and d_1 while keeping $L_x = L_y = 4.8$ mm and $t_{sup} = 1.5748$ mm to obtain a positive reflection phase at 10 GHz (single-resonance). Next, parametric studies were carried out on the patch-size, r_1 (L_7), and aperture-size, d_1 (L_8), while keeping the other dimensions fixed. This was followed by studies on the effect of varying the superstrate thickness, t_{sup}, and its permittivity value, ε_r, to increase the number of resonances.

4.3.1.1 Parametric study on patch (r_1) and aperture (d_1) sizes - single resonance

For variation in the patch size, d_1 was fixed at 1 mm while r_1 is varied from 1 mm to 1.4 mm for both TE and TM polarizations. The result of this study is given in Fig. 4.3. For the TE-polarized case in Fig. 4.3 (a), as the patch size increases, the resonance frequency decrease by about 2.5 GHz but the overall shapes of the curves for $|S_{22}|$ and the $\angle S_{22}$ remains almost unchanged. For the TM-polarized case in Fig. 4.3 (b) on the other hand, increasing the patch size reduces the resonance frequency albeit at a lower rate. However, both the phase and magnitude curves becomes highly distorted when r_1 becomes larger than d_1.

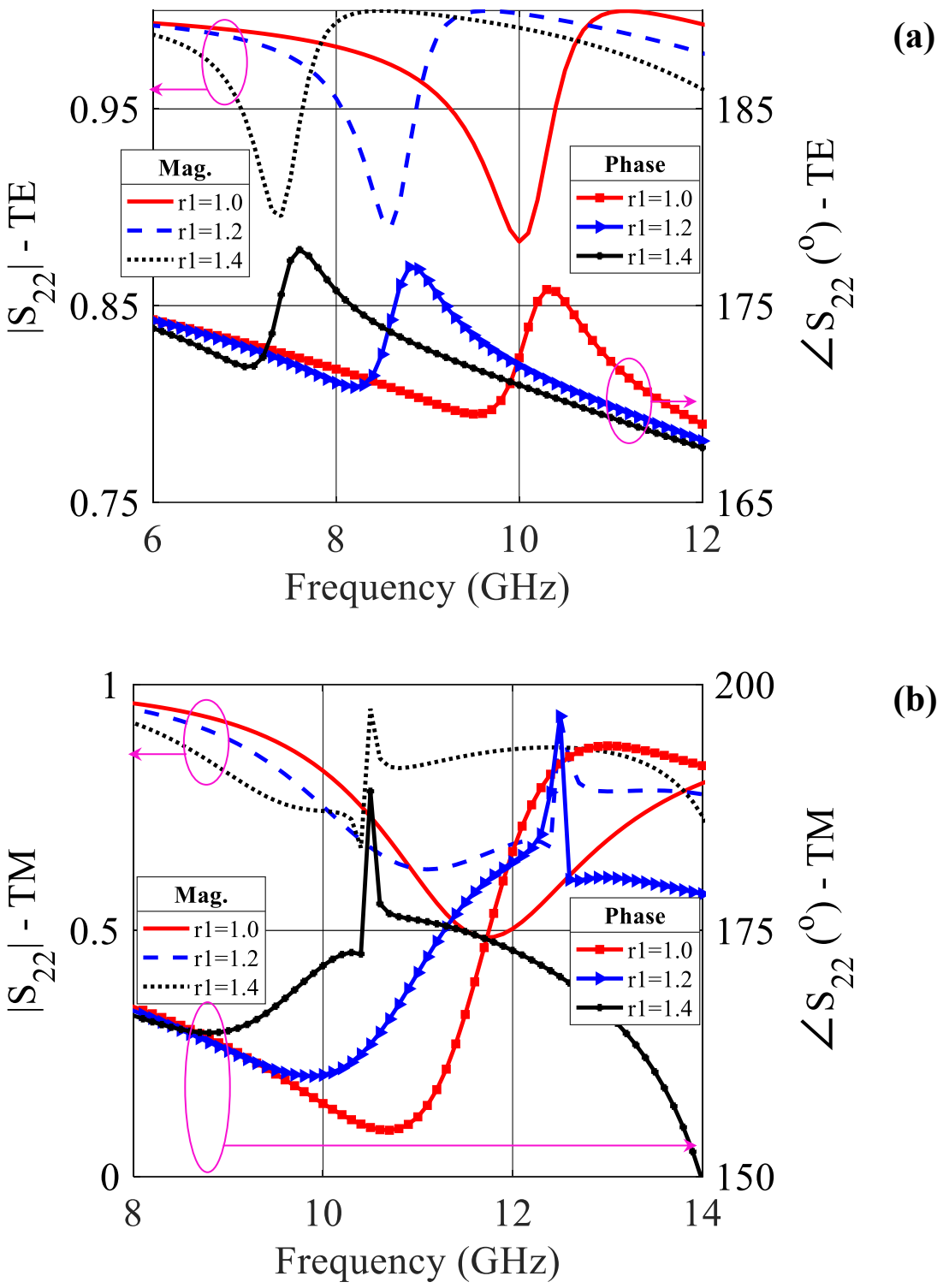

Fig. 4. 3. Dependence of substrate reflection on changing the patch size (*d1 = 1 mm*). (a) TE polarization. (b) TM polarization.

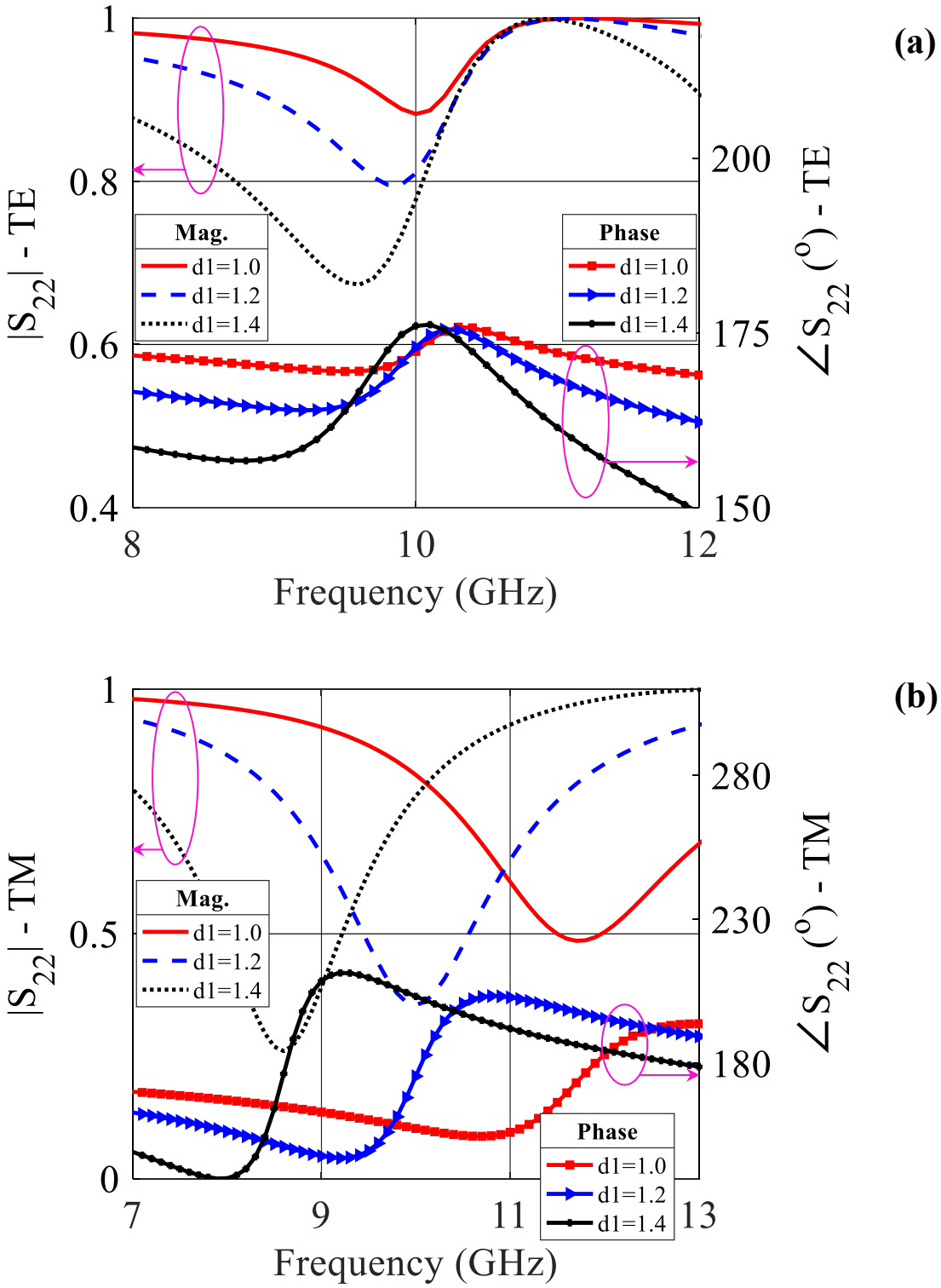

Fig. 4. 4. Dependence of substrate reflection on variation in the aperture size (*r1 = 1 mm*). (a) TE polarization. (b) TM polarization.

To demonstrate the effect of changing the aperture size, we look at the case when r_1 = 1 mm and d_1 is varied from 1.0 mm to 1.4 mm. The results of this investigation are displayed in Fig. 4.4. In Fig.

4.4 (a), the TE-polarized case shows that increasing the aperture size reduces the resonance frequency by less than 1 GHz while reducing the $|S_{22}|$ from 0.9 to 0.7 and making the $\angle S_{22}$ steeper. For the TM-polarized case in Fig. 4.4 (b), increasing the aperture size reduces the resonance frequency by about 2.5 GHz while at the same time reducing $|S_{22}|$ from 0.5 to 0.35 and making the $\angle S_{22}$ steeper.

From the above studies, the following can be deduced. In general, the TE curves have higher reflection magnitudes which suggest a higher directivity FPA according to (4.2). The positive reflection phase region occurs over a narrower frequency band which may lead to a narrowband FPA. Nevertheless, by changing the patch and aperture sizes, the resonance frequencies and the reflection magnitudes and phases can be controlled almost independently. This flexibility can give rise to more tailored designs.

For the TM curves on the other hand, the reflection magnitudes are lower which suggest a lower directivity FPA. Furthermore, the positive reflection phase region occurs over a wider frequency band which may lead to a more wideband FPA. However, it is required that the condition $r_1 \leq d_1$ should be fulfilled for stable operation. In addition, changing the aperture size changes the resonance frequency, $|S_{22}|$, and $\angle S_{22}$ simultaneously by a large margin. These concurrent changes on several parameters makes design for a given set of requirements quite challenging. For this reason, throughout the rest of this Thesis, we will focus on the TE-polarized scenarios.

4.3.1.2 Improved design - dual resonance

A candidate design is chosen from one of the TE cases of the former designs for further investigation and improvement using r1 = 1.0 mm and d1 = 1.2 mm. The magnitude and phase curves for this design are shown in Fig. 4.5. The TM polarized case is included here only for completeness. The |S11| and |S22| in Fig. 4.5 (a) are equal with a value of 0.79. In Fig. 4.5 (b), the reflection phase from the PMS side is zero around the design frequency thus it acts as an AMC in this region. This is significant because it will lead to a very low profile antenna if a dual superstrate is to be employed to further increase the bandwidth. Looking from the AMS side, the reflection phase follows the ideal phase line quite well.

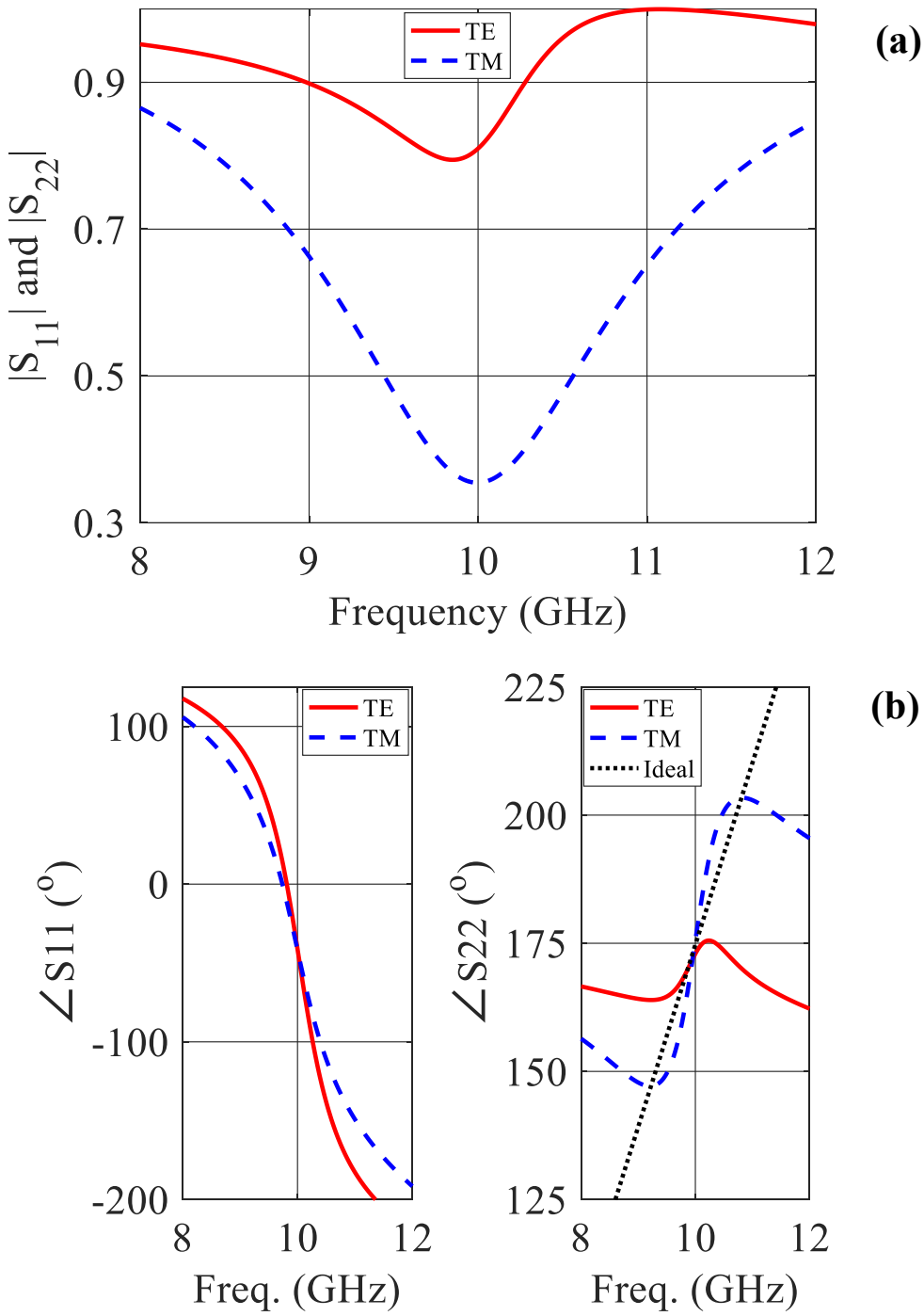

Fig. 4. 5. S-parameters of candidate single-resonance design. (a) Magnitude. (b) Phase.

The multiple resonances in the superstrate can be widely separated in frequency. In order to bring them closer together, the superstrate thickness is increased from 62 mil (1.5748 mm) to 120 mil (3.048 mm) as shown in Fig. 4.6. For t_{sup} = 3.048 mm, two resonances occur at 9.0 GHz and 14.4 GHz

with |S22| > 0.8 at both frequencies. The phase gradients are also identical at these two resonance frequencies. A more in-depth analysis of the multi-resonant behavior of the superstrate is given in part B of this section. The estimated directivity bandwidth (DBW) and the resonant height (calculated from (4.1) above) of this design is computed to be 46% and 16.16 mm respectively. If operation at lower frequencies is desired, the value of ε_r can be increased to lower the resonance frequencies with minimal change to $|S_{22}|$, and $\angle S_{22}$.

The design procedures for TE and TM polarized cases just discussed are summarized as follows:

a) TE-polarization

1. Design for a given frequency (optimization on g_1, g_2, g_3, r_1, and d_1).
2. Keep d_1 fixed and increase r_1 to reduce f_0 ($|S_{11}|$ and $\angle S_{11}$ remains unchanged)
3. Choose best r_1 and increase d_1 (minor decrease in f_0. Decrease in $|S_{11}|$ and increase in $\angle S_{11}$).
4. Increase t_{sup} to make multi-resonant.

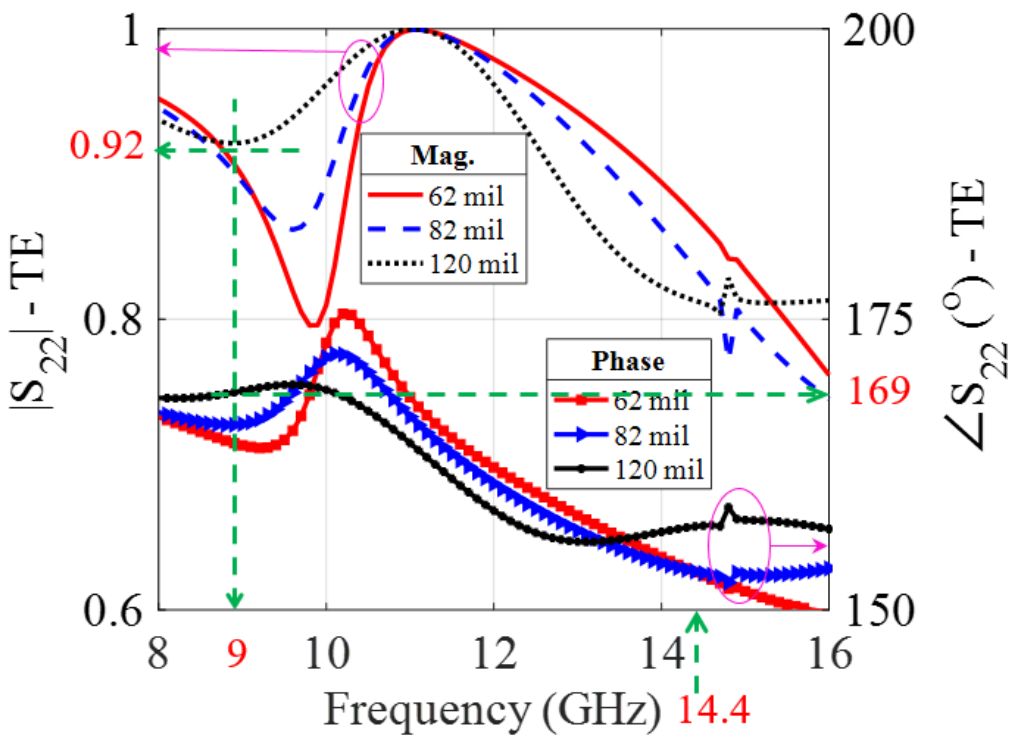

Fig. 4. 6. Parametric study on the substrate thickness of the candidate design. For H_{sup1} = *120 mil (= 3.048 mm)*, f_{L1} = *9 GHz*, λ_{L1} = *33.33 mm*, and $L_x = L_y = 0.144\ \lambda_{L1}$.

5. Increase ε_r to move resonances to lower frequencies if desired.

b) TM-polarization

1. Make sure $r_1 \leq d_1$
2. Design for a given frequency (optimization on g_1, g_2, g_3, r_1, and d_1).
3. Keep d_1 fixed and increase r_1 to reduce f_0 ($|S_{11}|$ increases and $\angle S_{11}$ also increases)
4. Choose best r_1 and increase d_1 (f_0 decreases, $|S_{11}|$ decreases, and $\angle S_{11}$ increases)
5. Follow steps 4 and 5 from TE-polarization

4.3.2 Equivalent Circuit

To obtain an insight into the inner workings of the superstrate, its equivalent circuit was devised as shown in Fig. 4.7. The superstrate is represented by three cascaded transmission line sections terminated by the load impedance, Z_{air}, where Z_{air} is the wave impedance of free space. This can be analyzed with the aid of a Smith chart. The AMS, dielectric, and PMS layers are represented by the characteristic impedances Z_{ams}, Z_d and Z_{pms} respectively. The thickness of the AMS and PMS layers is 17 μm and that of the dielectric is 3.048 mm.

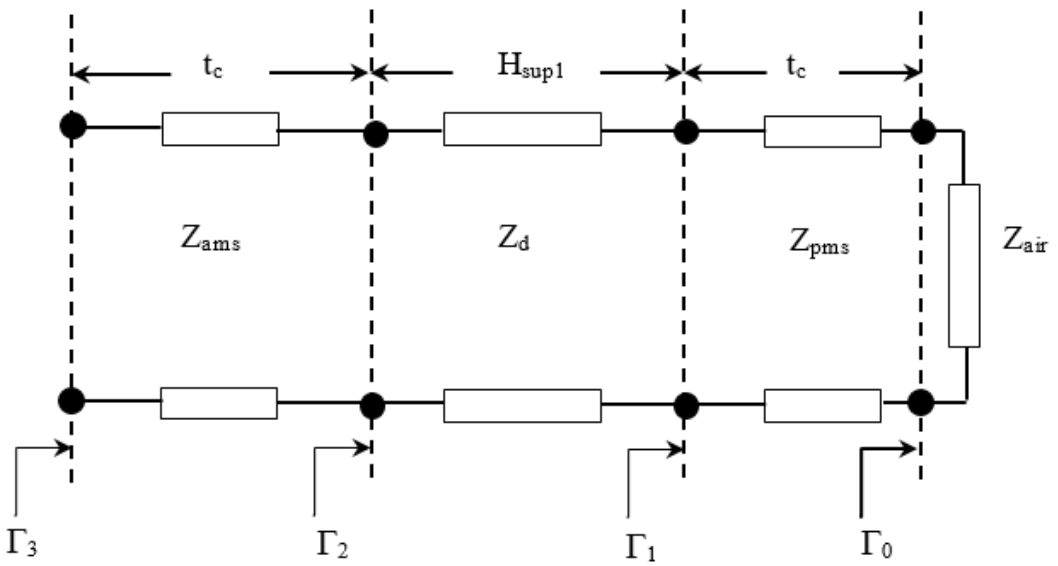

Fig. 4. 7. The superstrate equivalent circuit showing the various impedances and reflection coefficients. The thickness of the AMS and PMS layers, $t_c = 17\ \mu m$. $H_{sup1} = 3.048\ mm$.

The reflection coefficients Γ_0, Γ_1, Γ_2, and Γ_3 at the four interfaces shown in Fig. 4.7 are plotted on the admittance Smith chart in Fig. 4.8. The admittance chart, normalized to Z_{air}, is employed here because of the parallel nature of the various layers of the superstrate structure. Γ_0 falls at the center of the smith chart as it corresponds to the reference impedance value. The loci of all the curves in Fig. 4.8 move in a clockwise direction as the frequency changes from 8 GHz to 16 GHz. Moving to the left of the air region in Fig. 4.7, the interface between the PMS layer and the dielectric, Γ_0 is transformed to produce the Γ_1 curve. The Γ_1 curve travels along the unit conductance circle and intersects the real axis at the point M_1 to produce a reflection resonance (total reflection) at 13.9 GHz. The magnitude and phase of this reflection resonance is shown more clearly in Fig. 4.9 (a) and 4.9 (b) respectively. Fig. 4.9 (b) shows that at this stage, the reflection phase is negative and decreases with frequency.

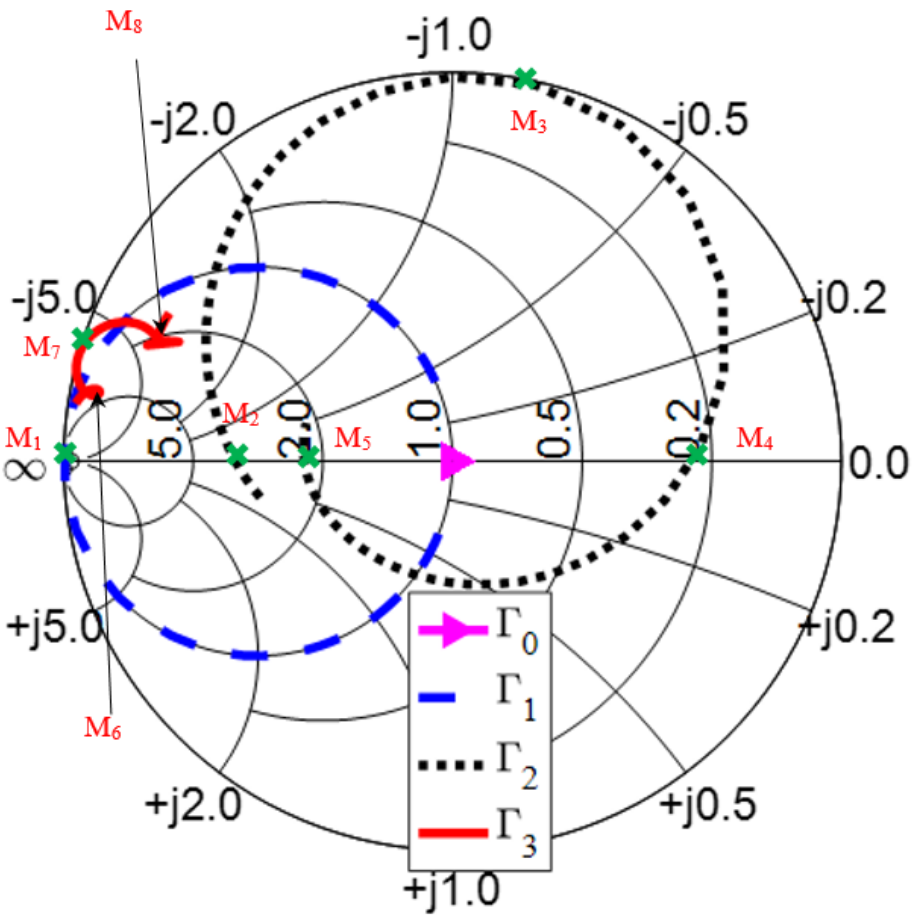

Fig. 4. 8. Admittance Smith chart plot showing the locus of Γ at the four interfaces of the dual-resonant superstrate.

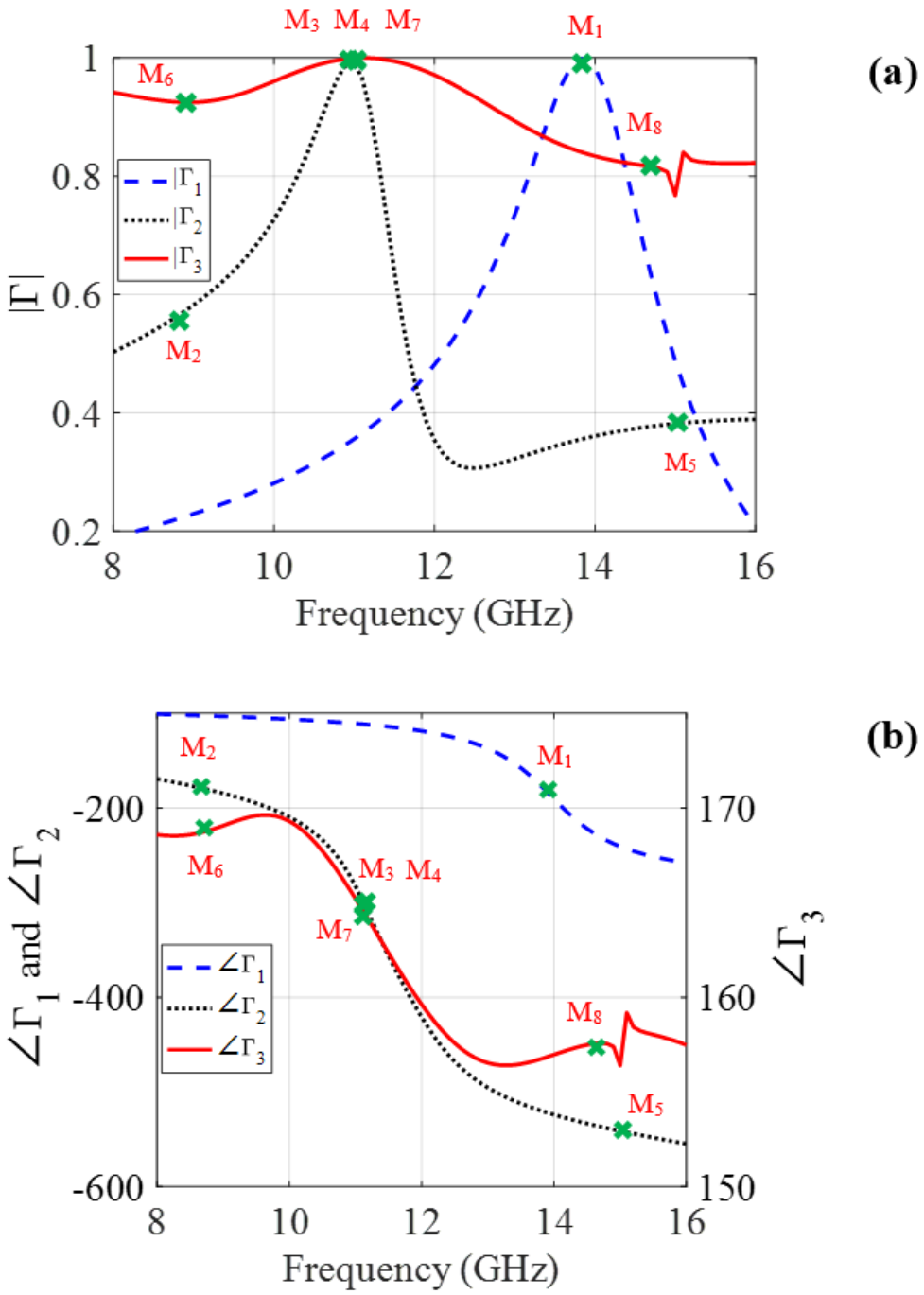

Fig. 4. 9. Reflection coefficient at three interfaces of the dual resonance design showing marker locations. (a) Magnitude. (b) Phase.

By adding the dielectric layer to the PMS layer, the Γ_1 curve on the Smith chart is transformed into the Γ_2 curve and the reflection resonance point moves to M_3 at a lower frequency of 11 GHz. In addition, Γ_2 intersects the real axis at three additional points, M_2 (8.8 GHz), M_4 (11.5 GHz), and M_5 (15.1 GHz)

and the reflection phase of the Γ_2 curve remains negative and decreases with frequency. Finally, the addition of the AMS layer transforms the Γ_2 curve to the Γ_3 curve. At the same time, point M_2 is transformed to point M_6 (9 GHz) and point M_5 is transformed to point M_8 (14.4 GHz) both with positive reflection phases and increasing with frequency as shown in Figs. 4.8 and 4.9. The reflection resonance point at M_4 gets transformed to the point M_7 (11.3 GHz). Just beyond the second resonance frequency at M_8 as shown in Figs. 4.8 and 4.9, there is a spike due to the addition of the AMS layer. The main function of the AMS layer is to transform the reflection phases at M_2 and M_5 into positive values that increase with frequency.

TABLE 4. 1 - Detailed Marker Information

Markers	***Freq. (GHz)***	***Angle*** (^{o})	***Mag.***	***Z = R + jX*** (Ω)	***Y = G + jB*** (Ω^{-1})
M1	13.90	176.57	0.99	0.00 + 0.03j	1.03 - 33.62j
M2	8.80	178.89	0.56	0.28 + 0.01j	3.58 - 0.11j
M3	11.00	77.50	0.99	0.01 + 1.25j	0.01 - 0.80j
M4	11.50	3.54	0.64	4.46 + 0.02j	0.22 - 0.00j
M5	15.10	177.48	0.38	0.45 + 0.02j	2.24 - 0.09j
M6	9.00	169.06	0.92	0.04 + 0.10j	3.69 - 8.94j
M7	11.30	163.49	0.99	0.00 + 0.15j	0.04 - 6.89j
M8	14.40	157.55	0.81	0.10 + 0.20j	2.11 - 3.98j

Table 4.1 summarizes the magnitude and phase of the reflection coefficient at markers M_1 – M_8 and their corresponding frequency, impedance, and admittance values. The same approach is used in the next section on a truncated version of the infinite superstrate described here to construct a wideband low profile FPA.

4.4 Wideband Multi-resonant FPA Design

Following the design and analysis of the multi-resonant superstrate unit cell above, two FPA designs focused on improving the 1-dB and 3-dB GBWs are presented in this section.

4.4.1 Antenna Structure

The proposed wideband FPA is shown in Fig. 4.10. It consists of a superstrate made up of 9 × 9 elements (43.2 mm × 43.2 mm) placed less than half a wavelength above a $D_x \times D_y$ ground plane with a standard WR75 waveguide at its centre. This aperture size was chosen to fulfill the minimum area required for a directivity improvement of 13.8 dB at 9 GHz as computed from (4.2). The maximum directivity

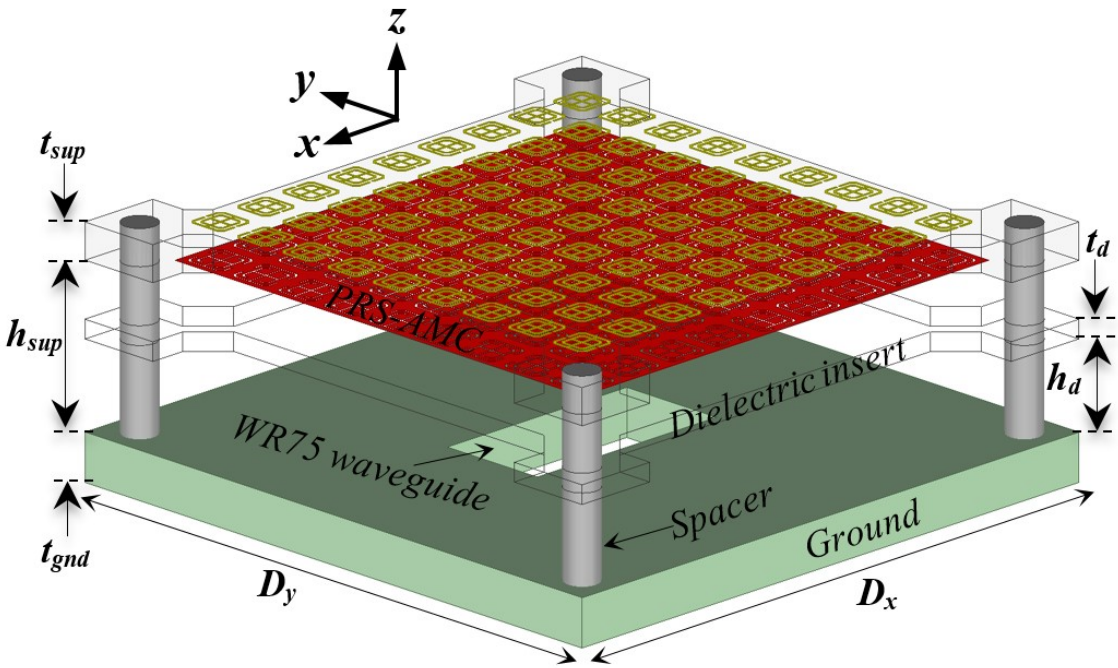

Fig. 4. 10. FPA with a waveguide feed. Both the dielectric insert and the multi-resonant superstrate are made from Rogers RT/Duroid™ 5880 with $\varepsilon_r = 2.2$ and $tan\delta = 0.0009$. WR75 dimensions = *19.05 mm × 9.525 mm*. Teflon spacer radius = *1.5* mm.

obtainable with this aperture at the highest frequency (14.4 GHz) is 17.3 dB. This truncated aperture can be better illuminated with higher aperture efficiency and a reasonably good gain [127]. The total dimension of the antenna is 52.8 mm × 52.8 mm × 16.75 mm. A dielectric substrate is inserted into the Fabry-Perot cavity to reduce the overall antenna height and for greater flexibility in tuning the directivity and impedance matching.Both the dielectric insert and the multi-resonant superstrate are made from Rogers RT/Duroid™ 5880 with $\varepsilon_r = 2.2$ and $\tan\delta = 0.0009$.

4.4.2 Initial FPA Designs

In the unit cell simulations, plane wave incidence was assumed. However, in the finite FPA, oblique incidences also occur which necessitates the adjustment of the previously calculated DBW and resonant heights. The resonance frequencies are also slightly shifted in the finite case. The detailed optimized dimensions for the various designs are given in table 4.2. Dielectric loading was employed in order to reduce the cavity height. Design-1a and 1b are for the cases without and with dielectric loading of the cavity respectively. For these two cases, the simulation settings made use of symmetry planes along the

x-z and *y-z* planes to reduce the computational time. In addition, infinitely thin PEC sheets were assumed for the ground plane, PMS layer, and AMS layer. The Teflon spacers and the extra superstrate dielectric holding the spacers were also not included in the simulations.

TABLE 4. 2 - FPA Dimensions (mm)

Design	D_x	D_y	t_{gnd}	h_{sup}	t_{sup}
1a – initial (No insert)	50.5	50.5	0.0	16.0	3.048
1b – initial (with Insert)	50.5	50.5	0.0	13.7	3.048
2a – final 1-dB (with Insert)	52.8	52.8	4.0	13.7	3.048
2b – final 3-dB (with Insert)	52.8	52.8	4.0	13.7	3.048
Design	l_{sup}	h_d	t_d	l_d	r_s
1a – initial (No Insert)	43.2	-	-	-	-
1b – initial (with Insert)	43.2	5.1	1.5748	50.5	-
2a – final 1-dB (with Insert)	43.2	4.0	2.032	41.0	1.5
2b – final 3-dB (with Insert)	43.2	7.4	1.5748	41.0	1.5

l_d = length of dielectric insert; l_{sup} = length of superstrate; r_s = spacer radius.

The DBW and return loss of the dielectric loaded and unloaded FPA is shown in Fig. 4.11. Using the dielectric insert, the DBW variation is improved across the band albeit with a slight deterioration of the low frequency impedance matching. Furthermore, the FPAs height is reduced from 16.0 mm to 13.7 mm as a result of the dielectric loading.

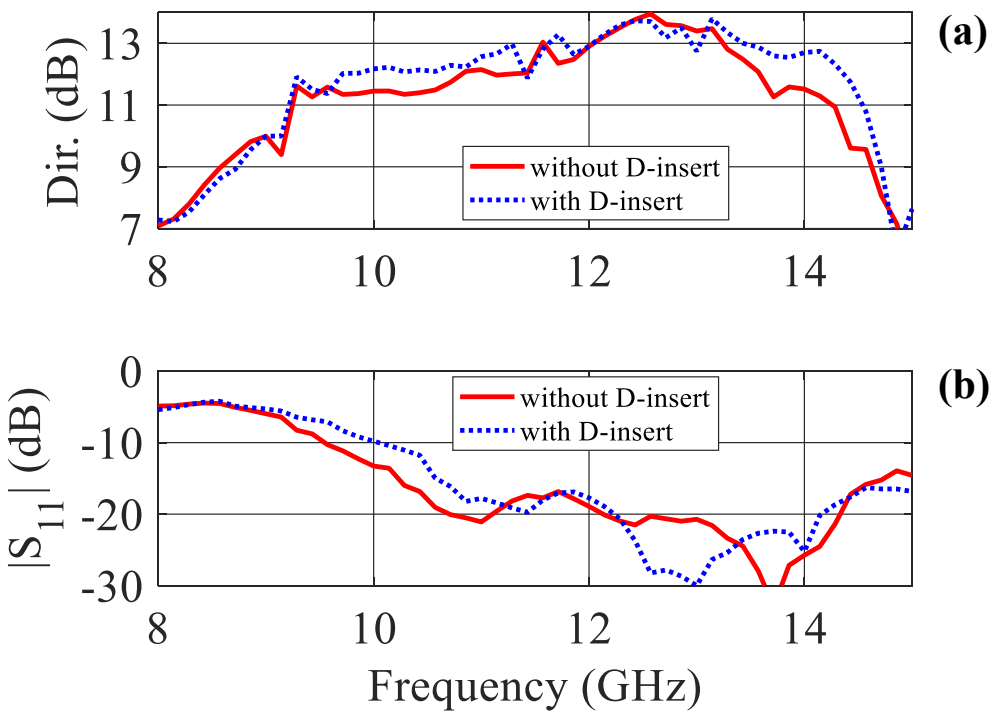

Fig. 4. 11. Initial FPA results with and without the dielectric insert. (a) Directivity (b) Reflection coefficient.

4.4.3 Final FPA Designs

We now consider two scenarios, namely design 2a which is optimized for 1-dB GBW and design 2b which is optimized for 3-dB GBW. The structure of both antennas is displayed in Fig. 4.10 and was simulated as is taking into account all material losses. Design-2a has a 2.032 mm dielectric insert at a height of 4.0 mm, while design-2b has a 1.5748 mm dielectric insert at a height of 7.4 mm. The DBW for design-2a is shown in Fig. 4.12 (a). Its 1-dB DBW is 25.44% (9.95 GHz – 12.85 GHz) and its 3-dB DBW is 43.60% (9.22 GHz – 14.36 GHz) with a peak gain of 13.7 dB at 11.6 GHz. For design-2b, the 3-dB DBW as shown in Fig. 4.12 (b) is 42.80% (9.32 GHz – 14.40 GHz) with a peak gain of 14.6 dB at 12.70 GHz. The directivity of the source antenna is also shown in Fig. 4.12 to highlight the directivity increase as a result of the Fabry-Perot cavity created by the superstrate. The cavity height, h_{sup}, for both designs is kept constant at 13.7 mm with a good impedance match across most of the band as shown in Fig. 4.14.

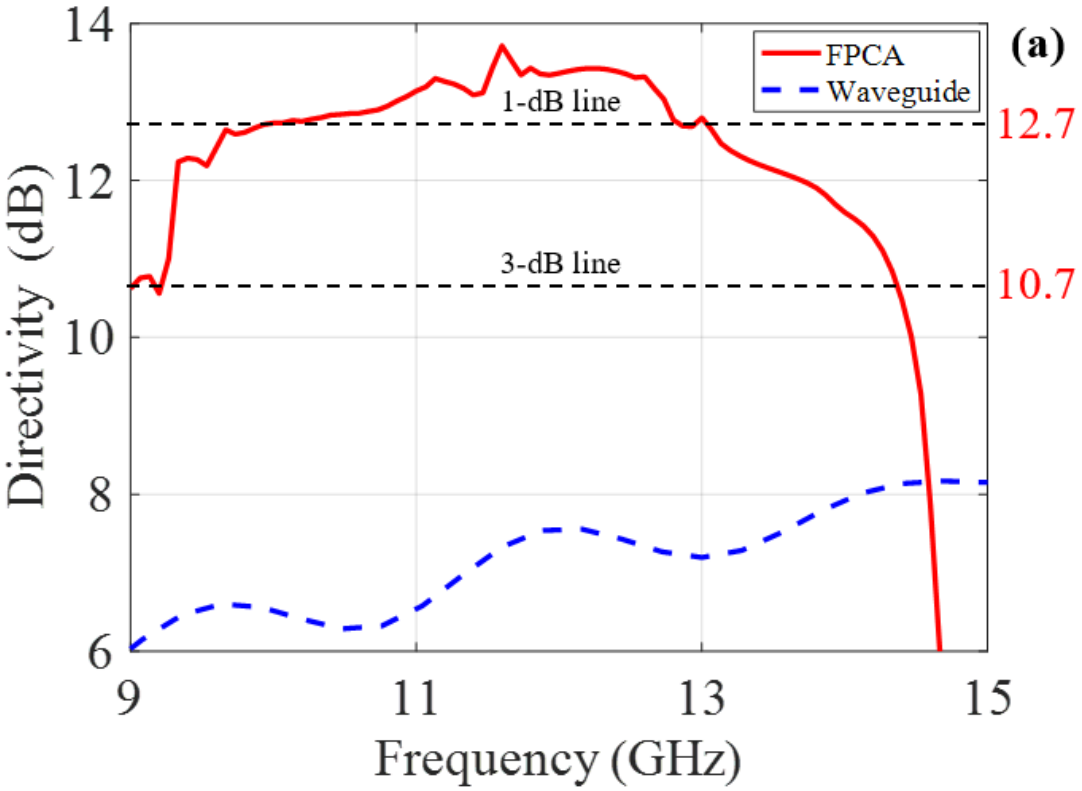

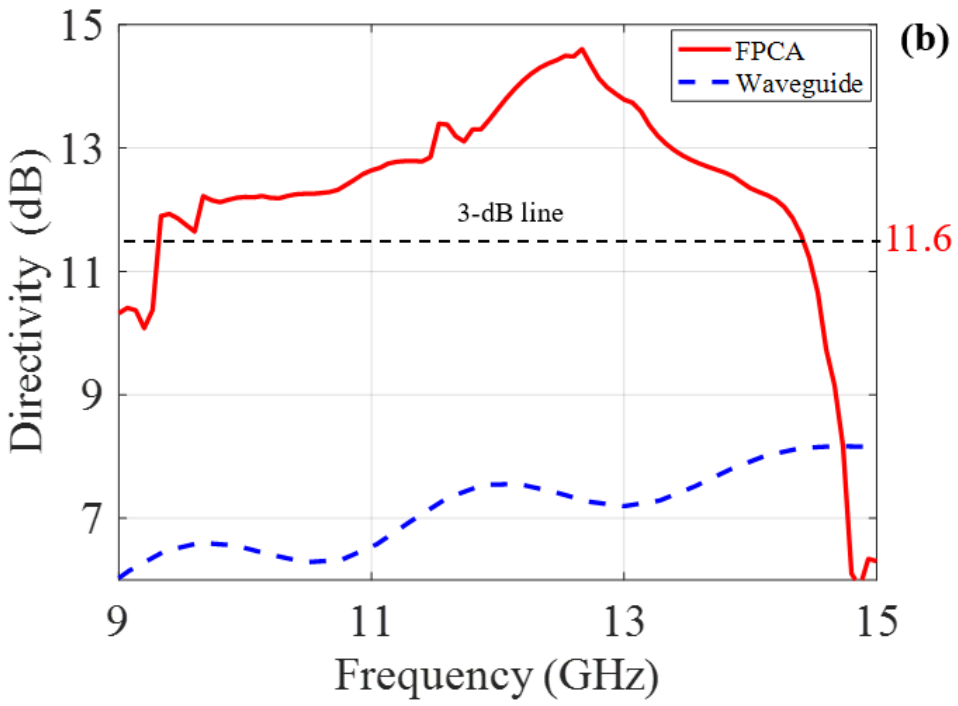

Fig. 4. 12. FPA and the waveguide directivity. (a) Design-2a. (b) Design-2b.

4.5 Measurement Results

The two FPA designs analysed in the previous section were fabricated and measured. The fabricated prototype is shown in Fig. 4.13. The simulated and measured results of these two antennas are given in this section and their performance is compared to similar designs given in the literature. A WR75 waveguide-to-coax transition and a straight WR75 waveguide section was used to connect the FPAs to the test equipment.

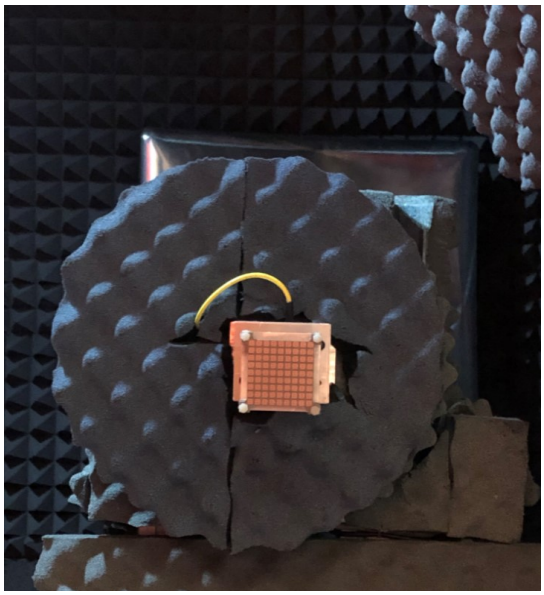

(a)

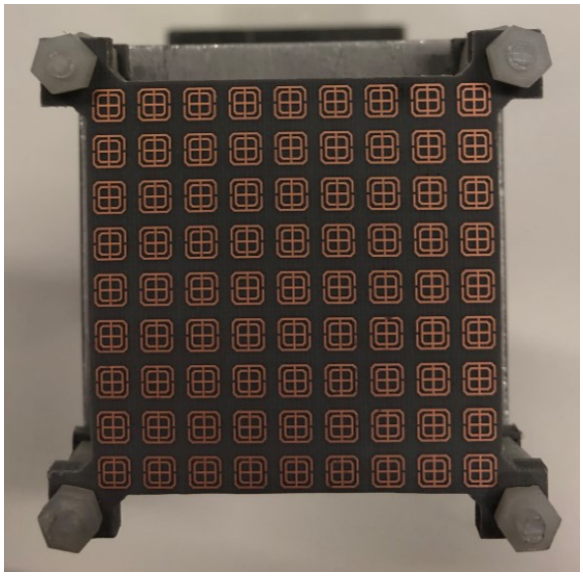

(b)

Fig. 4. 13. FPA prototype. (a) Testing in mini-compact range. (b) Top view of fabricated antenna.

4.5.1 Matching Performance

The input reflection coefficient was measured using a Keysight Technologies N5225A PNA. The simulated and measured input reflection coefficients of the two antennas are shown in Fig. 4.14. The measured reflection coefficient of the waveguide with no superstrate present is also shown in Fig. 4.14 to demonstrate the effect of the superstrate on the antenna matching. The measured and simulation results agree quite well with each other for both antennas remaining below -10 dB over the whole band. The discrepancies towards the high frequency end is attributed to the manufacturing tolerances in fabricating the WR75 waveguide and the positioning errors of the superstrate above the ground plane.

4.5.2 Radiation Performance

The radiation performance of the antennas was measured in a microwave vision group (MVG) Mini-Compact Range. The simulated and measured realized gains for design-2a and 2b are shown in Fig. 4.15 (a) and 15 (b) respectively. There is excellent agreement between the results for both designs although there is a 0.3 dB reduction in the measured peak realized gains. For design-2a, the measured 1-dB GBW is 24.0% (10.4 GHz – 13.2 GHz) and its 3-dB GBW is 42.1% (9.3 GHz – 14.3 GHz) with a peak gain

of 13.4 dB at 11.5 GHz. For design-2b, the measured 3-dB GBW is 40.0% (9.6 GHz – 14.4 GHz) with a peak gain of 14.3 dB at 12.70 GHz.

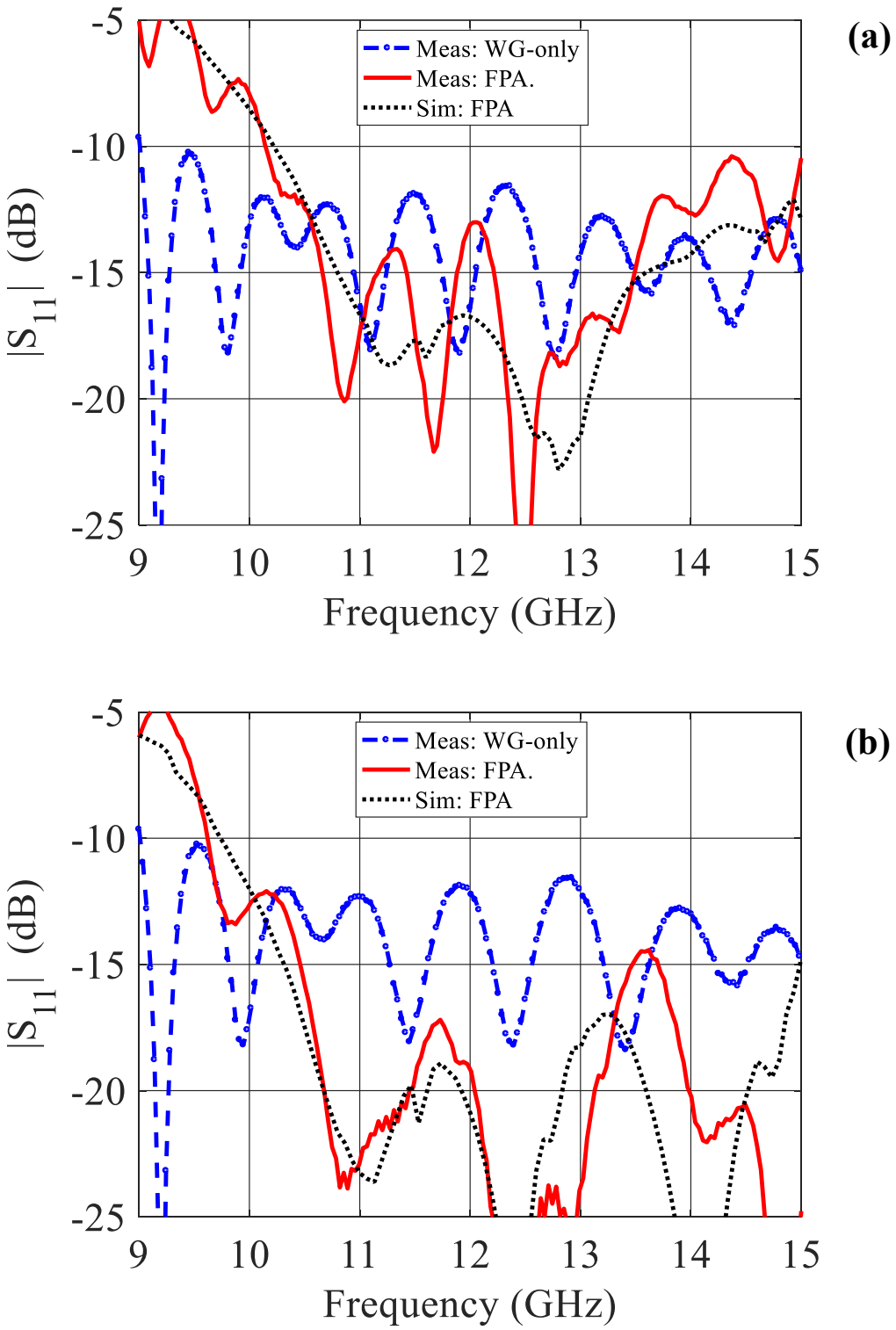

Fig. 4. 14. FPA and the waveguide reflection coefficients. (a) Design-2a. (b) Design-2b.

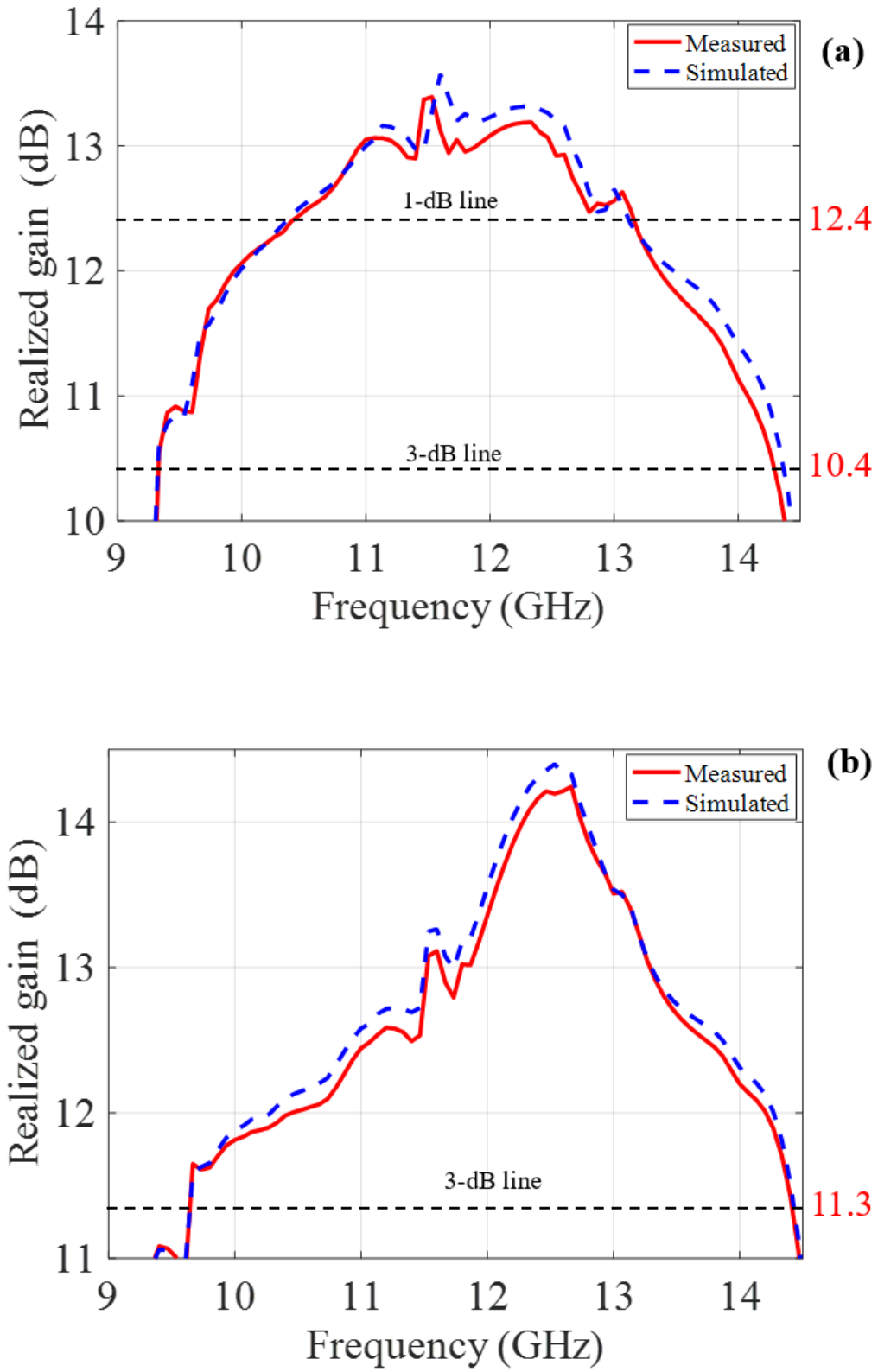

Fig. 4. 15. Simulated and measured realized gains. (a) Design-2a. (b) Design-2b.

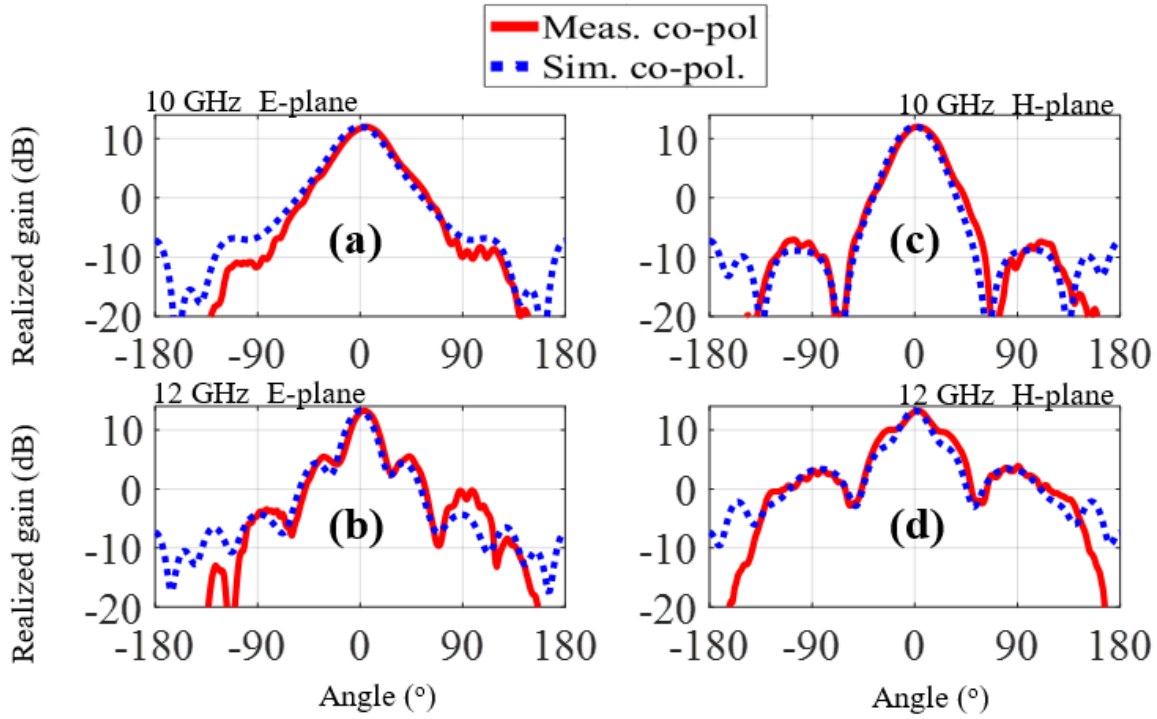

Fig. 4. 16. Simulated and measured radiation patterns for design-2a. (a) 10 GHz, E-plane. (b) 12 GHz, E-plane. (c) 10 GHz, H-plane. (d) 12 GHz, H-plane. The simulated and measured cross-polarization patterns are all below -30 dB.

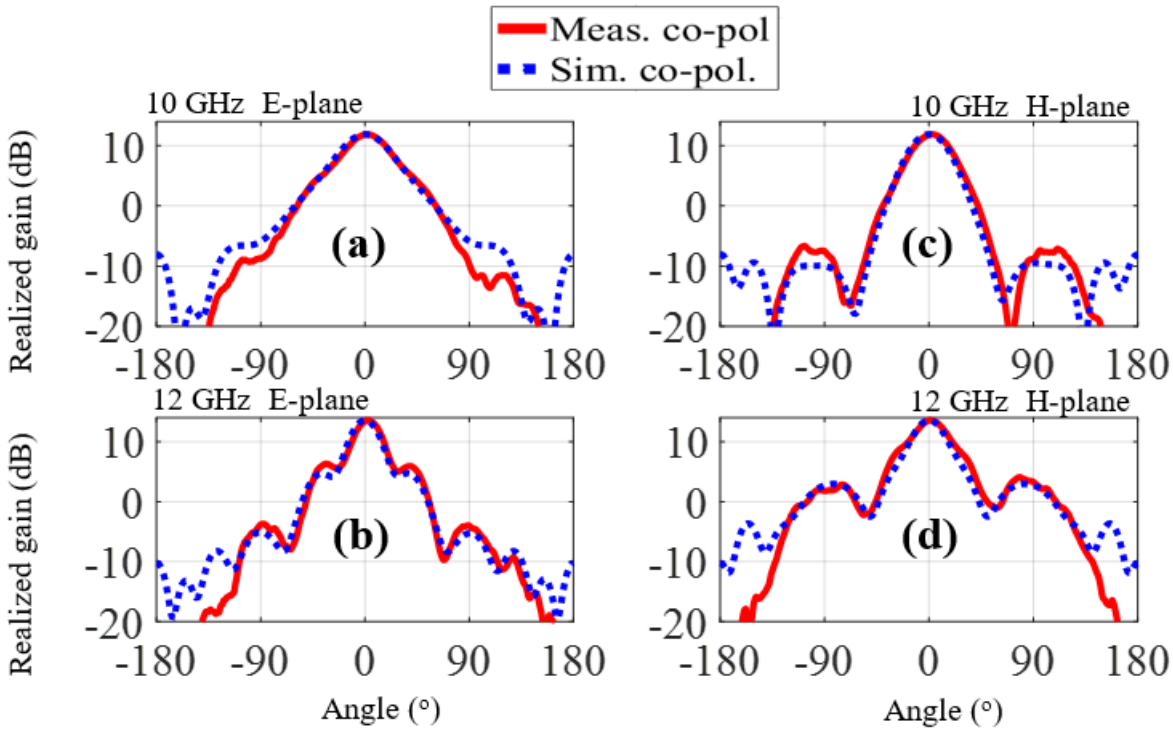

Fig. 4. 17. Simulated and measured radiation patterns for design-2b. (a) 10 GHz, E-plane. (b) 12 GHz, E-plane. (c) 10 GHz, H-plane. (d) 12 GHz, H-plane. The simulated and measured cross-polarization patterns are all below -30 dB.

The simulated and measured E- and H-plane radiation patterns are shown in Fig. 4.16 for design-2a and in Fig. 4.17 for design-2b. It can be seen that the simulated and measured patterns agree very well. The increase in side lobe levels for the 12 GHz patterns is attributed to the edge effects due to the small superstrate size and the appearance of higher order modes as the frequency increases. The simulated and measured E- and H-plane cross-polarizations are below -30 dB so do not appear in Figs.4.16 and 4.17.

A summary of the performance metrics of the two FPAs are shown in table 4.3. Design 2a has a 0.9 dB lower measured peak gain and a 2% higher 3-dB measured gain bandwidth compared to design 2b. Because of the lower peak gain of design 2a, it has a much wider 1-dB measured gain bandwidth of 24%.

TABLE 4. 3 - FPA Performance Parameters

Parameters	***Design-2a***		***Design-2b***
Simulated DBW	1-dB	25.4%	-
	3-dB	43.6%	42.8%
Simulated Peak directivity	13.7 dB @ 11.6 GHz		14.6 dB @ 12.7 GHz
Measured realized GBW	1-dB	24.0%	-
	3-dB	42.0%	40.0%
Measured peak realized gain	13.4 dB @ 11.5 GHz		14.3 dB @ 12.7 GHz
Aperture efficiency	64% @ 11.5 GHz		64% @ 12.7 GHz
Aperture size	$1.7\ \lambda_C \times 1.7\ \lambda_C$ (43.2 mm × 43.2 mm) $1.3\ \lambda_L \times 1.3\ \lambda_L$ (43.2 mm × 43.2 mm)		
Total antenna volume, V	$2.1\ \lambda_C \times 2.1\ \lambda_C \times 0.66\ \lambda_C$ $1.6\ \lambda_L \times 1.6\ \lambda_L \times 0.5\ \lambda_L$		
D_{max} @ f_H	17.3 dB		17.3 dB
DBWP @ f_C	1022.1		1234.4
DBWP/V @ f_C	359.0		433.6
GBWP @ f_C	918.9		1076.6
GBWP/V @ f_C	322.8		378.2

f_L = 9.2 GHz; f_C = 11.8 GHz; f_H = 14.4 GHz; DBWP (GBWP) = directivity (gain) bandwidth product; D_{max} = maximum directivity.

4.5.3 Comparison and Discussion

To make comparisons with previous designs, an additional metric is introduced here to account for the volume of the antenna in addition to its directivity or gain bandwidth product (i.e. DBWP or GBWP). This metric is the ratio of each BWP and the volume here designated as the DBWP/V or GBWP/V. The DBWP/V and GBWP/V are calculated based on the largest antenna dimensions at the central frequency.

A high value of DBWP or GBWP is desireable. The antenna height, *h*, is measured from the ground plane to the very top of the superstrate. Considering design 2b, its GBWP/V is higher than all the reported designs in table 4.4 except [129]. However, in [129], three layers of superstrate were required to achieve the stated performance with an aperture efficiency of only 38.4% as compared to the high value of 64% reported in this work.

TABLE 4. 4 – FPAs Performance Comparison

Ref.	***G_{max}***	***3dB-BW***	***V = A*h***	***GBWP***	***GBWP/V***	***Aper. eff.***
[76]	16.0	23.0	7.56*0.65	915.6	216.2	41.9
[79]	16.3	10.7	13.54*0.68	456.4	49.4	25.1
[80]	13.8	28.0	5.76*0.53	671.7	233.2	33.1
[81]	14.0	27.0	5.65*1.40	678.2	85.7	35.4
[126]	17.7	24.7	24.6*1.17	1454.4	50.53	19.0
[129]	14.2	86.3	4.16*1.24	2269.9	439.9	38.4
This work	**14.3**	**40.0**	**4.31*0.66**	**1076.6**	**378.5**	**64.0**

Antenna volume, $V = A*h = area * height$.

4.6 Chapter Conclusion

A new method of improving the bandwidth of low profile FPAs using multi-resonant metasurface based superstrates has been introduced and verified in this Chapter. Two prototypes focused on improving the 1-dB and 3-dB gain bandwidths have been designed, analyzed, fabricated and tested. The first fabricated prototype achieved a measured 1-dB GBW of 24.0% and a 3-dB GBW of 42.1% with a peak gain of 13.4 dB. The second fabricated prototype achieved a measured 3-dB GBW of 40.0% with a peak gain of 14.3 dB. A high GBWP/V value was obtained for both designs coupled with superior aperture efficiency (64%) compared to similarly sized antennas in the literature. Overall the measured performance agrees very well with simulations. Finally, potential applications of this improved antenna include satellite communication where space is a premium and high directivity is desired. Because of the small physical footprint of the antenna, it could be used as an element in a sparse antenna array to further increase the directivity.

Chapter 5 – Conclusions and Future Work

The objectives of this Thesis as stated in Chapter 1 are to fully address the major Challenges facing two kinds of antennas to enable multifunctional operation. Also in Chapter 1, the main motivation and significance of the work is clearly articulated. A thorough literature review is carried out on Tightly coupled antenna arrays (TCAA) and Fabry-Perot antennas (FPA) to identify the major obstacles to multifunctional antenna design and current solutions. In the first type of antenna, the so called tightly coupled antenna array, the two major challenges are the improvement of their wide angle impedance matching when scanning and the reduction of the complexity and profile of their feed networks. Both of these items are addressed comprehensively in Chapters 2 and 3 respectively. In the second type of antenna, the Fabry-Perot antenna, the biggest problem is to do with their inherently narrow gain bandwidth. A novel FPA bandwidth improvement method is introduced in Chapter 4.

A wideband single sided (SS) metasurface based wide angle impedance matching (MS-WAIM) superstrate was designed and experimentally validated in Chapter 2 to solve the scan loss problem in phased array antennas and TCAAs in particular. Its effective material parameters were extracted to show the near zero refractive index (NZI) behavior which led to the significant improvement in scan behavior. The optimized SS MS-WAIM was used as a superstrate over a TCAA of simple printed dipoles to reduce the impedance mismatch of the system to its source when the array is scanning whilst at the same time reducing the weight and profile of the antenna system.

An improved double sided (DS) MS-WAIM superstrate and an integrated TCAA feed network was reported in Chapter 3. A theoretical background on the TCAA and the feed network is also provided to aid understanding and improve the array performance. The proposed feed network is composed of an impedance transformer and a balun section, both of which were constructed from Klopfenstein tapered microstrip lines. The Klopfeinstein equations were solved in MATLAB and the results exported to HFSS to taper both the ground plane and microstrip line but at differeing rates. A 10 x 10 TCAA was designed, fabricated, and tested making use of the new DS MS-WAIM and feed network. A set of design guidelines were also established for designing arrays with the highest figures of merit that approach the

fundamental limits. For the optimum design, a bandwidth of 5.5:1 was achieved while scanning to 80° along the E-plane and 55° along the H-plane for an active VSWR value of 3.1.

In Chapter 4, a new method of improving the bandwidth of low profile FPAs using multi-resonant metasurface based superstrates was introduced and verified. In our approach, only a single superstrate is required with multiple closely spaced resonances which overlap to produce a wide gain bandwidth. The FPA aperture is kept small so it is well illuminated by the source antenna. Due to the small foot print of this FPA, it can be easily employed as an element in an active array setting without the introduction of grating lobes. At the same time, the number of active elements will be significantly reduced compared to the dense TCAAs leading to substantial cost reductions. Two designed and tested prototypes achieved > 40% 3-dB bandwidth and 64% aperture efficiency.

Future improvements to the TCAA can be achieved by extending the H-plane scan range, increasing the array size for better radiation and matching characteristics, implementing a dual polarization setup, and using a stripline or substrate integrated waveguide (SIW) feed to reduce unwanted feed coupling. Adopting a multi-layered superstrate will enhance the scanning capability even further. The high permittivity value of the array substrate also introduce some array guided surface waves as evident in the increase in the active measured VSWR in Fig. 3.15. A substrate with a lower permittivity value or using an all metal antenna will alleviate this problem. This wideband, wide scanning, array with an integrated low profile feed can serve as a multifunctional phased array for various radar, communication, and sensing applications.

TCAAs are very dense arrays which means substantially higher costs. An array of the small footprint FPA introduced in Chapter 4 is worth exploring. The elements can be placed more than a wavelength apart without significant performance degradation. This can lower the number of active elements and in turn the cost of antenna arrays significantly.

Some open directions for further research may include:

- Exploration of the effects of the high levels of coupling between elements when implementing simultaneous transmit and receive (STAR) systems;
- Analogue, digital, or hybrid beam forming techniques as applied to TCAAs;
- Interleaving a mixture of TCAAs and other conventional arrays to cover an even wider bandwidths;
- Realisation of multifunctional capabilities using TCAAs;
- The investigation of small sub-arrays, say 2x2, in TCAAs to reduce the number of Tx/Rx modules and hence the overall cost of the system; and
- Further exploration of the multi-resonant superstrate in FPAs with more than two resonances to achieve extremely wide bandwidths.

Bibliography

[1] G. C. Tavik, C. L. Hilterbrick, J. B. Evins, J. J. Alter, J. G. Crnkovich, J.W. De Graaf, W. Habicht, G. P. Hrin, S. A. Lessin, D. C. Wu, and S. M. Hagewood, "The advanced multifunction RF concept," *IEEE Trans. Microwave Theory Techn.*, vol. 53, no. 3, pp. 1009-1020, Mar. 2005.

[2] P. E. Dewdney, P. J. Hall, R. T. Schilizzi and T. J. L. W. Lazio, "The Square Kilometre Array," in *Proc. IEEE*, vol. 97, no. 8, pp. 1482-1496, Aug. 2009.

[3] Military Embedded Systems. (2019) "Next-gen military radar system design innovations". [Online]. Available: http://mil-embedded.com/articles/next-gen-system-design-innovations.

[4] P. S. Hall, P. Gardner, and A. Faraone, "Antenna Requirements for Software Defined and Cognitive Radios," in *Proc. IEEE*, vol. 100, no. 7, pp. 2262-2270, Jul. 2012.

[5] W. F. Croswell, T. Durham, M. Jones, D. Schaubert, P. Friederich, and J. G. Maloney, "Wideband arrays," in *Modern Antenna Handbook*, C.A. Balanis, Ed. New York: Wiley-Interscience, pp. 581-627, 2008.

[6] J. A. Kasemodel, C. C. Chen, and J. L. Volakis, "Wideband Planar Array With Integrated Feed and Matching Network for Wide-Angle Scanning," *IEEE Trans. Antennas Propag.,* vol. 61, no. 9, pp. 4528-4537, Sep. 2013.

[7] D. Cavallo, A. Neto, G. Gerini, A. Micco and V. Galdi, "A 3- to 5-GHz Wideband Array of Connected Dipoles with Low Cross Polarization and Wide-Scan Capability," *IEEE Trans. Antennas Propag.,* vol. 61, no. 3, pp. 1148-1154, Mar. 2013.

[8] R. C. Hansen, "Linear Connected Arrays," *IEEE Antennas Wireless Propag. Lett.*, vol. 3 pp. 154 156, 2004.

[9] B. Munk, *et al.,* "A low-profile broadband phased array antenna," in *Proc. IEEE Antennas Propag. Soc. Int. Symp. (APS'03)*, Columbus, OH, USA, Jun. 2003, vol. 2, pp. 448–451.

[10] J. P. Doane, K. Sertel, and J. L. Volakis, "A Wideband, Wide Scanning Tightly Coupled Dipole Array With Integrated Balun (TCDA-IB)," *IEEE Trans. Antennas Propag.,* vol. 61, no. 9, pp. 4538-4548, Sep. 2013.

[11] E. G. Magill and H. A. Wheeler, "Wide-angle impedance matching of a planar array antenna by a dielectric sheet," *IEEE Trans. Antennas Propag.*, vol. 14, no. 1, pp. 49–53, Jan. 1966.

[12] S. Lee and R. Mittra, "Radiation from dielectric-loaded arrays of parallel-plate waveguides," *IEEE Trans. Antennas Propag.*, vol. 16, no. 5, pp. 513-519, Sep. 1968.

[13] G. V. Trentini, "Partially reflecting sheet arrays," *IRE Trans. Antennas Propag.*, vol. 4, no. 4, pp. 666–671, Oct. 1956.

[14] J. J. Lee, "Ultra wideband arrays," in *Antenna Engineering Handbook*, 4th ed., J. L. Volakis, Ed. McGraw Hill Professional, 2007.

[15] K. F. Warnick, R. Maaskant, M. V. Ivashina, D. B. Davidson, and B. D. Jeffs, *Phased Arrays for Radio Astronomy, Remote Sensing*, *and Satellite Communications*, Ch. 1, pp. 12-18, Cambridge University Press, Cambridge, UK, 2018.

[16] Australia Telescope National Facility. (2019) "Phased Array Feed Receiver". [Online]. Available: https://www.atnf.csiro.au/projects/askap/index.html.

[17] D. R. DeBoer *et al*., "Australian SKA Pathfinder: A High-Dynamic Range Wide-Field of View Survey Telescope," in *Proc. IEEE*, vol. 97, no. 8, pp. 1507-1521, Aug. 2009.

[18] Australia Telescope National Facility. (2019) "The Australian Square Kilometre Array Pathfinder (ASKAP) Telescope". [Online]. Available: https://www.atnf.csiro.au/projects/askap/index.html.

[19] W. A. van Cappellen and L. Bakker, "APERTIF: Phased array feeds for the westerbork synthesis radio telescope," in *Proc. IEEE Int. Symp. on Phased Array Systems and Technology,* Waltham, MA, 2010, pp. 640-647.

[20] E. de Lera Acedo, A. J. Faulkner, and J. G. B. de Vaate, "SKA low frequency aperture array," in *Proc. United States National Committee of URSI National Radio Science Meeting (USNC-URSI NRSM)*, Boulder, CO, 2016, pp. 1-2.

[21] K. F. Warnick, R. Maaskant, M. V. Ivashina, D. B. Davidson and B. D. Jeffs, "High-Sensitivity Phased Array Receivers for Radio Astronomy," in *Proc. IEEE*, vol. 104, no. 3, pp. 607-622, Mar. 2016.

[22] J. G. B. de Vaate *et al*., "SKA Mid Frequency Aperture arrays: Technology for the ultimate survey machine," in *Proc. URSI General Assembly and Scientific Symposium*, Beijing, 2014, pp. 1-4.

[23] M. de Vos, A. W. Gunst and R. Nijboer, "The LOFAR Telescope: System Architecture and Signal Processing," in *Proc. IEEE*, vol. 97, no. 8, pp. 1431-1437, Aug. 2009.

[24] C. J. Lonsdale *et al*., "The Murchison Widefield Array: Design Overview," in *Proc. IEEE*, vol. 97, no. 8, pp. 1497-1506, Aug. 2009.

[25] G. W. Kant, P. D. Patel, S. J. Wijnholds, M. Ruiter, and E. van der Wal, "EMBRACE: A Multi-Beam 20,000-Element Radio Astronomical Phased Array Antenna Demonstrator," *IEEE Trans. Antennas Propag.*, vol. 59, no. 6, pp. 1990-2003, Jun. 2011.

[26] P. J. Gibson, "The Vivaldi Aerial," *9th European Microwave Conference*, Brighton, UK, 1979, pp. 101-105.

[27] R. W. Kindt, W. R. Pickles, "Ultrawideband all-metal flared-notch array radiator," *IEEE Trans. Antennas Propag*., vol. 58, no. 11, pp. 3568 - 3575, Sept. 2010.

[28] M. N. Vouvakis and D. H. Schaubert, "Vivaldi antenna arrays," in *Frontiers in Antennas: Next Generation Design & Engineering*, F. B. Gross, Ed. McGraw Hill, 2011.

[29] D. T. McGrath, N. Schuneman, T. H. Shively and J. Irion, "Polarization properties of scanning arrays," in *Proc. IEEE Int. Symp. on Phased Array Systems and Technology,* 2003, pp. 295-299.

[30] M.W. Elsallal and J. C. Mather, “An ultra-thin, decade (10:1) bandwidth, modular “BAVA” array with low cross-polarization,” in *Proc. IEEE Int. Symp. Antennas Propag. (APSURSI’11),* July 2011, pp. 1980–1983.

[31] H. A. Wheeler, “The Radiation Resistance of an Antenna in an Infinite Array or Waveguide,” in *Proc. IRE*, vol. 36, pp. 478-488, Apr. 1948.

[32] H. A. Wheeler, “Simple relations derived from a phased-array antenna made of an infinite current sheet,” *IEEE Trans. Antennas Propag.*, vol. 13, no. 4, pp. 506–514, 1965.

[33] D. K. Papantonis and J. L. Volakis, "Dual-Polarized Tightly Coupled Array With Substrate Loading," *IEEE Antennas Wireless Propag. Lett*., vol. 15, pp. 325-328, 2016.

[34] I. Tzanidis, K. Sertel, and J. L. Volakis, "UWB Low-Profile Tightly Coupled Dipole Array With Integrated Balun and Edge Terminations," *IEEE Trans. Antennas Propag.*, vol. 61, no. 6, pp. 3017-3025, Jun 2013.

[35] J. A. Kasemodel, C. C. Chen, and J. L. Volakis, "Broadband planar wide-scan array employing tightly coupled elements and integrated balun," in *Proc. IEEE International Symposium on Phased Array Systems and Technology (ARRAY),* Oct. 2010, pp. 467-472.

[36] W. F. Moulder, K. Sertel, and J. L. Volakis, "Ultrawideband Superstrate-Enhanced Substrate-Loaded Array With Integrated Feed," *IEEE Trans. Antennas Propag.*, vol. 61, no. 11, pp. 5802-5807, Nov. 2013.

[37] E. Irci, K. Sertel, and J. L. Volakis, “An extremely low profile, compact, and broadband tightly coupled patch array,” Radio Sci., 47, RS0M06, doi:10.1029/2011RS004771.

[38] E. Irci, K. Sertel, and J. L. Volakis, "Bandwidth enhancement of low-profile microstrip antennas using tightly coupled patch arrays," in *Proc. Antennas and Propagation Society International Symposium (APSURSI)*, Jul. 2011, pp. 1044-1047.

[39] J. L. Volakis and K. Sertel, “Narrowband and Wideband Metamaterial Antennas Based on Degenerate Band Edge and Magnetic Photonic Crystals,” *Proc. of the IEEE,* vol. 99. No. 10, pp. 1732-1745, Oct. 2011.

[40] I. Tzanidis, K. Sertel, and J. L. Volakis, “Interwoven spiral array (ISPA) with a 10:1 bandwidth on a ground plane,” *IEEE Antennas Wireless Propag. Lett*., vol. 10, pp. 115-118, 2011.

[41] E. O. Farhat, K. Z. Adami, Y. Zhang, A. K. Brown, and C. V. Sammut, "Ultra-wideband tightly coupled fractal octagonal phased array antenna," in *Proc. International Conference on Electromagnetics in Advanced Applications (ICEAA),* Sept. 2013, pp. 140-144.

[42] W. F. Moulder, K. Sertel, and J. L. Volakis, "Superstrate-Enhanced Ultrawideband Tightly Coupled Array With Resistive FSS," *IEEE Trans. Antennas Propag.*, vol. 60, no. 9, pp. 4166-4172, Sep. 2012.

[43] J. A. Kasemodel and J. L. Volakis, "A Planar Dual Linear-Polarized Antenna With Integrated Balun," *IEEE Antennas Wireless Propag. Lett*., vol. 9, pp. 787-790, 2010.

[44] T. R. Vogler and W. A. Davis, "Analysis and modification of the infinite foursquare array," in *Proc. Antennas and Propagation Society International Symposium (APSURSI), 2010*, Jul. 2010, pp. 1-4.

[45] J. J. Lee, S. Livingston, R. Koenig, D. Nagata, L. Lai, "Long slot arrays - part 2: ultra wideband test results," in *Proc. Antennas and Propagation Society International Symposium,* vol. 1A, 3-8, Jul. 2005, pp. 586-589.

[46] A. Neto and J. J. Lee, "Ultrawide-band properties of long slot arrays," *IEEE Trans. Antennas Propag.*, vol. 54, no. 2, pp. 534-543, Feb. 2006.

[47] J. Bai, S. Shi, G. Schneider, and D. Prather, "All-optical ultra-wideband tightly-coupled phased antenna array," in *Proc. Antennas and Propagation Society International Symposium (APSURSI),* Jul. 2014, pp. 1650-1651.

[48] N. K. Nahar, I. Tzanidis, K. Sertel, and J. L. Volakis, "Ultra wideband transparent RF aperture for electro-optical integration," in *Proc. Antennas and Propagation Society International Symposium (APSURSI),* Jul. 2010, pp. 1-4.

[49] N. Marchand "Transmission line conversion transformers," *Electronics*, vol. 17, pp. 142-145, Dec. 1944.

[50] S. S. Holland, D. H. Schaubert, and M. N. Vouvakis, "A 7–21 GHz Dual-Polarized Planar Ultrawideband Modular Antenna (PUMA) Array," *IEEE Trans. Antennas Propag.,* vol. 60, no. 10, pp. 4589-4600, Oct. 2012.

[51] J. T. Logan and M. N. Vouvakis, "On the design of 6:1 mm-wave PUMA arrays," in *Proc. Antennas and Propagation Society International Symposium (APSURSI),* Jul. 2013, pp. 626-627.

[52] S. S. Holland and M. N. Vouvakis, "The Planar Ultrawideband Modular Antenna (PUMA) Array," *IEEE Trans. Antennas and Propag.,* vol. 60, no. 1, pp. 130-140, Jan. 2012.

[53] J. T. Logan and M. N. Vouvakis, "Planar Ultrawideband Modular Antenna (PUMA) arrays scalable to mm-waves," in *Proc. Antennas and Propagation Society International Symposium (APSURSI),* July 2013, pp. 624-625.

[54] A. Oliner and G. Knittel, Eds., "Phased array antennas," in *Proc. 1970 Phased Array Symposium*, 1972 (Artech House, Dedham, MA).

[55] V. Galindo and C. P. Wu, "Dielectric loaded and covered rectangular waveguide phased arrays," *The Bell System Technical Journal*, vol. 47, no. 1, pp. 93-116, Jan. 1968.

[56] S. Lee and R. Mittra, "Radiation from dielectric-loaded arrays of parallel-plate waveguides," *IEEE Trans. Antennas Propag.*, vol. 16, no. 5, pp. 513-519, Sep. 1968.

[57] F. Silvestri, P. Chiusolo, L. Cifola, R. Bolt, and G. Gerini, "Design of metamaterial based wide angle impedance matching layers for active phased arrays," in *Proc. 9th European Conference on Antennas and Propagation (EuCAP)*, Lisbon, 2015, pp. 1-5.

[58] P. Rodríguez-Ulibarri, *et al*. "Experimental demonstration of metamaterials application for mitigating scan blindness in phased array antennas," *EPJ Appl. Metamat.* vol. 3, no. 9, Jul. 2016.

[59] S. Sajuyigbe, M. Ross, P. Geren, S. A. Cummer, M. H. Tanielian, and D. R. Smith, "Wide angle impedance matching metamaterials for waveguide-fed phased-array antennas," *IET Microw. Antennas Propag.*, vol. 4, no. 8, pp. 1063–1072, Aug. 2010.

[60] T. R. Cameron and G. V. Eleftheriades, "Analysis and characterization of a wide-angle impedance matching metasurface for dipole phased arrays," *IEEE Trans. Antennas Propag.*, vol. 63, no. 9, pp. 3928-3938, Sep. 2015.

[61] A. P. Feresidis, G. Goussetis, S.Wang and J. C. Vardaxoglou, "Artificial magnetic conductor surfaces and their application to low-profile high gain planar antennas," *IEEE Trans. Antennas Propag.*, vol. 53, no. 1, pp. 209−215, Jan. 2005.

[62] Y. Sun, Z. N. Chen, Y. W. Zhang, H. Chen and T. S. P. See, "Subwavelength substrate-integrated Fabry-Pérot cavity antennas using artificial magnetic conductor," *IEEE Trans. Antennas Propag.*, vol. 60, no. 1, pp. 30−35, Jan. 2012.

[63] K. Konstantinidis, A. P. Feresidis, and P. S. Hall, "Dual subwavelength Fabry-Perot cavities for broadband highly directive antennas," *IEEE Antennas Wireless Propag. Lett.*, vol. 13, pp. 1184–1186, 2014.

[64] A. Ghasemi, S. N. Burlkur, A. Dhouibi and A. Lustrac, "High beam steering in Fabry-Pérot leaky-wave antennas," *IEEE Antennas Wireless Propag. Lett.*, vol. 12, pp. 261-264, Mar. 2013.

[65] L. Y. Ji, Y. J. Guo, P. Y. Qin, S. X. Gong and R. Mittra, "A reconfigurable partially reflective surface (PRS) antenna for beam steering," *IEEE Trans. Antennas Propag.*, vol. 63, no. 6, pp. 2387-2395, Jun. 2015.

[66] F. Sultan and S. S. I. Mitu, "Superstrate-based beam scanning of a Fabry-Perot cavity antenna," *IEEE Antennas Wireless Propag. Lett.*, vol. 15, pp. 1187-1190, 2016.

[67] M. Thevenot, C. Cheype, A. Reineix, and B. Jecko, "Directive photonic bandgap antennas," *IEEE Trans. Microw. Theory Techn.*, vol. 47, no. 11, pp. 2115–2122, Nov. 1999.

[68] A. Weily, L. Horvath, K. Esselle, B. Sanders, and T. Bird, "A planar resonator antenna based on a woodpile EBG material," *IEEE Trans. Antennas Propag.*, vol. 53, no. 1, pp. 216–223, Jan. 2005.

[69] R. Gardelli, M. Albani, and F. Capolino, "Array thinning by using antennas in a Fabry–Perot cavity for gain enhancement," *IEEE Trans. Antennas Propag.*, vol. 54, no. 7, pp. 1979–1990, Jul. 2006.

[70] T. Debogovic and J. Perruisseau-Carrier, "Array-fed partially reflective surface antenna with independent scanning and beamwidth dynamic control," *IEEE Trans. Antenna. Propag.*, vol. 62. no. 1, pp. 446-449, Jan. 2014.

[71] L. Moustafa and B. Jecko, "Design of a Wideband Highly Directive EBG Antenna Using Double-Layer Frequency Selective Surfaces and Multifeed Technique for Application in the Ku-Band," *IEEE Antennas Wireless Propag. Lett.*, vol.9, pp. 342-346, Apr. 2010.

[72] A. Weily, K. P. Esselle, T. S. Bird, and B. C. Sanders, "Dual resonator 1-D EBG antenna with slot array feed for improved radiation bandwidth," *IET Microwaves, Antennas Propag.*, vol. 1, no. 1, pp. 198–203, Feb. 2007.

[73] Z.-H. Wu and W.-X. Zhang, “Broadband printed compound air-fed array antennas,” *IEEE Antennas Wireless Propag. Lett.*, vol. 9, pp. 187–190, 2010.

[74] Z.-G. Liu, W.-B. Lu, and W. Yang, "Enhanced Bandwidth of High Directive Emission Fabry-Perot Resonator Antenna with Tapered Near-Zero Effective Index Using Metasurface," *Scientific Reports,* vol. 7, no. 1, p. 11455, Sep. 2017.

[75] M. U. Afzal, K. P. Esselle and B. A. Zeb, “Dielectric phase-correcting structures for electromagnetic band gap resonator antennas,” *IEEE Trans. Antennas Propag.*, vol. 63, no. 8, pp. 3390−3399, Aug. 2015.

[76] L. Ji, P. Qin and Y. J. Guo, "Wideband Fabry-Perot Cavity Antenna With a Shaped Ground Plane," *IEEE Access*, vol. 6, pp. 2291-2297, 2018.

[77] R. M. Hashmi and K. P. Esselle, “A class of extremely wideband resonant cavity antennas with large directivity-bandwidth products,” *IEEE Trans. Antennas Propag.*, vol. 64, no. 2, pp. 830−835, Feb. 2016.

[78] A. P. Feresidis and J. C. Vardaxoglou, “High gain planar antenna using optimized partially reflective surfaces,” *IEEE Proc. Microwave Antennas Propag.*, vol. 148, no. 6, pp. 345–350, Dec. 2001.

[79] K. Konstantinidis, A. P. Feresidis and P. S. Hall, "Broadband Sub-Wavelength Profile High-Gain Antennas Based on Multi-Layer Metasurfaces," *IEEE Trans. Antennas Propag.*, vol. 63, no. 1, pp. 423-427, Jan. 2015.

[80] N. Wang, Q. Liu, C. Wu, L. Talbi, Q. Zeng and J. Xu, “Wideband Fabry-Perot Resonator Antenna with Two Complementary FSS Layers,” *IEEE Trans. Antennas Propag.*, vol. 62, no. 5, pp. 2463–2471, May. 2014.

[81] N. Wang, L. Talbi, Q. Zeng and J. Xu, "Wideband Fabry-Perot Resonator Antenna With Electrically Thin Dielectric Superstrates," *IEEE Access*, vol. 6, pp. 14966-14973, 2018.

[82] Y. Ge, K. P. Esselle, and T. S. Bird, “The use of simple thin partially reflective surfaces with positive reflection phase gradients to design wideband, low-profile EBG resonator antennas,” *IEEE Trans. Antennas Propag.*, vol. 60, no. 2, pp. 743–750, Feb. 2012.

[83] N. Engheta and R. W. Ziolkowski, Introduction, history, and selected topics in fundamental theories of metamaterials in *Metamaterials: Physics and Engineering Explorations* (eds. Engheta, N. & Ziolkowski, R. W.) 7 (John Wiley & Sons, 2006).

[84] R. W. Ziolkowski and E. Heyman, “Wave propagation in media having negative permittivity and permeability,” *Phys. Rev. E.,* vol. 64**,** 056625, 2001.

[85] D. R. Smith, W. J. Padilla, D. C. Vier, S. C. Nemat-Nasser, and S. Schultz, “Composite medium with simultaneously negative permeability and permittivity,” *Phys. Rev. Lett., vol.*84**,** pp. 4184, 2000.

[86] R. A. Shelby, D. R. Smith, and S. Schultz, “Experimental verification of a negative index of refraction,” *Science,* vol. 292, pp. 77–79, 2001.

[87] T. Koschny, M. Kafesaki, E. Economou, and C. Soukoulis, “Effective medium theory of left-handed materials,” *Phys. Rev. Lett.,* vol. 93, 107402, 2004.

[88] W. J. Padilla, D. N. Basov, and D. R. Smith, “Negative index metamaterials,” *Materials Today,* vol. 9, pp. 7-8, 2006.

[89] E. D. Goertz and C. F. Williams, “Metamaterial dispersion,” *U.S. Patent* 8, 648306, 2014.

[90] L. Holloway, *et al.,* “An overview of the theory and applications of metasurfaces: the two-dimensional equivalents of metamaterials,” *IEEE Ant. & Propag. Magazine*, vol. 54, pp. 10-35, 2012.

[91] F. Bilotti, A. Toscano, K. B. Alici, E. Ozbay, and L. Vegni, “Design of miniaturized narrowband absorber based on resonant-magnetic inclusions,” *IEEE Trans. Electromag. Compat.,* vol. 53, pp. 63-72 2011.

[92] N. I. Landy, S. Sajuyigbe, J. J. Mock, D. R. Smith, andW. J. Padilla, “ Perfect metamaterial absorber,” *Phys. Rev. Lett.,* vol. 100, 207402, 2008.

[93] O. Luukkonen, F. Costa, C. R. Simovski, A. Monorchio, and S. A. Tretyakov, “A thin electromagnetic absorber for wide incidence angles and both polarizations,” *IEEE Trans. Ant. & Propag.,* vol.10, pp. 3119-3125, 2009.

[94] P. Su, *et al., “*An ultra-wideband and polarization-independent metasurface for RCS reduction,” *Sci. Rep., vol.*6, 20387 (2016).

[95] H. –H. Hsiao, C. H. Chu, and D. P. Tsai, “Fundamentals and applications of metasurfaces,” *Small Methods.,* vol. 1, 1600064, 2017.

[96] B. A. Munk, Element types: a comparison in *Frequency Selective Surfaces: theory and design,* pp. 27-36, John Wiley & Sons, 2000.

[97] D. Ö. Güney, T. Koschny, and C. M. Soukoulis, “Reducing ohmic losses in metamaterials by geometric tailoring,” *Phys. Rev. B,* vol. 80, 125129, 2009.

[98] J. Naqui, *et al*., “Common-mode suppression in microstrip differential lines by means of complementary split ring resonators: theory and applications,” *IEEE Trans. Microw.Theory Techn.,* vol. 60, pp. 3023-3034, 2012.

[99] J. Naqui *et al*., "Split rings-based differential transmission lines with common-mode suppression," *IEEE MTT-S International Microwave Symposium*, Baltimore, MD, 2011, pp. 1-4.

[100] D. Schurig, J. J. Mock, and D. R. Smith, “Electric-field-coupled resonators for negative permittivity metamaterials,” *Appl. Phys. Lett.,* vol. 88, 041109, 2006.

[101] J. Y. Yin, X. Wan, Q. Zhang, and T. J. Cui, “Ultra wideband polarization-selective conversions of electromagnetic waves by metasurface under large-range incident angles,” *Sci. Rep.* vol. 5, 12476, 2015.

[102] ANSYS HFSS ver. 16, ANSYS, Inc., Canonsburg, PA [Online]. Available: https://www.ansoft.com/products/hf/hfss/

[103] Matlab R2016, The Mathworks, Inc., Natick, MA [Online]. Available: https://www.mathworks.com/products/matlab/

[104] Z. Szabo, G. H. Park, R. Hedge and E. P. Li, "A unique extraction of metamaterial parameters based on Kramers–Kronig relationship," *IEEE Trans. Microw. Theory Techn.*, vol. 58, no. 10, pp. 2646-2653, Oct. 2010.

[105] C. M. Watts, X. Liu, and W. J. Padilla, "Metamaterial electromagnetic wave absorbers," *Adv. Mater*., vol. 24, pp. 98–120, 2012.

[106] R. de L. Kronig, "On the theory of the dispersion of X-rays". *J. Opt. Soc. Am.* vol. 12, pp. 547–557, 1926.

[107] H. A. Kramers, "La diffusion de la lumière par les atomes". *Atti Cong. Intern. Fisici, (Transactions of Volta Centenary Congress) Como.* vol. 2, pp. 545–557, 1927.

[108] J. P. Doane, "Wideband low-profile antenna arrays: Fundamental limits and practical implementations," Ph.D. dissertation, Dept. Elect. Comput. Eng., Ohio State Univ., Columbus, OH, USA, 2013.

[109] B. A. Munk, *Finite Antenna Arrays and FSS*, ch. 6, pp. 181-213, John Wiley & Sons, Hoboken, NJ, 2003.

[110] A. K. Bhattacharyya, "Floquet modal functions," in *Phased Array Antennas: Floquet Analysis, Synthesis, BFNs and Active Array Systems*, 1st ed. Hoboken, NJ, USA: Wiley-Interscience, 2006.

[111] R. C. Hansen, *Microwave Scanning Antennas Vol. II*, Array Theory and Practice. New York, NY, USA: Academic, 1966.

[112] R. W. Klopfenstein, "A Transmission Line Taper of Improved Design," in *Proc. of the IRE*, vol. 44, Jan. 1956, pp. 31-15.

[113] D. M. Pozar, *Microwave Engineering*, ch. 3, pp. 148-149, John Wiley & Sons, Hoboken, NJ, 2012.

[114] R. J. P. Douville and D. S. James, "Experimental Characterization of Microstrip Bends and Their Frequency Dependent Behavior," in *Proc. IEEE Conf. Digest,* Oct. 1973, pp. 24-25.

[115] A. Ludwig, "The definition of cross polarization," *IEEE Trans. Antennas Propag.*, vol. 21, pp. 116–119, Jan. 1973.

[116] A. O. Bah, P. Y. Qin, R. W. Ziolkowski, Q. Cheng and Y. J. Guo, "Realization of an Ultra-thin Metasurface to Facilitate Wide Bandwidth, Wide Angle Beam Scanning," *Scientific Reports*, vol. 8, no. 1, pp. 4761, Mar. 2018.

[117] R. C. Hansen, *Phased Array Antennas*. Hoboken, NJ, USA: Wiley, 2009, ch. 15, pp. 526–527.

[118] E. Yetisir, N. Ghalichechian and J. L. Volakis, "Ultrawideband array with 70° scanning using FSS superstrate," *IEEE Trans. Antennas Propag.*, vol. 64, no. 10, pp. 4256-4265, Oct. 2016.

[119] H. Holter, T.H. Chio, and D. H. Schaubert, “Experimental results of 144-element dual-polarized endfire tapered-slot phased arrays,” *IEEE Trans. Antennas Propag.*, vol. 48, no. 11, pp. 1707-1718, Nov. 2000.

[120] D. H. Schaubert, S. Kasturi, A. O. Boryssenko, and W. M. Elsallal, “Vivaldi antenna arrays for wide bandwidth and electronic scanning,” in *Proc. EuCAP - European Conference on Antennas & Propagation*. IET, Nov. 2007, pp. 1-6.

[121] M. J. Buckley, J. Wolf, B. J. Herting, J. Mather, D. Manson, and J. B. West, “Wide band and wide scan metamaterial loaded radiating elements,” in *Proc. Antennas and Applications Symposium*, *Allerton IL*, Sep. 2010.

[122] R. Erickson et al., “Wideband and wide scan phased array microstrip patch antennas for small platforms,” in *Proc. EuCAP - European Conference on Antennas & Propagation*. IET, Nov. 2007, pp. 1-6.

[123] M. Stasiowski and D. Schaubert, “Broadband array antenna,” in *Proc. Antennas and Applications Symposium, Allerton IL*, Sep. 2008.

[124] Y. J. Lee, J. Yeo, R. Mittra, and W. S. Park, “Application of electromagnetic bandgap (EBG) superstrates with controllable defects for a class of patch antennas as spatial angular filters,” *IEEE Trans. Antennas Propag.*, vol. 53, no. 1, pp. 224–235, Jan. 2005.

[125] T. S. Bird, *Fundamentals of Aperture Antennas and Arrays: From Theory to Design, Fabrication and Testing*, Ch. 9, pp. 352-353, John Wiley & Sons, West Sussex, UK, 2016.

[126] F. Wu, and K. M. Luk, “Wideband High-Gain Open Resonator Antenna Using a Spherically Modified, Second-Order Cavity,” *IEEE Trans. Antennas Propag.*, vol. 65, no. 4, pp. 2112–2116, Apr. 2017.

[127] K. Konstantinidis, A. P. Feresidis, and P. S. Hall, "Dual-slot feeding technique for broadband Fabry–Perot cavity antennas," *IET Microwaves Antennas Propag.*, vol. 9, no. 9, pp. 861-866, 2015.

[128] N. Nguyen-Trong, H. H. Tran, T. K. Nguyen and A. M. Abbosh, "A Compact Wideband Circular Polarized Fabry-Perot Antenna Using Resonance Structure of Thin Dielectric Slabs," *IEEE Access*, vol. 6, pp. 56333-56339, Sep. 2018.

[129] N. Nguyen-Trong, H. H. Tran, T. K. Nguyen and A. M. Abbosh, "Wideband Fabry–Perot Antennas Employing Multilayer of Closely Spaced Thin Dielectric Slabs," *IEEE Antennas Wireless Propag. Lett.*, vol. 17, no. 7, pp. 1354-1358, Jul. 2018.

[130] L. Leger, C. Serier, R. Chantalat, M. Thevenot, T. Monediere, and B. Jecko, “1D dielectric electromagnetic band gap resonator antenna design,” *Annales Telecoms*, vol. 59, pp. 246, Mar. 2004.

[131] L. Moustafa and B. Jecko, “EBG structure with wide defect band for broadband cavity antenna applications,” *IEEE Antennas Wireless Propag. Lett.*, vol. 7, pp. 693–696, Nov. 2008.

[132] L. Leger, T. Monediere, and B. Jecko, “Enhancement of gain and radiation bandwidth for a planar 1-D EBG antenna," *IEEE Microwave Wireless Components Lett.*, Vol. 15, no. 9, pp. 573-575, Sep. 2005.

[133] R. Mittra, C. H. Chan and, T. Cwik, "Techniques for analyzing frequency selective surfaces-a review," in *Proc. of the IEEE*, vol. 76, no. 12, pp. 1593-1615, Dec. 1988.

[134] Shung-Wu Lee, G. Zarrillo, and Chak-Lam Law, "Simple formulas for transmission through periodic metal grids or plates," *IEEE Trans. Antennas Propag.*, vol. 30, no. 5, pp. 904-909, Sep. 1982.